

Characterization of phase transitions in warm dense matter with X-ray scattering

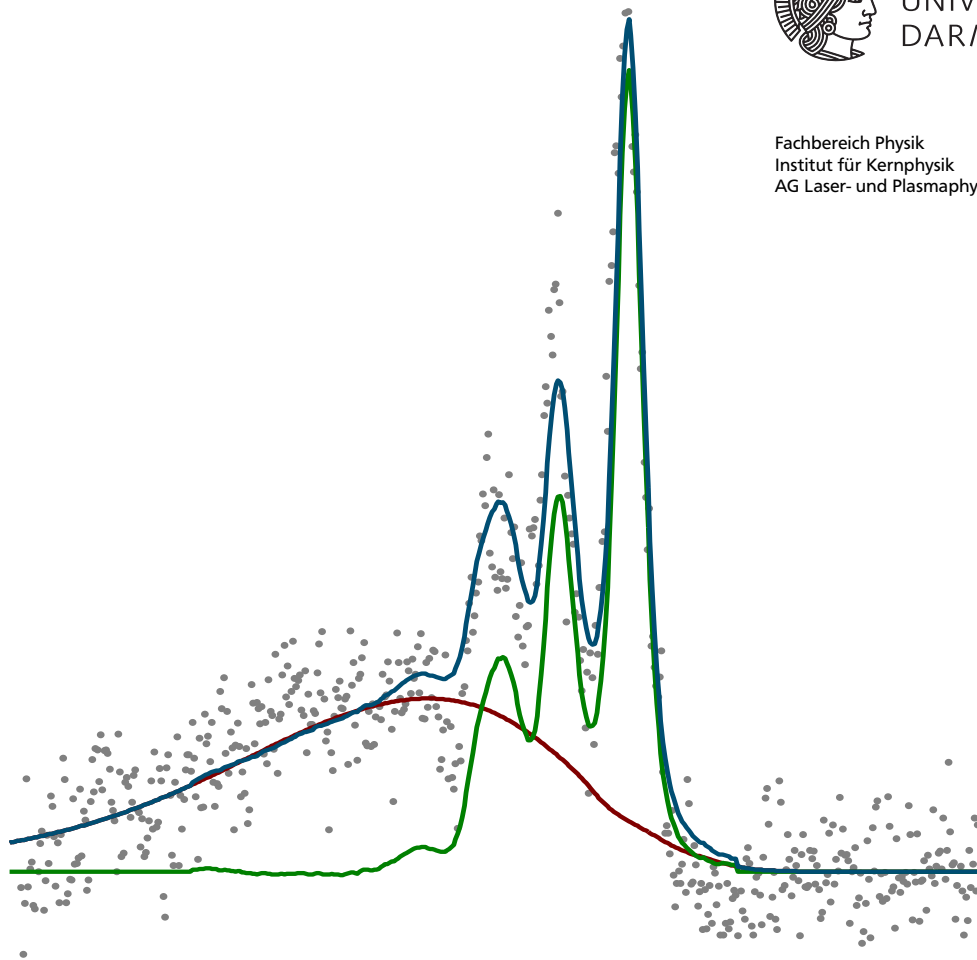
Charakterisierung von Phasenübergängen in warmer dichter Materie mit Röntgenstreuung

Zur Erlangung des Grades eines Doktors der Naturwissenschaften (Dr. rer. nat.)
genehmigte Dissertation von M. Sc. Dominik Kraus aus Darmstadt
Dezember 2012 — Darmstadt — D 17



TECHNISCHE
UNIVERSITÄT
DARMSTADT

Fachbereich Physik
Institut für Kernphysik
AG Laser- und Plasmaphysik



Characterization of phase transitions in warm dense matter with X-ray scattering
Charakterisierung von Phasenübergängen in warmer dichter Materie mit Röntgenstreuung

Genehmigte Dissertation von M. Sc. Dominik Kraus aus Darmstadt

1. Gutachten: Prof. Dr. Markus Roth
2. Gutachten: Prof. Dr. Dr. h.c./RUS Dieter H. H. Hoffmann

Tag der Einreichung: 9. Oktober 2012

Tag der Prüfung: 26. November 2012

Darmstadt — D 17

Zusammenfassung

Die vorliegende Arbeit befasst sich mit der experimentellen Erzeugung und Untersuchung von *warmer dichter Materie*, d. h. dem Übergangsbereich zwischen Festkörpern und dichten Plasmen. Dieser stellt für theoretische Modelle eine große Herausforderung dar und ist gleichzeitig experimentell schwer zugänglich. Die Physik warmer dichter Materie ist von entscheidender Bedeutung für die Trägheitsfusion und die Beschreibung des Inneren von großen Planeten. Um verschiedene theoretische Modellierungen dieses Gebietes zu testen, sind experimentelle Daten zwingend erforderlich.

Im Rahmen dieser Arbeit wurde das Verhalten von Kohlenstoff bei einem Druck um 100 GPa ($=10^6$ bar) und einer Temperatur um 8000 K untersucht. Theoretische Modelle vermuten in diesem Bereich einen fest-flüssig Phasenübergang. Dieser konnte durch die in dieser Arbeit beschriebenen Experimente erstmals im Labor charakterisiert werden.

Der zu vermessende Materiezustand wurde durch lasergetriebene Schockkompression von Graphit der Ausgangsdichte 1.84 g/cm^3 erzeugt. Dazu wurde das Lasersystem *nhelix* am *GSI Helmholtzzentrum für Schwerionenforschung* verwendet. Über Messung von Schock- und Teilchengeschwindigkeit konnten Dichte und Druck innerhalb der Schockwelle bestimmt werden. Die Kohlenstoffproben wurden auf $3.9 \pm 0.2 \text{ g/cm}^3$, d.h. etwa das Zweifache der ursprünglichen Dichte, komprimiert und Drücke von 80 GPa bis 170 GPa erzeugt. Dies ist in sehr guter Übereinstimmung mit ein- bzw. zweidimensionalen Hydrodynamik-Simulationen, die mit den Paketen HELIOS bzw. MULTI2D durchgeführt wurden.

Für die Untersuchung der mikroskopischen Struktur der verdichteten Kohlenstoffproben wurde intensive gepulste Röntgenstrahlung eingesetzt, die mit dem Lasersystem *PHELIX* durch das Bestrahlen von Titanfolien erzeugt wurde. Der verwendete Titan-Helium- α Übergang, der in eine emittierte Photonenenergie von 4.75 keV resultiert, konnte mit hoher Effizienz angeregt werden. Ein Anteil der Laserenergie von $\sim 0.5\%$ wurde in Röntgenstrahlung dieses Übergangs konvertiert. Die spektral aufgelöste Messung der gestreuten Strahlung ermöglicht die Bestimmung der Korrelationen der Kohlenstoffatome über den Strukturfaktor. Bei den speziell ausgesuchten Streuwinkeln 105° und 126° ändert sich der Strukturfaktor und damit auch der Streuwirkungsquerschnitt innerhalb des Phasenübergangs um einen Faktor zwei. Diese Änderung konnte im Rahmen dieser Arbeit experimentell nachgewiesen werden.

Absolute Werte für den Strukturfaktor wurden durch die Bestimmung der Verhältnisse der Intensitäten von elastisch und inelastisch gestreuter Röntgenstrahlung ermittelt. Für eine Dichte von $3.9 \pm 0.2 \text{ g/cm}^3$ und einen Druck von 145 ± 17 GPa wurde in der Schockwelle die Existenz einer flüssigen Phase experimentell nachgewiesen. Bei einem niedrigeren Druck von 86 ± 11 GPa und ebenfalls einer Dichte von $3.9 \pm 0.2 \text{ g/cm}^3$ wurde ein Zustand sehr nahe der Schmelzlinie erzeugt, der gerade noch flüssig ist. Dies ist in sehr guter Übereinstimmung mit ab-initio-Simulationen, mit denen Strukturfaktoren für diese Parameter berechnet wurden.

Somit wurde im Rahmen dieser Arbeit ein experimenteller Weg aufgezeigt, Phasenübergänge in warmer dichter Materie zu charakterisieren und erstmals die Erzeugung von flüssigem Kohlenstoff durch Schockkomprimierung von Graphit direkt beobachtet.



Abstract

The topic of this thesis is the experimental generation and characterization of *warm dense matter*, i. e. the intermediate regime between solid state materials and dense plasmas. These states are challenging for both theoretical models and experimental measurements in the laboratory. The physics of warm dense matter is of essential importance for inertial confinement fusion and the understanding of giant planets. For testing different theoretical models of this field, experimental data is urgently needed.

In the framework of this thesis, the properties of carbon at a pressure around 100 GPa and a temperature of roughly 8000 K were investigated. Theoretical models predict a solid-liquid phase transition in this regime. This transition could be characterized for the first time in the laboratory by the experiments presented in this thesis.

The desired matter states were produced by laser-driven shock compression of graphite samples with an initial density of 1.84 g/cm^3 . For this purpose, the laser system *nhelix* at the *GSI Helmholtzzentrum für Schwerionenforschung* was applied. Density and pressure inside the shock wave were determined by measurements of shock velocity and particle velocity. The carbon samples were compressed to a density of $3.9 \pm 0.2 \text{ g/cm}^3$, i.e. about two times the initial density, and pressures from 80 GPa to 170 GPa were achieved. This is in very good agreement with one- and two-dimensional hydrodynamic simulations using the code packages HELIOS and MULTI2D, respectively.

For the investigation of the microscopic structure inside the compressed carbon samples, intensive pulsed X-ray radiation was produced by irradiation of titanium foils with the *PHELIX* laser system. The applied titanium helium- α transition, which emits photons of the energy 4.75 keV, could be triggered very efficiently. In fact, a conversion efficiency from laser energy to X-rays of $\sim 5 \times 10^{-3}$ was achieved. The spectrally resolved measurement of the scattered radiation allows for determining the correlations of the carbon atoms via the structure factor. For the specially chosen scattering angles of 105° and 126° , a strong change of the structure factor is expected to happen for the solid-liquid phase transition resulting in a strong change of the scattering cross section. This change could be verified experimentally in the framework of this thesis.

Absolute values of the structure factor were obtained by determining the intensity ratios of elastically and inelastically scattered X-ray radiation. The existence of a liquid phase was experimentally observed for a density of $3.9 \pm 0.2 \text{ g/cm}^3$ and a pressure of $145 \pm 17 \text{ GPa}$ inside the shock wave. For a lower pressure of $86 \pm 11 \text{ GPa}$ and a similar density of $3.9 \pm 0.2 \text{ g/cm}^3$, a state of matter was produced which is very close to the melting line and just barely liquid. This is in very good agreement with ab-initio simulations which were used to calculate structure factors for the investigated parameters.

Thus, in the framework of this thesis an experimental method for the characterization of phase transitions in warm dense matter was demonstrated and the formation of liquid carbon under shock compression was reliably observed using graphite as initial state for the first time.



Contents

1	Introduction	1
1.1	Motivation	1
1.2	Experimental work and simulations	3
1.3	Thesis structure	3
1.4	Units	4
2	Warm Dense Matter	5
2.1	Localization and definition	5
2.2	Radial distribution function	7
2.3	Warm dense carbon	8
3	Laser plasma interaction	11
3.1	Basic properties of a laser-driven plasma	11
3.2	Absorption	12
3.3	Transport mechanisms	12
3.3.1	Heat conduction	13
3.3.2	Radiation transport	13
3.4	Ablation pressure	14
3.5	Shock waves	15
3.5.1	Shock waves in solids	17
3.5.2	Porous materials	17
3.5.3	Phase transitions within a shock wave	18
3.6	X-ray generation	20
3.6.1	Helium-alpha emission	20
4	X-ray scattering	23
4.1	X-ray Thomson scattering from a single free electron	24
4.2	X-ray scattering from matter	26
4.2.1	Elastic scattering	30
4.2.2	Inelastic scattering from free electrons	32
4.2.3	Inelastic scattering from bound electrons	32
4.3	Measurement and characterization of phase transitions	34
5	Experimental methods	37
5.1	Experimental setup at the target area Z6 at GSI	37
5.1.1	The <i>nhelix</i> laser system	41
5.1.2	The <i>PHELIX</i> laser system	42
5.2	Realization and characterization of laser-driven shock waves	43
5.2.1	Carbon targets	43
5.2.2	Shadowgraphy	44
5.2.3	Streak camera	45
5.3	X-ray generation and scattering	46
5.3.1	X-ray backlighter target design and fabrication	46
5.3.2	Alignment methods	47

5.3.3	HOPG crystals	48
5.3.4	Image plates	49
6	Simulations	51
6.1	Hydrodynamics of the shock waves	51
6.1.1	Simulations with HELIOS	52
6.1.2	Simulations with MULTI2D	53
6.1.3	Comparison	56
6.2	Ab-initio simulations	57
6.2.1	DFT-MD	57
6.2.2	Microscopic structure of shock-compressed graphite	59
7	Experimental results and discussion	61
7.1	Thermodynamic state in the shock wave	61
7.1.1	Experimental campaign March/April 2011	63
7.1.2	Experimental campaign February/March 2012	65
7.1.3	Hugoniot data	67
7.2	X-ray generation	68
7.2.1	Shadowgraphy images	69
7.2.2	Spectral features of the source radiation and resulting plasma parameters	70
7.2.3	Conversion efficiency of laser energy to X-rays	73
7.2.4	Estimated heating of the carbon sample by probe radiation X-rays	74
7.2.5	Angular distribution of the X-rays	75
7.3	Absorption characteristics and influence of the shock-driving laser plasma	76
7.4	Transmission measurements and 38° spectrometer	77
7.5	Scattering spectra	78
7.5.1	Experimental campaign March/April 2011	78
7.5.2	Experimental campaign February/March 2012	81
7.6	Conclusions	86
8	Outlook	89
8.1	Further improvements of the presented experiments	89
8.2	Isochoric heating with intense laser-generated particle beams	91
8.3	4th generation light sources	91
8.4	Perspectives for WDM experiments at FAIR	91
	Bibliography	93
	Publications	103
	Danksagung	105
	Lebenslauf	107

1 Introduction

1.1 Motivation

Understanding the properties of so-called "warm dense matter" (WDM) is a young and highly evolving field of physics [Lee et al., 2002, 2003]. Typical attributes of matter in the WDM regime are temperatures from several thousand to several hundred thousand kelvins and densities around solid density resulting in pressures from several thousand to several million atmospheres.

In particular, the physics of warm dense matter is highly relevant for geophysics as the earth's core mainly consists of iron in WDM states [Koenig et al., 2010]. In astrophysics, a detailed understanding of WDM is needed to develop models of giant planets which, to a large extent, are composed of low-Z element mixtures in warm dense matter states [Militzer et al., 2008; Nettelmann et al., 2008]. Additional natural occurrences of WDM are brown and white dwarfs [Dufour et al., 2007] as well as the outer crust of neutron stars [Daligault and Gupta, 2009]. Another field of science, which strongly relies on understanding the physics of warm dense matter, is the controlled realization of inertial confinement fusion in the laboratory [Lindl et al., 2004; Atzeni and Meyer-ter-Vehn, 2004]. Concerning the at present ongoing inertial confinement fusion experiments at the National Ignition Facility (NIF) [Glenzer et al., 2010], the target hohlraum walls are in a WDM state as well as, in a transient state, the ablator material surrounding the fusion capsule and, also as a transient state, the deuterium-tritium fuel itself.

More generally speaking, warm dense matter is generated for a short time in every process involving very rapid heating of a solid state density sample. This is for example fulfilled in every interaction of a high energy laser with a solid state material. In particular, the relation which connects the basic thermodynamic parameters like for example density, temperature and pressure, the so-called "equation of state", is of high interest for materials in warm dense matter states. Additionally, knowledge of material properties like phase transitions, opacities, energy absorption rates, response functions and relaxation rates is needed for a complete physical understanding of the warm dense matter regime.

The controlled realization of warm dense matter states in the laboratory and their diagnostics is a very challenging and demanding task. Shock experiments have been a common tool to explore the properties of matter at high pressures for many years. The benefit of this method is that material under shock-compression is heated instantaneously which can lead to exotic states of matter including warm dense matter. Shock waves with pressures of more than 100 GPa ($=10^6$ bar) can be realized with gas guns [Gust, 1980], high explosives [Nellis et al., 2001], high intensity particle beams [Fortov et al., 1996], pulsed power devices [Knudson et al., 2008], and pulsed high energy laser systems [Batani et al., 2004]. Using the Rankine-Hugoniot equations, the thermodynamic parameters density, pressure and specific internal energy can directly be obtained by measuring the shock and particle velocities [Zeldovic and Raizer, 1966]. Furthermore, discontinuities in the velocity measurements indicate phase transitions inside the shocked material. However, the real microscopic structure of the shocked material is not accessible just by velocity measurements. A very promising diagnostic method, which emerged in the last decade, is the scattering of intense X-ray radiation produced by laser plasmas [Glenzer and Redmer, 2009]. This method has proven

to be capable to resolve the electronic and atomic or ionic structure of short-lived warm dense matter samples [Garcia Saiz et al., 2008]. Additionally, thermodynamic parameters like temperature, density and ionization degree of dense plasmas can be obtained [Gregori et al., 2004].

The better understanding of carbon in warm dense matter states is highly relevant to particular applications. Large samples of warm dense carbon are for example produced in graphite beam dumps of the newest generation of particle accelerators like the LHC [Zazula, 1997]. In inertial confinement fusion research carbon may be used as ablator material and an improved knowledge of the equation of state would simplify the simulations of the processes that should lead to ignition of the fusion capsule [Kritcher et al., 2011]. Furthermore, the equation of state of warm dense carbon is very interesting for the description of the ice giants in our solar system (Neptune and Uranus [Hubbard et al., 1991; Stanley and Bloxham, 2004]), comparable extra-solar planetary systems (for example pure carbon planets [Kuncher and Seager, 2005]) and brown and white dwarfs [Dufour et al., 2007]. Hereby, the carbon solid-liquid phase transition may play a major role. In the pressure regime of these astrophysical objects, this transition is poorly understood so far and further investigation is needed [Correa et al., 2008].

Besides its high physical relevance, elementary carbon is a very useful material for laboratory warm dense matter studies. Compared to cryogenic hydrogen or helium and lithium, stable and pure solid density carbon samples are easy to manufacture and handle. Additionally, there are no health or equipment contamination risks as there are for example in experiments investigating highly toxic beryllium. Another advantage is that the initial density of carbon can be varied by using different types of amorphous, polycrystalline and monocrystalline carbon in an experiment. Therefore, very different final warm dense matter states can be produced by the same experiment. As a relatively low-Z element, carbon is also accessible theoretically reasonably well. Due to its low number of electrons, a number of theoretical and numerical techniques, including *ab-initio simulations*, allow for the description of its properties within the computational resources available today [Correa et al., 2006].

Following this motivation, the topic of this thesis is the experimental investigation of the solid-liquid phase transition in shock-compressed graphite with X-ray scattering. Different theories suggest that driving pressures from ~ 80 [Grover, 1979] to ~ 300 GPa [Nellis et al., 2001] are needed to reach the melting threshold of shocked graphite starting in an initial state with ideal crystal density. There are some velocity measurements on shocked graphite which claim to have seen a discontinuity in this regime [Alder and Christian, 1961], some have not [Pavlovskii and Drakin, 1966; Gust, 1980]. Some show very slight indications of a phase transition [van Thiel, 1977; Marsh, 1980], but these are within the experimental uncertainty and hence an exact statement cannot be given. In the end, the currently agreed conclusion is that velocity measurements are not sufficient to detect the solid-liquid transition of shock-compressed graphite. In the last decade, experiments using diamond as initial state have detected a phase transition to a metallic liquid state. In these experiments, reflectivity and pyrometry measurements of the shock front have been performed which took advantage of the optical transparency of diamond [Bradley et al., 2004; Eggert et al., 2009]. However, these methods are not applicable for optically opaque materials like graphite and, in fact, the solid-liquid phase transition of shock-compressed graphite has not been measured reliably so far. As stated above, an alternative is the use of intense laser-generated X-rays which are able to access the processes inside a warm dense matter sample. This method was first applied for the carbon solid-liquid phase transition at lower pressure (few GPa) in a proof-of-principle experiment where the heating was realized isochorically by intense laser-accelerated proton beams [Roth et al., 2009; Pelka et al., 2010; Pelka, 2010]. Concerning the application of this technique for the diagnostics of strong shock waves, there are few facilities in

the world where sufficient basic conditions for these experiments are given because a 100 GPa shock drive and a pulsed high energy laser system for the X-ray generation are needed in combination. The experiments in the framework of this thesis were performed at the *GSI Helmholtzzentrum für Schwerionenforschung* in Darmstadt which currently offers two high energy laser systems, *nhelix* [Schaumann et al., 2005] and the larger *PHELIX* system [Bagnoud et al., 2010], with sufficient parameters to realize such experiments.

This work is strongly connected to the future plasma physics experiments at the *Facility for Antiproton and Ion Research (FAIR)* which is at present under construction next to GSI [Gutbrod et al., 2006]. Due to its numerous benefits, X-ray scattering is planned to be a central diagnostics for all three upcoming plasma physics experiments, *Heavy Ion Heating and Expansion (HIHEX)*, *Laboratory of Planetary Sciences (LAPLAS)* and *Warm Dense Matter (WDM)*, which aim for a precise characterization of warm dense matter [Tahir et al., 2011]. In the framework of the experiments presented in this thesis, successful X-ray scattering experiments on the characterization of warm dense matter have been performed for the first time at GSI. This gives a start for the future development of X-ray scattering as a standard diagnostics for FAIR.

1.2 Experimental work and simulations

The experimental work presented in this thesis is divided in two separate campaigns which were conducted at the GSI Helmholtzzentrum für Schwerionenforschung in March/April 2011 and February/March 2012. In addition to the shock-drive and X-ray generation capabilities, the experimental area Z6 at GSI offers diagnostics which allow for velocity measurements of laser-driven shocks [Kraus et al., 2012]. These instruments open the possibility to determine the thermodynamic state of the shocked graphite samples independently from the X-ray scattering measurements. This is in contrast to most other X-ray scattering campaigns which have been performed by the warm dense matter research community so far. These experiments generally relied exclusively on hydrodynamic simulations to define the thermodynamic state of the investigated samples.

Hydrodynamic simulations, however, were also very important for the design and the analysis of the experiments presented in this thesis. Hereby the one-dimensional HELIOS simulation package [MacFarlane et al., 2006] and the two-dimensional MULTI2D code [Ramis et al., 2009] in combination with the PROPACEOS and SESAME equation of state tables were applied to define the laser-parameters of the shock drive. In addition, a fruitful collaboration with the Centre for Fusion, Space and Astrophysics at the University of Warwick, United Kingdom allowed for the access to *ab-initio* simulations based on density functional theory and molecular dynamics (DFT-MD). These calculations were very useful for the analysis of the obtained X-ray scattering spectra.

1.3 Thesis structure

The outline of this thesis is as follows: After this introduction, chapter two describes the basic properties and challenges connected with warm dense matter, focusing on warm dense carbon. Chapter three introduces the fundamental physics of laser plasma interactions before describing the two special applications of this field which are relevant to the experiments presented in this thesis: laser-driven shock waves and the generation of intense X-ray radiation. Chapter four deals with X-ray scattering as a diagnostic tool for warm dense matter states, especially in the context of the solid-liquid phase transition in shock-compressed graphite. The experimental setup of the two campaigns conducted in the framework of this thesis is presented in chapter five. This includes a description of the instruments applied for generation and characterization of the produced states.

Chapter six describes the numerical calculations which were necessary for the design and analysis of the experiments. The hydrodynamic code packages HELIOS and MULTI2D are introduced which were applied for the simulation of the laser-driven shock propagation. Furthermore, the *ab-initio* calculations which supported the analysis of the microscopic carbon structure inside the shock waves are briefly described. Chapter seven then shows the experimental results which were obtained during the experimental campaigns at GSI. This includes the analysis of the velocity measurements to determine the thermodynamic state of the shocked carbon, the characterization of the X-ray source radiation and the interpretation of the X-ray scattering spectra to deduce the microscopic sample structure. All results are compared to numerical calculations in this chapter: velocity measurements to hydrodynamic simulations, source radiation spectra to collisional-radiative codes and X-ray scattering spectra to *ab-initio* simulations. Chapter eight finally shows perspectives which follow from the results obtained by the experiments in the framework of this thesis and suggestions for next steps are presented.

1.4 Units

As this thesis mainly describes experimental work, the applied system of units is the SI system for a better direct calculation of real quantities. Occasionally, some numbers are given in units which are more common in everyday work than pure SI units. For example, mass densities are given in grams per cubic centimeter and most temperatures have the unit electronvolt (eV or more correct eV/k_B , where k_B is the Boltzmann constant, 1 eV temperature corresponds to 11605 kelvins).

2 Warm Dense Matter

Warm dense matter (WDM) is the intermediate regime of matter between condensed materials and hot, weakly coupled plasmas [Lee et al., 2002, 2003]. Therefore, WDM cannot be described by simple temperature assumptions like $T \approx 0$ (classical solid state physics) or $T \gg T_F$ and $k_B T \gg E_{\text{pot}}$ (classical plasma physics), where T_F is the Fermi temperature, k_B the Boltzmann constant and E_{pot} the potential energy of the atomic interaction. This definition is rather qualitative and, in fact, so far there is no general agreement on the exact limits given for thermodynamic parameters of WDM. Nevertheless, these can be roughly summarized as follows: The density is close to solid state density, the temperature is between several thousand and several hundred thousand kelvins and the pressure can be found between 1 GPa and 1 TPa. Therefore, the warm dense matter regime partially overlaps with the very recently defined field of 'high energy density physics' [Drake, 2006], which investigates materials with pressures of at least 100 GPa (=1 Mbar) and is currently seen as one of the biggest challenges of contemporary sciences [US National Research Council, 2003].

2.1 Localization and definition

An important scale for the localization and definition of WDM is the product of electron number density n_e (= number of electrons per unit volume) and the third power of the thermal de-Broglie-wavelength Λ_e :

$$n_e \Lambda_e^3 = n_e \left(\frac{2\pi\hbar^2}{m_e k_B T} \right)^{\frac{3}{2}}. \quad (2.1)$$

Hereby, m_e is the electron mass, k_B the Boltzmann constant and T the temperature. For $n_e \Lambda_e^3 \gtrsim 1$, the probability clouds of the electron wave functions overlap [Kremp et al., 2005]. Thus, the electrons are indistinguishable and degeneracy effects cannot be neglected. However, the model of a fully degenerate electron gas can only be applied for $n_e \Lambda_e^3 > 10$. In contrast, a classical approach is only useful for $n_e \Lambda_e^3 \ll 1$. For warm dense matter one typically obtains $n_e \Lambda_e^3 \approx 1$. Therefore, a theoretical description for this state of matter is more complicated than for both the ideal degenerate and ideal classical case.

Another important scale is the electron-electron coupling parameter Γ_{ee} which compares the mean interaction potential energy to the mean kinetic energy of the electrons:

$$\Gamma_{ee} = \frac{\langle E_{\text{pot}} \rangle}{\langle E_{\text{kin}} \rangle}. \quad (2.2)$$

For the ideal plasma case ($n_e \Lambda_e^3 \rightarrow 0$), the kinetic energy is simply given by the temperature whereas for a highly degenerate system ($n_e \Lambda_e^3 \gg 1$), the electrons do not fulfill Boltzmann but Fermi-Dirac statistics. Therefore, the Fermi energy

$$E_F = \frac{\hbar^2}{2m_e} (3\pi^2 n_e)^{2/3}, \quad (2.3)$$

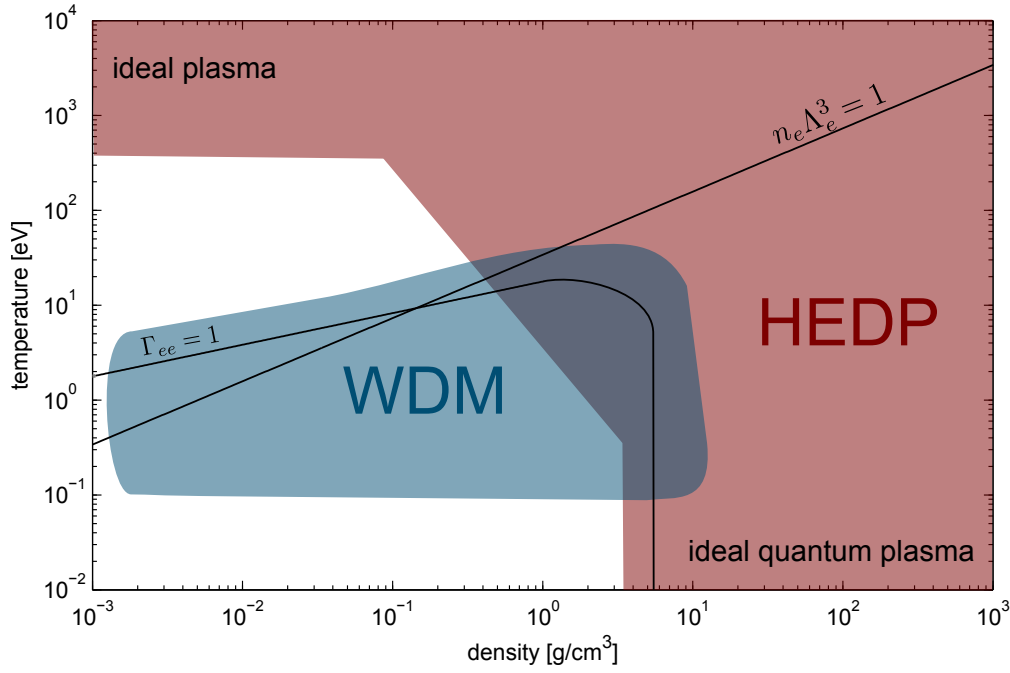


Figure 2.1: Warm dense matter (WDM) domain in the temperature-density diagram of hydrogen as defined in [Lee et al., 2002, 2003]. The High Energy Density Physics (HEDP) regime with pressures larger than 100 GPa [Drake, 2006] and the lines $n_e \Lambda_e^3 = 1$ as well as $\Gamma_{ee} = 1$ [Wünsch, 2011] are also shown.

which is independent from temperature, is the appropriate scale in this case. The mean interaction potential energy is approximately given by the Coulomb potential at the mean particle distance $\langle d \rangle = [3/(4\pi n_e)]^{1/3}$ (Wigner-Seitz radius). Therefore, both limiting cases give

$$\Gamma_{ee} \xrightarrow{n_e \Lambda_e^3 \ll 1} \frac{e^2}{4\pi\epsilon_0 k_B T \langle d \rangle} \quad (2.4)$$

$$\Gamma_{ee} \xrightarrow{n_e \Lambda_e^3 \gg 1} \frac{e^2}{4\pi\epsilon_0 E_F \langle d \rangle} \quad (2.5)$$

In the warm dense matter regime one typically obtains $\Gamma_{ee} \approx 1$, which implies moderately coupled electrons. For the ideal degenerate case, the electron coupling parameter is only density-dependent. In a temperature-density diagram, the line defined by $\Gamma_{ee} = 1$ strongly changes its characteristics in the WDM domain (see figure 2.1).

The measurement of warm dense matter properties is a strong challenge. Because of the resulting thermodynamic parameters, WDM is a very short-lived (ns) state under laboratory conditions and large, homogeneous samples are difficult to produce. Additionally, warm dense matter is generally opaque for visible light. Therefore, measurements of the processes inside a sample volume can exclusively be realized using X-rays or particle beams whereas the, in the field of plasma physics, popular and well-proven optical emission spectroscopy gives only information from the sample surface.

For a sufficient theoretical description of WDM, methods are necessary which unambiguously give the right results. A very promising tool are so-called first-principle or *ab-initio* (Latin: "from the beginning") simulations which only need the most basic physical laws as input [Kresse and Hafner, 1993; Kresse and Furthmüller, 1996]. A drawback is that these simulations need too much computational effort to obtain quick results. Therefore, it is useful to introduce more approximate models

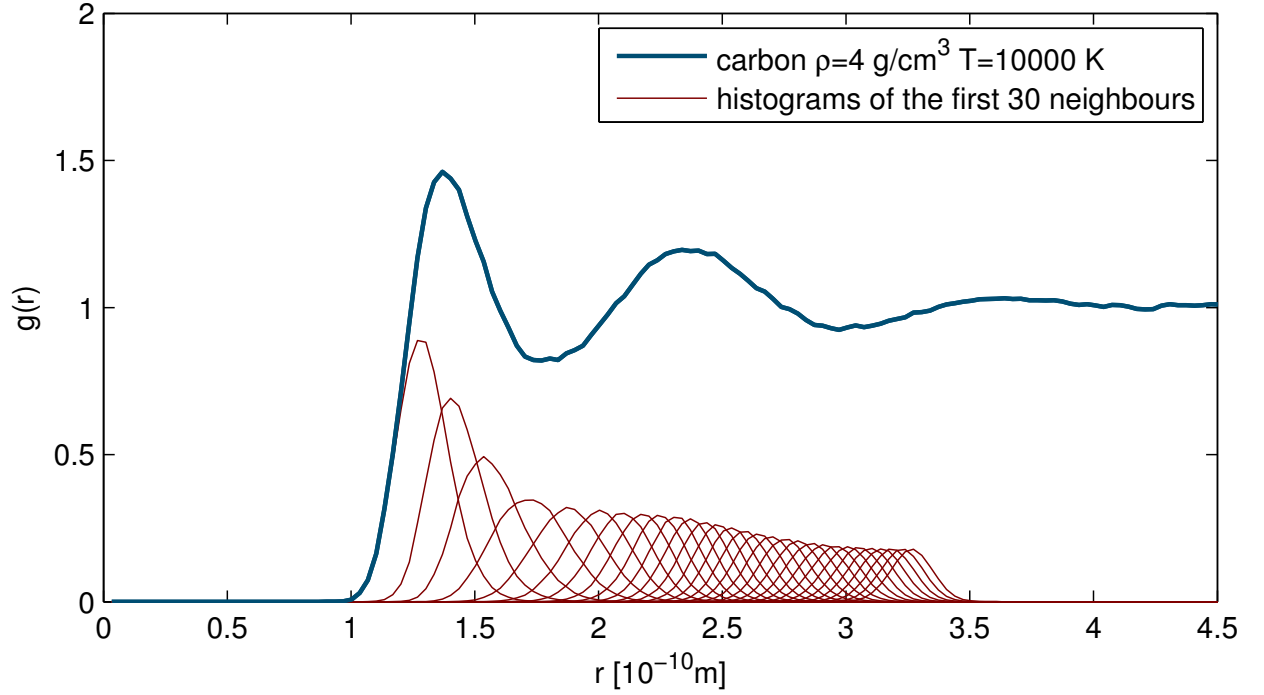


Figure 2.2: Pair correlation function of warm dense carbon with density 4 g/cm³ and 10000 K temperature. The single atom histograms of the first 30 nearest neighbors are also shown. The calculation of the distribution function was performed by J. Vorberger using density functional theory in combination with molecular dynamics (DFT-MD).

and test those against *ab-initio* simulations and experiments. An example for such an intermediate model is the hypernetted chain (HNC) approach [Wünsch et al., 2009].

2.2 Radial distribution function

A quantity, which illustrates many properties of warm dense matter is the atomic or ionic radial distribution function which additionally forms a bridge between theory and experiments because it is accessible for both. The radial distribution function is a special case of the pair correlation function $g(\vec{r}_1, \vec{r}_n)$, which gives the probability to find an atom at position \vec{r}_n if a reference atom is placed at \vec{r}_1 . Using $\vec{r} = \vec{r}_n - \vec{r}_1$, the pair correlation function is defined by

$$g(\vec{r}_1, \vec{r}_n) = g(\vec{r}) = \frac{V}{N} \left\langle \sum_{n=2}^N \delta(\vec{r} - \vec{r}_n) \right\rangle = \frac{V(N-1)}{N} \langle \delta(\vec{r} - \vec{r}_1) \rangle, \quad (2.6)$$

where N is the number of atoms in a volume V , $\delta(\dots)$ is the Dirac delta function and the angle brackets $\langle X \rangle$ mark the ensemble average of a quantity X . For an isotropic material, the pair correlation function is spherically symmetric and only depends on the atomic distance $r = |\vec{r}|$. In this case, $g(\vec{r}) = g(r)$ is also called the radial distribution function. Considering an ideal gas which is completely uncorrelated in terms of particle positions, the pair correlation function is simply given by $g(r)=1$. For interacting materials, like warm dense matter, the radial distribution function can be calculated from the interaction potential via Monte Carlo methods or using the Ornstein-Zernike equations in combination with hypernetted chain theory [Wünsch, 2011]. However, the basic problem concerning warm dense matter is, that the interaction potential is just not yet known for this complicated state of matter. At present, there are two ways to overcome this

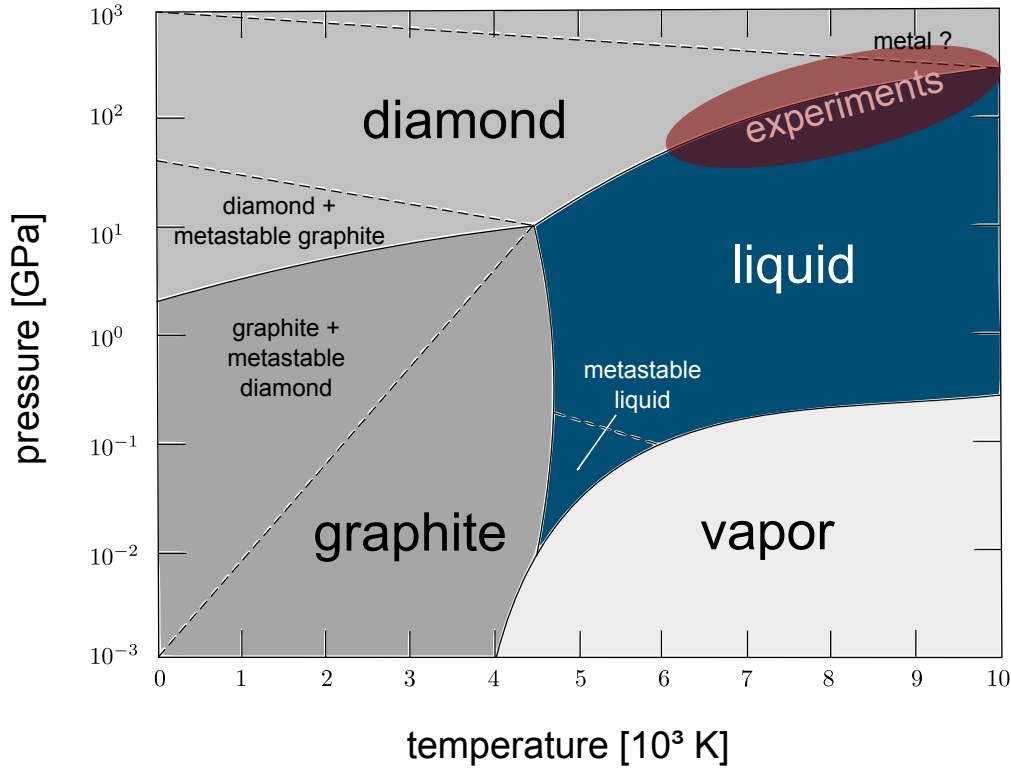


Figure 2.3: Carbon phase diagram [Bundy, 1989; Zazula, 1997]. The upper right quarter in this diagram is poorly understood so far and further investigation is needed. The area marked in red roughly shows the region in temperature and density space which is accessed by the experiments presented in this thesis.

drawback: experiments (which are very difficult) and the already mentioned *ab-initio* simulations (which need large computational effort). The latter are typically build-up as follows: A small sample cell is filled with atoms at given temperature and density. The interaction of the electrons is then determined via a full quantum calculation using the density functional theory (DFT). The behavior of atoms (or ions) is treated by the simple classical laws of motion due to the forces given by the electronic interaction (molecular dynamics - MD). The DFT-MD method for the calculation of the radial distribution function is explained in more detail in chapter six.

An example for such a calculation for carbon in a warm dense matter state is shown in figure 2.2. At small distances $g(r)$ equals zero due to the finite volume of the reference carbon atom. The following peaks at intermediate r indicate the distances where a second atom is preferably found in respect to the reference atom. Exemplarily, the single atom histograms of the first nearest neighbors are also shown. Going to larger distances, there are no more correlations, thus $\lim_{r \rightarrow \infty} g(r) = 1$. This is very similar to the radial distribution function of a liquid, however, the atomic or ionic potential is very different compared to atoms in liquids at room temperature. In fact, for the shown example it is not yet clear whether carbon is a metallic liquid with quasi-free electrons in this regime or not [Gericke, 2012]. In general, carbon is an interesting material for warm dense matter studies which is emphasized in the following section.

2.3 Warm dense carbon

Carbon is a practical element for the first steps in warm dense matter research: As carbon is a low-Z element, calculating real results from theoretical models, including *ab-initio* simulations, is only

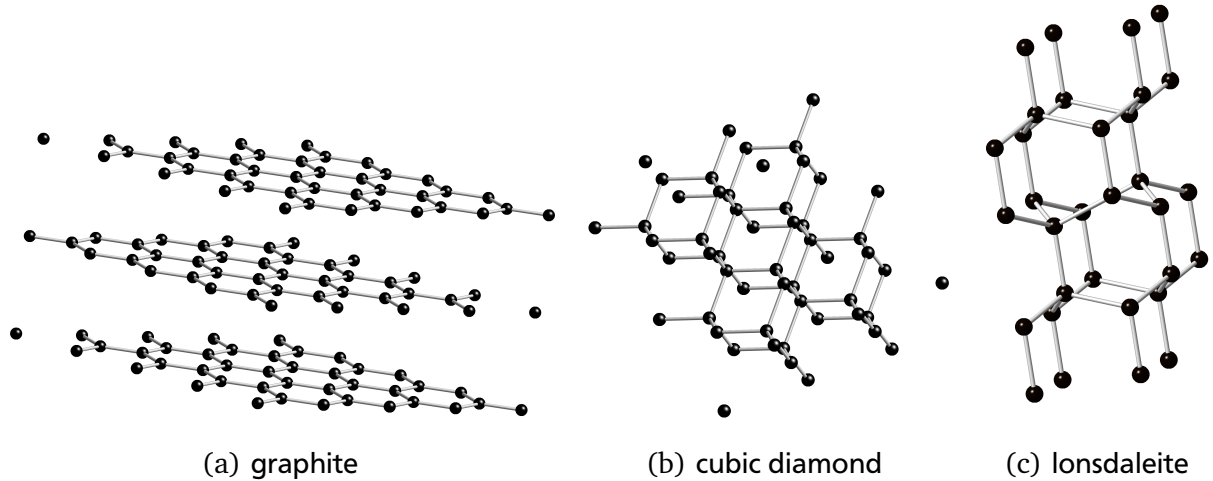


Figure 2.4: Crystal phases of carbon: cubic diamond and lonsdaleite (hexagonal diamond) can be produced by shock compression of graphite.

difficult but not impossible with the computational power available today. Additionally, all forms carbon are, under normal conditions, relatively easy to handle in the laboratory. Furthermore, the carbon phase diagram in the warm dense matter regime is very interesting: The graphite-diamond, graphite-liquid and diamond-liquid coexistence lines all pass a large region of warm dense matter states (see figure 2.3). The graphite-diamond and graphite-liquid transitions are relatively well characterized at moderate pressures and moderate temperatures. Few ten GPa and few thousand kelvins can be reached by experiments with samples set under static pressure by piezoelectrical materials or diamond anvil cells which are then heated externally. Higher pressures, exceeding 100 GPa in combination with temperatures ≥ 5000 K, can only be realized by using very intense particle beams or alternatively, by shock compression experiments. These pressures are relevant for investigating the diamond-liquid transition. Starting with diamond samples, pressures of at least ~ 600 GPa have to be realized to form liquid carbon in a shock wave. In the last decade, sophisticated experiments at the OMEGA laser facility in Rochester [Bradley et al., 2004; Eggert et al., 2009] and the Z-machine at the Sandia National Laboratory in Albuquerque [Knudson et al., 2008] were able to measure a phase transition to a metallic liquid state by shock compression of pure diamond samples to this pressure regime. However, the diagnostic methods applied in these experiments rely on samples which are optically transparent in the initial state. Therefore, only perfectly mono-crystalline diamond samples were compressed in these experiments. However, the investigation of the diamond solid-liquid phase transition at pressures of 100 GPa to 300 GPa by shock compression needs graphite as initial state. Therefore, the optical diagnostics cannot access the shock front inside the samples and X-rays are needed.

Concerning shock compression of graphite, there are many experiments using explosives which observed the graphite-diamond transition starting at ~ 20 GPa [Gust, 1980; Nellis et al., 2001]. The final state of this transition can either be cubic diamond or hexagonal diamond. The latter is also called "lonsdaleite" [Bundy and Kasper, 1967], which is named after the crystallography scientist Kathleen Lonsdale (1903-1971), who discovered the planar-hexagonal structure of benzene (see figure 2.4). The formation of either lonsdaleite or diamond by shock compression of graphite can be influenced by varying the crystal plane orientation and by adding different additives [Kurdyumov et al., 2012]. These transitions are expected to happen on a very fast timescale, going from roughly a few nanoseconds at the transition onset at 20 GPa [Erskine and Nellis, 1991] to below 1 ps at higher pressures [Mundy et al., 2008].

Going to stronger shock compression experiments with graphite, there are no reliable data of the subsequent transition to the liquid and corresponding theories, even *ab-initio* simulations, are not in agreement [Grumbach and Martin, 1996; Wang et al., 2005; Correa et al., 2006, 2008]. Pressures from ~ 80 [Grover, 1979] to ~ 300 GPa [Nellis et al., 2001] have been proposed for the melting threshold of shock-compressed graphite which was initially in a state with ideal crystal density of 2.26 g/cm^3 . Starting with porous polycrystalline samples of lower density, this threshold is expected to be at lower pressures [Batani et al., 2004] because shock compression of porous samples results in higher temperatures for a given pressure (compare section 3.5.2). Up to now, there has been only one experiment which seemed to have observed a transition to the liquid with a large volume change at ~ 60 GPa [Alder and Christian, 1961]. These findings, however, could never be reproduced and therefore, these results are nowadays believed to be incorrect [Gust, 1980]. In fact, modern calculations show that the volume change of this transition is relatively small [Wang et al., 2005]. Therefore, it is very difficult to resolve the melting process just by using the classical measurement of shock and particle velocity. Essentially, the solid-liquid phase transition of shock-compressed graphite has not been measured reliably so far.

As mentioned before, X-rays, which are able to access the processes inside the sample, are a promising alternative. In comparison to simple radiography, X-ray scattering cannot only measure the propagation of the shock but also the microscopic structure inside the sample [Glenzer and Redmer, 2009]. Thus, strong changes in the structure due to phase transitions induced by shock can be measured directly [Garcia Saiz et al., 2008; Kugland et al., 2009]. This is also the method of choice in the experiments presented in this thesis and is explained in detail in chapter four. Prior to that, the physics of laser-driven shocks and the laser-based generation of bright X-ray pulses is introduced in the following chapter.

3 Laser plasma interaction

The experiments and simulations in the framework of this thesis deal with laser-driven shocks to generate a warm dense matter state of carbon. Additionally, laser-generated X-rays were used for the characterization of this state. Both experimental techniques have their origin in the physics of laser-plasma interactions and hydrodynamics. A very brief overview on the relevant phenomena for the applied laser intensities in the region between 10^{13} W/cm² and 10^{15} W/cm² is given in this chapter.

3.1 Basic properties of a laser-driven plasma

Exceeding intensities of 10^9 W/cm², light is able to create plasma on the surface of a solid state sample. Plasma is a state of matter where the atoms are at least partially ionized. Thus, a plasma consists of free electrons and ions with relating number densities $n_{e,\text{free}}$ and $n_i = n_{e,\text{free}}/Z_i$ where Z_i is the mean charge state of the ions. Considering a laser interacting with a solid state surface, the electromagnetic wave couples on existing free electrons which are subsequently accelerated and generate additional free electrons by collisions with neutral atoms or ions. The emerging plasma sheath on the target surface expands with a characteristic velocity which resembles, in good approximation, the propagation speed (sound velocity) of an ion-acoustic wave in a plasma [Drake, 2006]:

$$c_{s,i} = \sqrt{\frac{Z_i k_B T_e + 3k_B T_i}{M_i}}. \quad (3.1)$$

Here, k_B is the Boltzmann constant, T_e the electron temperature, T_i the ion temperature and M_i the mass of the ions. Under the assumption of an isothermal expansion, an exponentially decreasing density profile is formed on the target surface. The laser light, which heats the plasma, is only able to penetrate into the plasma to the so-called critical free electron density [Eliezer, 2002]

$$n_{\text{crit}} = \frac{\omega_L^2 m_e \epsilon_0}{e^2} = \frac{1,1 \times 10^{27}}{(\lambda_L/\text{nm})^2} \text{cm}^{-3}, \quad (3.2)$$

which is directly defined by the laser frequency ω_L (or, more practical, the laser wavelength λ_L), the electron mass m_e , the dielectric constant ϵ_0 and the elementary charge e . At the critical electron density the laser frequency equals the electron plasma frequency [Eliezer, 2002]

$$\omega_{p,e} = \sqrt{\frac{n_{e,\text{free}} e^2}{m_e \epsilon_0}}. \quad (3.3)$$

This means that the electrons can dynamically follow the oscillations of the laser field, shield it and as a consequence stop the propagation of the light wave. For a laser wavelength $\lambda_L = 1064$ nm, the critical free electron density is $\sim 1 \times 10^{21}$ cm⁻³, which is, depending on the material, roughly of the order of one percent of a typical solid state density.

The laser-plasma interaction can be divided into three different parts: The absorption region, the transport region and the compression region (see figure 3.1). These zones, especially emphasizing the latter one, will be discussed in the following sections of this chapter.

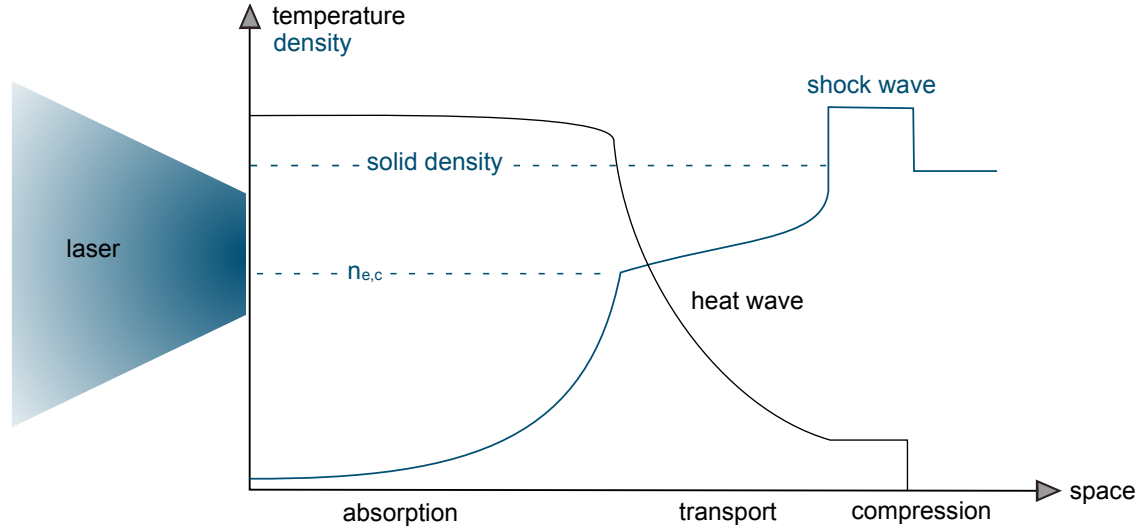


Figure 3.1: Schematic picture of the different regimes that evolve when a high energy laser hits a solid density sample material.

3.2 Absorption

As stated above, laser light is only absorbed in the plasma regime where the free electron density is below the critical density n_{crit} . This absorption region is also called the plasma corona. If laser light is able to penetrate the absorption region to the critical density, the light will be reflected back into the corona. Dealing with relatively low intensities (i.e. $I_L \lambda_L^2 < 10^{15} \text{ W/cm}^2 \mu\text{m}^2$ where I_L is the incident laser intensity), the laser absorption is dominated by inverse bremsstrahlung which is the absorption of a photon by an electron within a collision with another electron or ion. The absorption coefficient μ_{ib} of inverse bremsstrahlung is given by [Eliezer, 2002]

$$\mu_{ib} = \frac{\sqrt{2}\pi n_{e,\text{free}}^2 Z_i e^6 \lambda_L^2 \ln \Lambda}{48\pi^4 c^3 \epsilon_0^3 (m_e k_B T_e)^{3/2}} \left(1 - \frac{n_{e,\text{free}}}{n_{\text{crit}}}\right)^{-1/2}, \quad (3.4)$$

where c is the speed of light and $\ln \Lambda$ is the logarithm of the ratio of maximal and minimal impact parameter of an electron-ion collision, the so-called "Coulomb logarithm". The attenuation of the laser intensity I_L after propagating a distance x is then

$$I_L(x) = I_{L,0} \exp\left(-\int_0^x \mu_{ib}(x') dx'\right), \quad (3.5)$$

where $I_{L,0}$ is the initial laser intensity. Going to incident intensities satisfying $I_L \lambda_L^2 \gtrsim 10^{15} \text{ W/cm}^2 \mu\text{m}^2$, laser absorption due to parametric instabilities like resonance absorption becomes more and more important. Typically, these instabilities result in two temperature electron distribution functions due to the generation of hot, suprathermal electrons.

3.3 Transport mechanisms

A fraction of the energy that is deposited in the corona by the laser is transported from the critical density to the transport and compression region. The involved processes are collisions (heat conduction) and radiation transport. Both mechanisms are presented briefly in this section.

3.3.1 Heat conduction

In every medium with a temperature gradient, a heat flux \vec{j}_{therm} is generated which tends to reduce this gradient. The change in energy density per unit time due to thermal conductivity is then given by:

$$q_{\text{therm}} = -\vec{\nabla} \cdot \vec{j}_{\text{therm}} = \vec{\nabla} \cdot (\kappa \vec{\nabla} T), \quad (3.6)$$

where κ is called the heat conductivity coefficient. For a plasma, it is a good assumption that only the electrons contribute to this heat transport. However, the electron mean free path is mainly defined by the electron-ion collision frequency. In the widely-used Spitzer-Harm model for an ionized gas, a small perturbation of the local electron velocity distribution due to a temperature gradient is assumed. Neglecting electron-electron collisions, κ is given by [Kruer, 2003]

$$\kappa = \left(\frac{4\pi\epsilon_0}{e^2} \right)^2 \frac{4k_B^{7/2} T_e^{5/2}}{Z_i m_e^{1/2} \ln \Lambda}. \quad (3.7)$$

Notably, the Spitzer-Harm heat conductivity coefficient strongly scales with temperature but does not depend on density. However, the regime of application is limited. For small values of Z_i a correction factor taking into account the electron-electron collisions has to be included. Finally, for very strong temperature gradients, as for example at the critical density of a laser-plasma interaction, the perturbative approach completely fails and the heat flux is strongly overestimated in this case. Therefore, an even more simple, but also very common model of the electron heat transfer is introduced: The so-called flux-limited transport model. Here, the maximum possible free-streaming heat flux, moving with the thermal velocity of the electrons v_{Th} , is considered [Drake, 2006]:

$$j_{\text{free}} = n_{e,\text{free}} k_B T_e v_{\text{Th}}. \quad (3.8)$$

However, j_{free} usually overestimates the heat flux j within a real physical environment. Therefore a correction factor, called the flux-limiter, f , is introduced [Kruer, 2003]:

$$j_{\text{therm}} = f j_{\text{free}} = f n_{e,\text{free}} k_B T_e v_{\text{Th}} = f n_{e,\text{free}} k_B T_e \sqrt{\frac{k_B T_e}{m_e}}. \quad (3.9)$$

A typical value for the flux limit factor is $f \approx 0.1$ [Drake, 2006] or even lower (for example if parametric instabilities are involved [Kruer, 2003]). Codes which model laser plasma interactions often calculate the heat flux for both flux-limited transport and the Spitzer-Harm model for every single grid cell. The model which gives the smaller value for the heat flux will then be used in the particular calculation step.

3.3.2 Radiation transport

As the energy density of a radiation field is proportional to T^4 , radiation transport gives a relevant contribution to the energy flux in plasmas and gets dominant for high temperatures and low densities. For the case of very dense plasma where blackbody radiation can be assumed, the radiation flux σT^4 (where σ is the Stefan-Boltzmann constant) can easily be compared to the energy flux given by the flux-limited heat transport model. The temperature where the energy transfer is equal for radiation and heat transport is then

$$T_e = \left(\frac{f n_{e,\text{free}} k_B^{3/2}}{\sigma m_e^{1/2}} \right)^{2/5}. \quad (3.10)$$

Thus, for a dense plasma with an electron density of $n_e = 10^{23} \text{ cm}^{-3}$, the electron temperature T_e must exceed $\sim 230 \text{ eV}$ that the radiation transport will be the dominant energy exchange mechanism. However, independent from plasma conditions radiation is always dominating the energy transport to regions which are not yet reached by electron heat conduction. This is because electron heat conduction travels in the order of the material's sound speed. Radiation instead propagates with the speed of light. This is a significant issue concerning laser-driven shock waves. Soft and hard X-rays, which are produced in high numbers close to the critical density, can cause considerable preheating of the cold target material in front of the shock wave. Hence, the initial state can be changed in such a way that the characterization of the shock wave becomes impossible. Therefore, radiation transport has to be included in a simulation treatment of laser-driven shock waves.

For the calculation of the radiation transport the general expression for the spectral energy density of a radiation field has to be considered:

$$u_\omega(\vec{r}, t) = \hbar\omega \int d\Omega f_\omega(\vec{r}, t), \quad (3.11)$$

where $f_\omega(\vec{r}, t)$ is the time-dependent spectral photon distribution function. The spectral radiation energy flux in the direction of a unit vector \vec{n} is then given by

$$\vec{S}_\omega(\vec{r}, t, \vec{n}) = \hbar\omega c \int d\Omega f_\omega(\vec{r}, t) \vec{n} \quad (3.12)$$

The spectral radiation energy density and the spectral radiation energy flux have to fulfill a continuity equation, the so-called radiation transport equation

$$\frac{\partial u_\omega}{\partial t} + \vec{\nabla} \cdot \vec{S}_\omega = c\kappa_\omega(u_{\omega, \text{Planck}} - u_\omega), \quad (3.13)$$

where the terms on the right hand side of this equation define the radiation sinks and sources. $u_{\omega, \text{Planck}}$ is the energy density of a perfect blackbody radiator and κ_ω is the frequency-dependent opacity of the material. Modeling plasma properties, the partial time derivative can usually be neglected as a change of the radiative energy density will propagate with the speed of light which is much larger than plasma flow velocities. Therefore, the radiation transport equation reduces to

$$\vec{\nabla} \cdot \vec{S}_\omega = c\kappa_\omega(u_{\omega, \text{Planck}} - u_\omega). \quad (3.14)$$

3.4 Ablation pressure

The expanding corona of the laser plasma generates a large pressure on the target surface. This is called the ablation pressure and an analytic description can be obtained by considering the heat transport from the corona through the critical density to the transport layer. Hereby, the simple model of the flux-limited heat transport can be applied (see section 3.3.1): Assuming that about half of the laser irradiance I_L is absorbed in the thin corona [Drake, 2006], the remaining 50 % are available for heat transport at the critical density n_{crit} :

$$\frac{1}{2}I_L = j_{\text{therm}} = f n_{\text{crit}} k_B T_e \sqrt{\frac{k_B T_e}{m_e}}. \quad (3.15)$$

From this equation an approximation of the electron temperature in the transport domain can be deduced for $f=0.1$:

$$T_e = 1.7 \left[\left(\frac{I_L}{10^{14} \text{W/cm}^2} \right) \left(\frac{\lambda_L}{1 \mu\text{m}} \right)^2 \right]^{2/3} \text{ keV.} \quad (3.16)$$

The ablation pressure P_{abl} is equal to the momentum flux $\rho \vec{v}^2$ through the critical density. As mentioned before, the ablation velocity is approximately the sound velocity of an ion-acoustic wave. The velocity relevant for the momentum flux is, however, roughly $\sqrt{2}$ times the sound velocity [Drake, 2006]. This gives:

$$P_{\text{abl}} \approx 2\rho c_{s,i}^2 = 2n_{\text{crit}} \frac{Zk_B T_e + 3k_B T_i}{Z}. \quad (3.17)$$

Using equation (3.16) and assuming fully ionized carbon ($Z=6$) and $T_i = T_e/3$, which is a typical value for laser coronae [Drake, 2006], the ablation pressure is then given by

$$P_{\text{abl}} \approx 2n_{\text{crit}} k_B T_e \frac{Z+1}{Z} = 700 \left(\frac{I_L}{10^{14} \text{W/cm}^2} \right)^{2/3} \left(\frac{\lambda_L}{1 \mu\text{m}} \right)^{-2/3} \text{ GPa.} \quad (3.18)$$

This formula (sometimes with small simulation based corrections of the scaling prefactor) is widely used in inertial confinement fusion research [Atzeni and Meyer-ter-Vehn, 2004]. Some more advanced concepts and scaling formulas of the ablation pressure can be found in [Batani et al., 2003].

3.5 Shock waves

The ablation pressure induced by the expanding corona usually drives a shock wave into the cold sample material. The shock wave is supersonic regarding the undisturbed material and carries energy forward. Thereby, the medium undergoes compression, heating and acceleration. To describe this process, the Euler fluid equations are considered in conservative form which means that mass, momentum and energy equations all have the form of a continuity equation [Drake, 2006]:

$$\frac{\partial \rho}{\partial t} + \vec{\nabla}(\rho \vec{v}) = 0 \quad (3.19)$$

$$\frac{\partial(\rho \vec{v})}{\partial t} + \vec{\nabla}(\rho \vec{v} \vec{v} + P) = \vec{f}_{\text{ext}} \quad (3.20)$$

$$\frac{\partial(\rho \epsilon + \frac{1}{2} \rho \vec{v}^2)}{\partial t} + \vec{\nabla} \left[\vec{v} \left(\rho \epsilon + \frac{1}{2} \rho \vec{v}^2 + P \right) \right] = q \quad (3.21)$$

Here, \vec{v} is the fluid velocity, ρ its density and ϵ the fluid's specific internal energy. The pressure P is a tensor in the most general case of a non-isotropic medium. \vec{f}_{ext} is the external force density and q is an additional source or sink term of energy, which can be, for example, heat conduction, radiation transport or absorbed laser energy. For the typical one-dimensional shock wave solution of the Euler fluid equations, it is assumed that external forces, heat conduction and radiation transfer can be neglected, which means $\vec{f}_{\text{ext}}=0$ and $q=0$. Thus, the conservation laws for mass, momentum and energy in one dimension give:

$$\frac{\partial \rho}{\partial t} = -\frac{\partial}{\partial x}(\rho v) \quad (3.22)$$

$$\frac{\partial(\rho v)}{\partial t} = -\frac{\partial}{\partial x}(\rho v^2 + P) \quad (3.23)$$

$$\frac{\partial(\rho \epsilon + \frac{1}{2} \rho v^2)}{\partial t} = -\frac{\partial}{\partial x} \left[\rho v \left(\epsilon + \frac{1}{2} v^2 + \frac{P}{\rho} \right) \right] \quad (3.24)$$

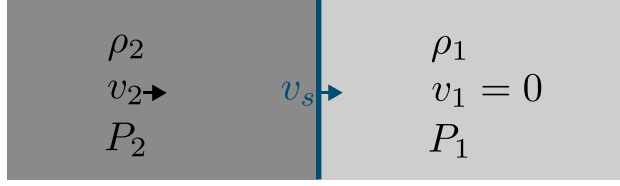


Figure 3.2: One dimensional shock wave scenario in the laboratory frame.

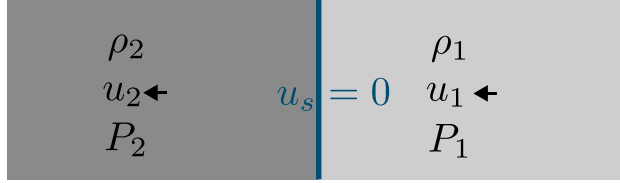


Figure 3.3: One dimensional shock wave scenario in the shock wave frame.

Now, a scenario as in figure 3.2 is considered. A one-dimensional shock wave passes an undisturbed material at rest ($v_1=0$) with density ρ_1 and pressure P_1 . Thereby, the shock front travels with the shock velocity v_s which is larger than the sound velocity of the undisturbed medium. Otherwise, the discontinuity at the shock front would not be a stable solution of the Euler equations. The compressed and accelerated material behind the shock front with density ρ_2 and pressure P_2 is moving with the so-called particle velocity v_2 which is obviously smaller than v_s . For a very simple derivation of the relations which connect the thermodynamic parameters of undisturbed and shocked medium, the velocities can be transferred into a coordinate system where the shock front is at rest (the so-called shock wave frame). The transformation of the velocities is then simply given by:

$$u_{1,2,s} = v_{1,2,s} - v_s, \quad (3.25)$$

where $u_{1,2,s}$ are the related velocities in the shock wave frame. In this picture (see figure 3.3) the undisturbed material moves with velocity u_1 towards the stationary shock and after passing the shock front, the material instantaneously moves with velocity u_2 . This is a stationary system which means that the partial time derivatives in the equations (3.22) to (3.24) are zero at every point in the shock wave frame. Thus, mass, momentum and energy flows are similar on both sides of the shock front in this reference system. This is a completely intuitive picture as there are no sources or sinks of mass, momentum and energy. Therefore, the flow of mass, momentum and energy from one side into the discontinuity at the shock front has to be same on the other side of the shock in this stationary picture. This directly gives the relations which connect the thermodynamic parameters of both sides, the so-called Rankine-Hugoniot relations:

$$\rho_1 u_1 = \rho_2 u_2 \quad (3.26)$$

$$\rho_1 u_1^2 + P_1 = \rho_2 u_2^2 + P_2 \quad (3.27)$$

$$\rho_1 u_1 \left(\epsilon_1 + \frac{1}{2} u_1^2 + \frac{P_1}{\rho_1} \right) = \rho_2 u_2 \left(\epsilon_2 + \frac{1}{2} u_2^2 + \frac{P_2}{\rho_2} \right). \quad (3.28)$$

Using two equations from these relations, it is possible to eliminate the velocities u_1 and u_2 . Thus, the resulting equation can be simplified to

$$\epsilon_2 - \epsilon_1 = \frac{P_1 + P_2}{2} \left(\frac{1}{\rho_1} - \frac{1}{\rho_2} \right). \quad (3.29)$$

This equation defines all thermodynamic states $(\rho_2, P_2, \epsilon_2)$ which can be achieved by shock compression of an initial state $(\rho_1, P_1, \epsilon_1)$. Applying the equation of state, another variable can be eliminated and the resulting curve in phase space is called the Hugoniot curve. Additionally, equation (3.29) states that, due to shock compression, half of the total compression energy $P\Delta V \propto P\Delta(\frac{1}{\rho})$ is stored as internal energy whereas the other half is needed for the acceleration of the material to the velocity v_2 .

Shock waves are a very useful tool to study the equation of state of materials at high pressures. If all initial conditions are known, the Rankine-Hugoniot relations form a system of three equations which contains five unknown variables. Thus, measuring the two velocities exactly gives the density, pressure and specific internal energy of the shocked material. On the one hand, the measurement of the shock velocity does not pose much experimental difficulties as the shock transit time through a sample can easily be determined by fast modern cameras or interferometry instruments. The particle velocity v_2 , on the other hand, is very hard to access directly. If the shock pressure is not too high ($\lesssim 300$ GPa [Benuzzi-Mounaix et al., 2002]), the particle velocity is connected to the free surface velocity v_{FS} of the shock breakout by the so-called "doubling rule" [Zeldovic and Raizer, 1966; Eliezer, 2002]. This states that the release isentrope of the shock breakout is in good approximation a mirror image of the Hugoniot curve which results in

$$v_{FS} \approx 2v_2. \quad (3.30)$$

This simplification is not applicable for very high pressure shock waves which impose a large change in volume and entropy. Measurements of the thermodynamic properties of these states via the Rankine-Hugoniot relations are only possible by determining the particle velocity directly. This can be achieved in experiments using impactors, so-called flyer plates, to drive the shock [Knudson et al., 2008].

It is to mention that all treatments of shock waves discussed so far are assuming a perfectly planar one-dimensional shock drive. Considering a laser-driven shock, this means that the laser focus has to be homogeneous and by far larger than the sample thickness (at least a factor of two [Eliezer and Mima, 2009]) to guarantee a one-dimensional drive. Otherwise 2D-effects will become important.

3.5.1 Shock waves in solids

The special feature of solids (and also liquids) regarding shock compression is, in comparison to gas states, a strong repulsive force between the atoms in the shocked state. This is why pressures of the order of 100 GPa or even larger are needed to compress solid state samples by at least a factor of two. Therefore, much of the compression energy induced by the shock drive is directly converted to potential energy to overcome the repulsive forces. Only for very strong shock waves ($P \gtrsim 1$ TPa), this so-called cold compression energy is small compared to the thermal energy induced by the simultaneous heating and entropy increase in the shock. In the pressure regime around ~ 100 GPa, which is relevant for the experiments described in this thesis, the cold compression and thermal energy are comparable in magnitude [Zeldovic and Raizer, 1966]. Thus, determining the temperature of the shocked state from the change in specific internal energy is very complicated and requires sophisticated microscopic structure models of the high pressure state.

3.5.2 Porous materials

Regarding equation of state studies, porous materials open the possibility to explore different Hugoniot curves of the same sample material. This is because the different initial density of the

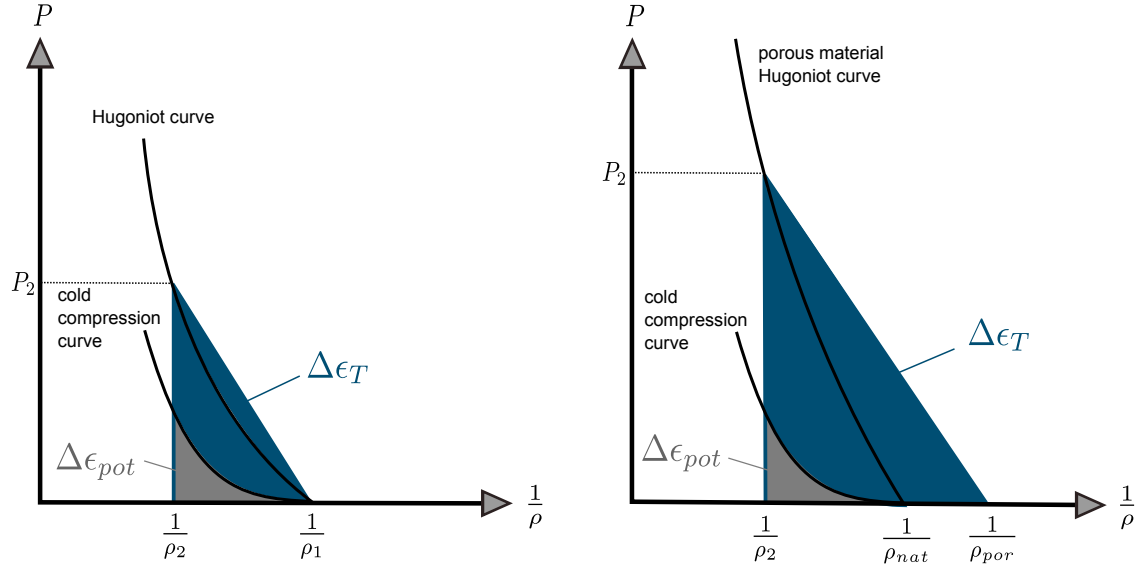


Figure 3.4: Different Hugoniot curves for the natural density (left) and the porous sample (right) compared with the cold compression curve. The specific internal energy changes which go into potential and thermal energy are also shown [Zeldovic and Raizer, 1966].

porous material results in different achievable final states under shock compression. The pressure needed for the compression of the porous material with density ρ_{por} back to its natural density ρ_{nat} is typically orders of magnitude smaller than the pressures of ~ 100 GPa which are relevant for the experiments presented in this thesis. Thus, a porous material undergoing shock compression will first be compressed to the natural density and then follow a Hugoniot curve which is steeper in a pressure-volume diagram than the Hugoniot curve directly starting at the natural density. This is due to the heating during the first compression phase. Additionally, the ratio of thermal internal energy to potential internal energy is much larger for a compressed porous sample than for the same material with continuous natural density. In particular, this means it is easier to reach high temperature states by shock compression using porous materials. This fact can easily be deduced from a pressure-volume diagram as shown in figure 3.4: The specific internal energy change, see equation (3.29), is given by the area of the triangle defined by the points $(\frac{1}{\rho_1}, 0)$, $(\frac{1}{\rho_2}, 0)$ and $(\frac{1}{\rho_1}, P_2)$. The potential energy which is needed to overcome the repulsive forces is given by the gray area under the cold compression curve. For a porous material, the sample is first compressed back to its natural density of the pure material ρ_{nat} . Hereby, the entropy is already increasing and further compression will hence follow a steeper Hugoniot curve. Achieving the same compression, the induced thermal energy is therefore much larger using a porous material. Following this scheme, graphite with a porosity of 10 Vol. % was applied in the experiments presented in this thesis to reach melting of the carbon samples with the available drive laser intensity.

3.5.3 Phase transitions within a shock wave

Shock compressed materials can undergo phase transitions. Starting with a solid at room temperature, these transitions lead to different solid, liquid or dense plasma phases in the final state. Due to the absorption (or release) of latent heat, the Hugoniot curve gets more complicated. Considering a scenario as shown in figure 3.5a: A compression pressure P_A is applied to a sample material. The consequence is that first an intermediate state with Pressure P_M and density ρ_M will be formed before the shocked material will release into the final state. This is because the relaxation (or nucleation) time of a first order phase transition is typically much larger than the time required for

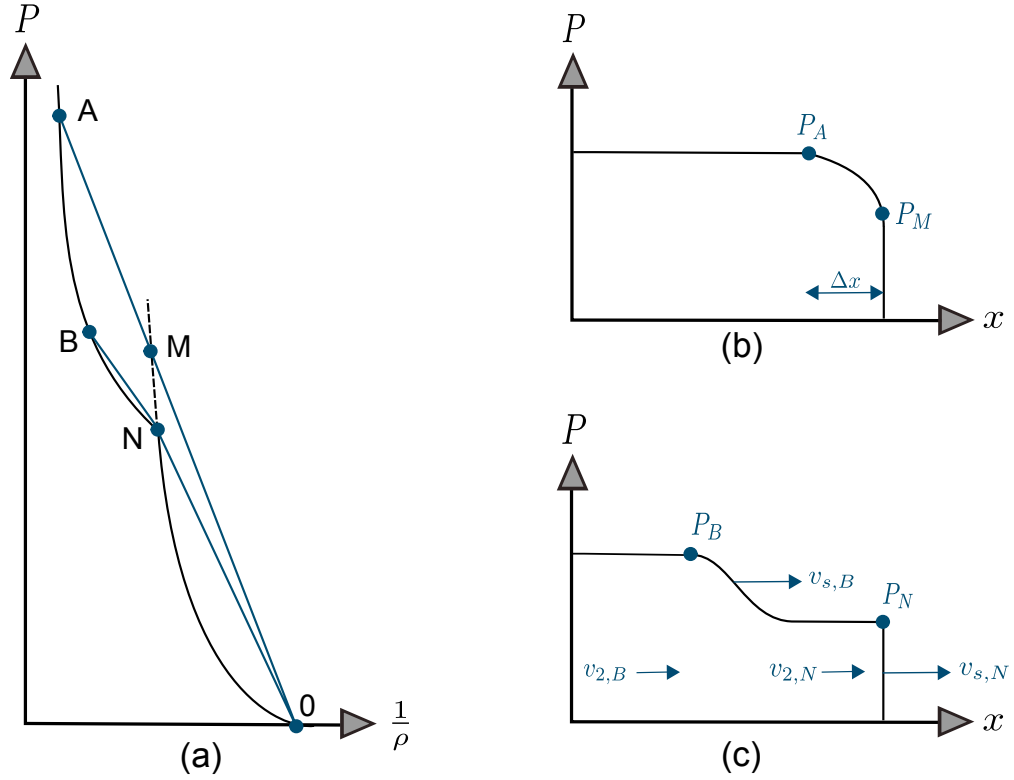


Figure 3.5: Sketch of different scenarios which can evolve due to a phase transition induced by a shock wave: a) Hugoniot in the pressure-volume diagram. b) If the driving pressure is large enough, a static shock with a phase transition zone of length Δx will establish. c) At lower pressures which are just enough to reach the phase transition, a two wave structure will evolve [Zeldovic and Raizer, 1966].

establishing thermodynamic equilibrium after the shock transit. The intermediate state M can be found on the extrapolated Hugoniot curve of the initial phase. As the shock velocity

$$v_s = \frac{1}{\rho_1} \sqrt{\frac{P_2 - P_1}{\frac{1}{\rho_1} - \frac{1}{\rho_2}}} \quad (3.31)$$

is proportional to the square root of the slope of the lines, which connect initial and final state in the diagram, a stationary scenario as in figure 3.5b will evolve. If the compression pressure is smaller, for example P_B , the shock wave can split into two waves. This is because the intermediate state N results in a shock velocity

$$v_{s,N} = \frac{1}{\rho_0} \sqrt{\frac{P_N - P_0}{\frac{1}{\rho_0} - \frac{1}{\rho_N}}} \quad (3.32)$$

which is faster than the shock due to the phase transition relaxation as the slope of N-B is substantially smaller than the slope of 0-N. Therefore the relaxation front moving with velocity

$$v_{s,B} = \frac{1}{\rho_N} \sqrt{\frac{P_B - P_N}{\frac{1}{\rho_N} - \frac{1}{\rho_B}}} + v_{2,N} < v_{s,N} \quad (3.33)$$

is slower than $v_{s,N}$. In this case a scenario as pictured in figure 3.5c will evolve.

3.6 X-ray generation

In addition to the driving of shock waves, laser plasmas were also used for the generation of X-rays within the experiments presented in this thesis. Basically, there are three different elementary mechanisms of X-ray emission in a laser plasma: bremsstrahlung (free-free transition), radiative recombination (free-bound transition) and radiative de-excitation (bound-bound transition). The latter creates line emission which can be used for X-ray scattering applications [Riley et al., 2002; Urry et al., 2006; Kritcher et al., 2007]. The spectral emissivity for a bound-bound transition from a high energy state 2 to a low energy state 1 is:

$$J(\omega) = n_2 A_{21} \frac{\hbar \omega_{21}}{4\pi} g(\omega), \quad (3.34)$$

where n_2 is the population density of the high energy state, A_{21} the spontaneous radiative rate, ω_{21} the frequency of the emitted radiation and $g(\omega)$ the line profile function. To optimize the X-ray yield from one line transition, n_2 has to be maximized. This can be achieved by tuning the temperature (thermal line emission) or by applying non-equilibrium effects (non-thermal line emission). The latter method needs high laser intensities ($\gtrsim 10^{16}$ W/cm²) to be efficient. Collective processes, such as resonance absorption or other parametric instabilities, start dominating the laser absorption mechanism in that intensity regime because the plasma becomes collisionless due to the higher electron temperatures. Resonance absorption and parametric instabilities result in electrons with very high kinetic energy (hot electrons) in the regime from several tens of keV to even several MeV. These high energy electrons penetrate deep into the cold target material surrounding the laser-plasma interaction and can efficiently produce K-alpha line radiation, depending on the target material, up to several tens of keV.

3.6.1 Helium-alpha emission

Looking for photon energies of 1 keV to 5 keV, thermal line emission is up to two orders of magnitude more efficient [Glenzer and Redmer, 2009]. This is especially true for ions where only the two K-shell electrons are left. These ions are called helium-like. As the K-shell electrons are relatively tightly bound compared to those in the L-shell, helium-like ions are very stable over a large temperature interval for a given density. The high density inside the transport region of the laser-plasma interaction results in high collision rates. These conditions favor the excitation of ground state K-shell electrons of helium-like ions to the L-shell ($1s^2 \rightarrow 1s2p$). The following de-excitation ($1s2p \rightarrow 1s^2$) is called the helium- α line transition of the corresponding ion (see figure 3.6). Considering laser-plasmas, this transition has typical spectral characteristics. The decay of the excited state can happen by a singlet ($1P \rightarrow 1S$) or triplet transition ($3P \rightarrow 1S$). The latter is semi-forbidden, i.e. it is only allowed for heavy atoms with strong spin-orbit coupling resulting in overlapping wave functions of $3P$ and $1P$, and is called intercombination line. In addition to these two spectral features helium- α spectra from dense plasmas typically show so-called satellite lines. These emerge when additional spectator electrons are present in the ion. Such a transition for lithium-like ions is for example $1s2p^2 \rightarrow 1s^2 2p$ with a spectator electron in the L-shell (compare figure 3.7). The transition energy of a satellite line is reduced compared to the main transition as the additional electrons reduce the potential seen by the transition electron. Lithium-like ions are however very rare in dense laser plasmas which favor the existence of helium-like ions. Nevertheless these satellite lines are also efficiently produced by the dielectronic recombination process. Here the excessive kinetic energy of the captured electron excites another bound electron. The following de-excitation emits a photon which is reduced in energy due to the spectator electron (see figure 3.8).

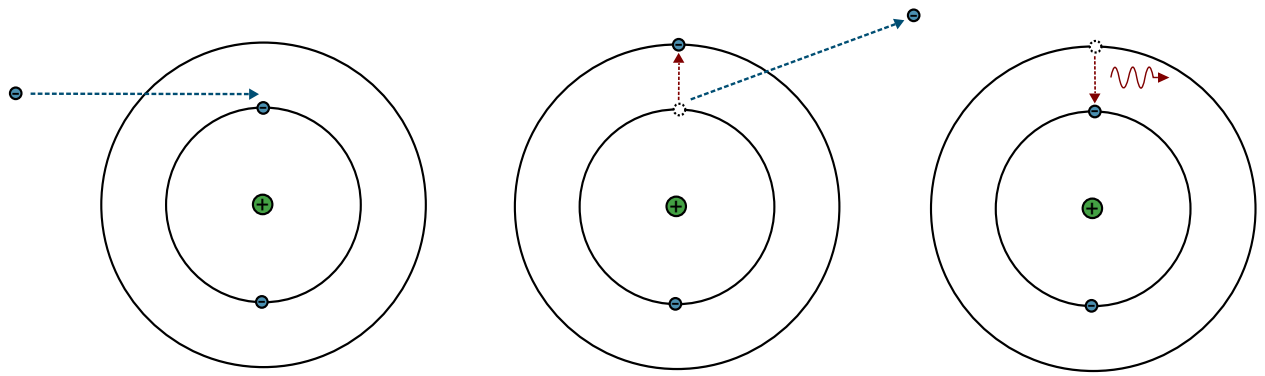


Figure 3.6: Diagram of the helium- α transition: One K-shell electron of a helium-like ion is excited by the impact of a free electron. The latter is deflected whereas the bound electron is transferred to the L-shell for a short time. This excited state then decays by spontaneous emission of the corresponding helium- α photon.

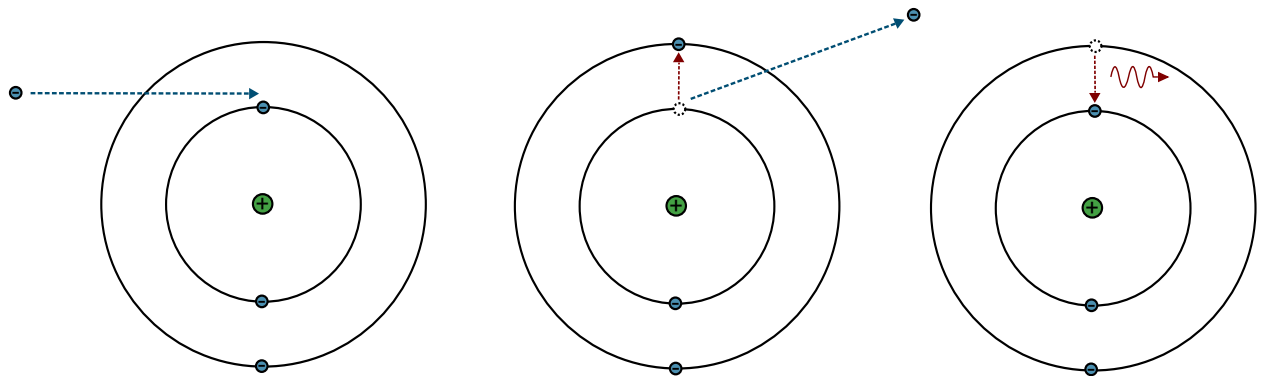


Figure 3.7: Satellite line: A spectator electron is added to the excitation and de-excitation process of figure 3.6. Due to shielding of the nuclear potential the emitted photon energy is slightly reduced.

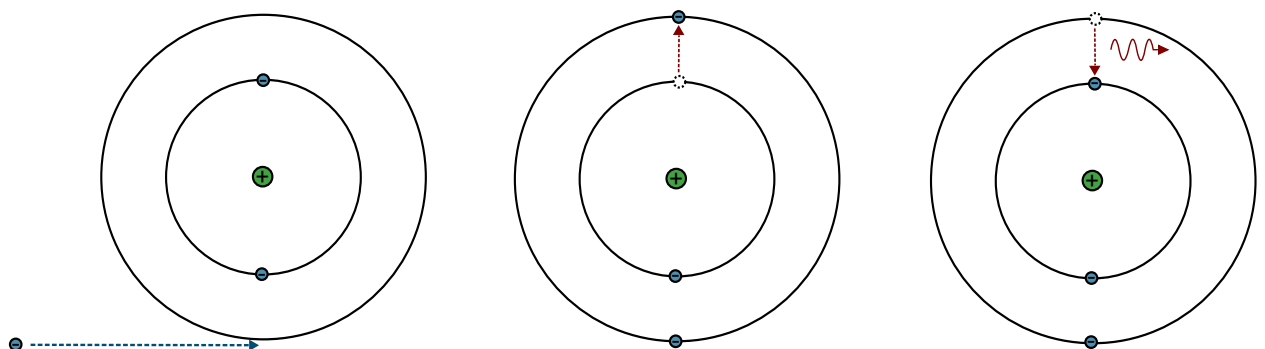


Figure 3.8: Dielectronic satellite: In the dielectronic recombination process a free electron is captured into an outer shell and the remaining kinetic energy additionally excites one K-shell electron. The following decay again results in a photon that is slightly reduced in energy compared to the pure helium- α transition.

Considering laser pulses in the nanosecond regime, the duration of a laser-driven helium- α radiation flash is typically in the order of the laser pulse duration. The onset of the X-ray flash is slightly delayed relative to the laser as it takes some time to produce helium-like ions in the transport region. Additionally, it needs a while for the laser plasma to cool down after the laser drive is finished. This results in X-ray pulses which are slightly shifted in time compared to the drive laser but have in good approximation the same duration. This behavior was verified experimentally by various groups using for example X-ray streak cameras [Riley et al., 2002].

The X-ray source which was applied in the experiments presented in this thesis was chosen to be thermal line emission from helium-like titanium (in particular the titanium helium- α line at 4.75 keV). This radiation can be driven very efficiently by lasers and has been used successfully in various X-ray scattering experiments for the characterization of warm dense matter [Riley et al., 2000; Glenzer et al., 2003; Gregori et al., 2004]. The special spectral characteristics of the titanium helium- α transition are presented in more detail in section 7.2 whereas the next chapter is about scattering of the produced X-rays from warm dense matter samples.

4 X-ray scattering

Scattering of electromagnetic radiation is a powerful and therefore very popular technique to characterize various states of matter. This method offers a measurement of physical parameters nearly without perturbing the samples, if these are relatively transparent for the probe radiation. Working close to transparency also reduces inaccuracies caused by multiple scattering events. Therefore, the microscopic structure of solid density cold matter samples is typically investigated with high energy X-rays, which are mostly produced by synchrotron radiation facilities in modern days. In terms of classical plasma physics, scattering of visible light is a standard technique to measure temperature, free electron density and degree of ionization of a thin plasma. This technique is, for example, well-established in magnetic confinement fusion research. Dealing with warm dense matter samples, there are many difficulties that have to be overcome: WDM samples are usually very short-lived ($\sim 10^{-9}$ s), small ($\sim 10^{-4}$ m) and opaque for visible light. Thus, short X-ray pulses with very high photon numbers are needed for the characterization of warm dense matter by scattering of electromagnetic radiation. The only X-ray sources that at present fulfill all these requirements are laser-produced plasmas [Riley et al., 2002; Urry et al., 2006; Kritcher et al., 2007] and, very lately, X-ray free electron lasers like the Linac Coherent Light Source (LCLS) facility in Stanford [Arthur et al., 2002; Vinko et al., 2012] or the European XFEL which is currently under construction at DESY in Hamburg [DESY XFEL Project Group, 2006].

There are various types of scattering of electromagnetic radiation which are mostly named historically after the corresponding way-leading scientists. Elastic scattering of radiation from tightly bound electrons of an atom is usually called Rayleigh scattering. Inelastic scattering from bound electrons, which are transferred to an excited state during the scattering process, is called Raman scattering. Inelastic scattering from free or, compared to the energy transfer within the scattering process, weakly bound electrons, where the energy of the incident photons is much smaller than the rest mass of the electrons, is called Thomson scattering. Going to higher photon energies, where relativistic effects become more and more important, the common term is Compton scattering. Dealing with partially ionized plasmas of warm dense matter research, Rayleigh, Raman and Thomson scattering are often used in combination to characterize sample properties. However, these three scattering types converge to the single term "X-ray Thomson scattering (XRTS)" in various publications of the WDM research community [Glenzer and Redmer, 2009]. This is basically done because of practical convenience but also because it is possible to describe all these scattering types with the theory of Thomson scattering of electromagnetic radiation and the dynamic structure factor [Sheffield, 1975; Gregori et al., 2003, 2004].

An effective analysis of experimentally obtained scattering spectra relies on a proper theoretical treatment of the dynamic structure factor. This is still ongoing research because, as described in chapter two, warm dense matter is a complicated state of matter, often containing partially ionized atoms and partially degenerated electrons. Especially the interpretation of the shape of spectrally resolved scattering signals usually involves a large theoretical effort [Wünsch, 2011]. Due to the strong increase of available computational power during the last decade, the use of *ab-initio* methods becomes more and more popular and practical for the calculations of the dynamic structure factor of warm dense matter states [Garcia Saiz et al., 2008].

In the experiments that were performed in the framework of this thesis, a combination of Rayleigh

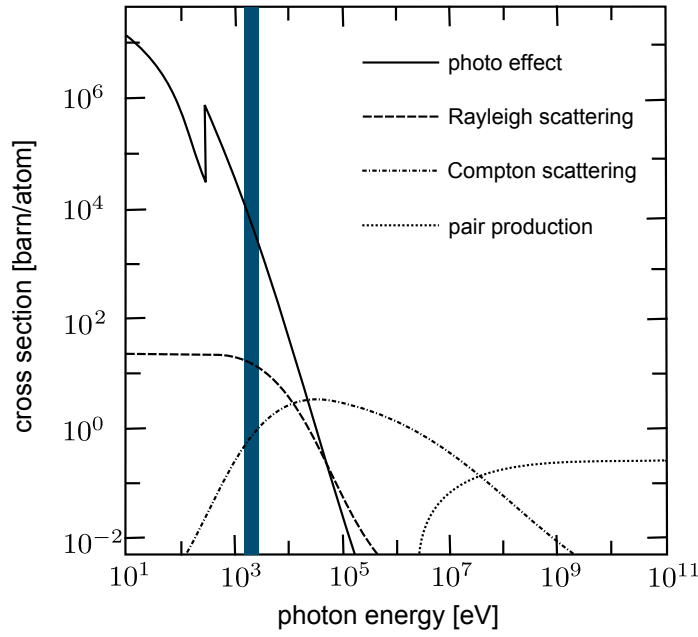


Figure 4.1: Diagram of the photoabsorption cross section of graphite in dependence of the probe radiation photon energy [Hubbell et al., 1980]. The colored area highlights the region around the photon energy 4.75 keV which was applied in the experimental work of this thesis. Multiple scattering can be neglected because of the small scattering cross sections. The dominating absorption process at a photon energy of 4.75 keV is the atomic photo effect. In this process all the photon energy is transferred to the resulting photo electron.

scattering and Thomson scattering was applied to characterize the microscopic structure of shock-compressed graphite. The photon energy of the probe radiation was 4.75 keV which has an $1/e$ absorption length of 204.3 μm in graphite (see figure 4.1 and [Henke et al., 1993]). Therefore, samples of comparable and smaller thicknesses were used and multiple scattering events can be neglected because the dominant absorption process is the atomic photo effect.

The theory which is necessary to interpret the collected scattering spectra is presented in this chapter. First a simple treatment for Thomson scattering from a single free electron is discussed which is then generalized to X-ray scattering from matter (especially warm dense matter). Finally, the applied method to characterize phase transitions in WDM by using the measurement of different scattering features and the comparison of their relative intensity is described.

4.1 X-ray Thomson scattering from a single free electron

Thomson scattering, in general, is the scattering of electromagnetic radiation from electrons where the energy transferred to the electron in the scattering process is much smaller than the rest mass of the electron $m_e c^2$. There is a sufficient purely classical treatment of the interaction which may be thought of as follows [Hutchinson, 2005]: An incident electromagnetic wave impinges on the electron. As a result of the electric and magnetic fields of the wave, the particle is accelerated. The electron undergoing acceleration emits electromagnetic dipole radiation. This emitted radiation is the scattered wave. To describe this elementary process the electric field of the incident radiation is considered to be a plane monochromatic wave:

$$\vec{E}_i(\vec{r}, t) = \vec{E}_{i,0} e^{i(\vec{k}_i \vec{r} - \omega_i t)}. \quad (4.1)$$

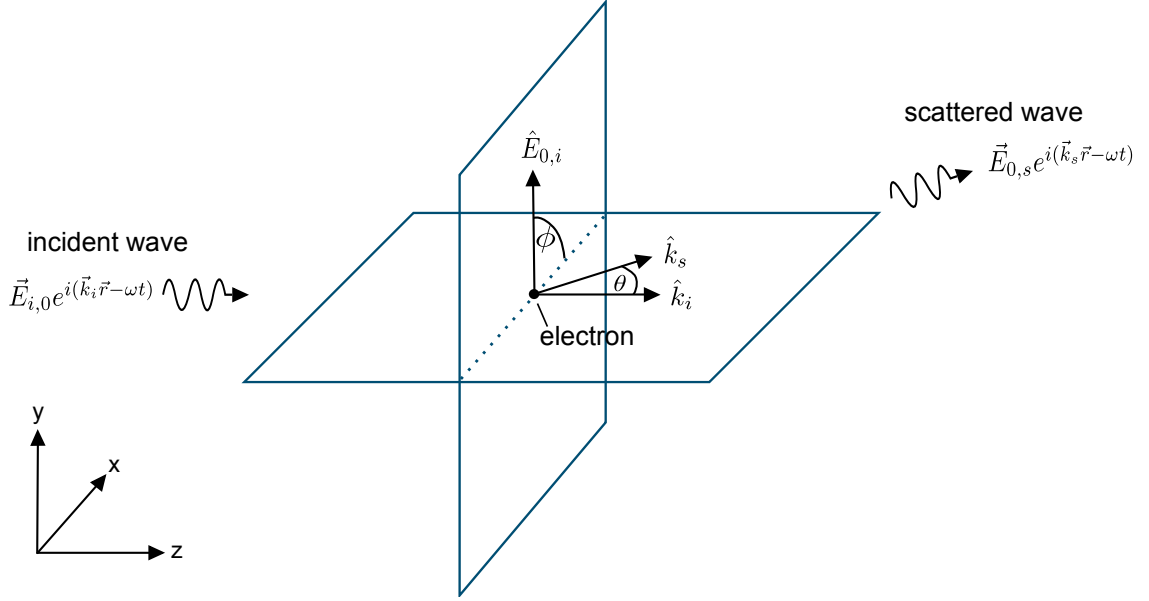


Figure 4.2: Definition of the scattering geometry: \hat{k}_i , \hat{k}_s and $\hat{E}_{0,i}$ are the corresponding unit vectors to \vec{k}_i , \vec{k}_s and $\vec{E}_{0,i}$, respectively. θ is the scattering angle and ϕ the polarization angle between $\vec{E}_{0,i}$ and the scattering plane defined by \vec{k}_i and \vec{k}_s .

Here, $\vec{E}_{i,0}$ is the amplitude, \vec{k}_i the wave vector and ω_i the frequency of the incident wave $\vec{E}_i(\vec{r}, t)$. With \vec{k}_s denoting the wave vector and ω_s the frequency of the scattered field, respectively, the momentum transfer within the scattering process is $\hbar(\vec{k}_s - \vec{k}_i) \equiv \hbar\vec{k}$. Hereby, \vec{k} is called the scattering vector and its absolute value is, applying the restrictions for Thomson scattering (i.e. $|\vec{k}_s| \approx |\vec{k}_i|$), in good approximation:

$$k \equiv |\vec{k}| = \frac{2\omega_i}{c} \sin(\theta/2), \quad (4.2)$$

where θ is the scattering angle, as defined in figure 4.2. The corresponding energy transfer within the scattering process is $\hbar(\omega_i - \omega_s) \equiv \hbar\omega$. For the following calculations it is convenient to introduce unit vectors along the directions of \vec{k}_i , \vec{k}_s and $\vec{E}_{0,i}$ using the coordinate system defined in figure 4.2:

$$\hat{k}_i = \begin{pmatrix} 0 \\ 0 \\ 1 \end{pmatrix}; \quad \hat{k}_s = \begin{pmatrix} \sin \theta \\ 0 \\ \cos \theta \end{pmatrix}; \quad \hat{E}_{0,i} = \begin{pmatrix} \cos \phi \\ \sin \phi \\ 0 \end{pmatrix}.$$

With these definitions, the scattered electric field $\vec{E}_s(\vec{r}, t)$ caused by an accelerated electron at a distance R , moving with velocity \vec{v} and presuming non-relativistic motion ($|\vec{v}| \ll c$), can be written as [Jackson, 1999]:

$$\vec{E}_s(\vec{r}, t) = -\frac{e}{4\pi\epsilon_0 c^2 R} \left[\hat{k}_s \times \left(\hat{k}_s \times \dot{\vec{v}}(\vec{r}, t) \right) \right]. \quad (4.3)$$

Here, e is the elementary charge and ϵ_0 the dielectric constant. The acceleration of the electron is connected to the electric field of the incident photon by the equation of motion:

$$\dot{\vec{v}}(\vec{r}, t) = -\frac{e}{m_e} \vec{E}_i(\vec{r}, t). \quad (4.4)$$

This expression can be inserted into equation (4.3) and the time averaged scattered radiation power $d\bar{P}_s$ to a solid angle element $d\Omega = dA/R^2$ can be formulated as:

$$\begin{aligned}\frac{d\bar{P}_s}{d\Omega} &= R^2 \frac{d\bar{P}_s}{dA} = \frac{R^2 \epsilon_0 c}{2} \lim_{T \rightarrow \infty} \frac{1}{T} \int_{-T/2}^{T/2} dt |\vec{E}_s(\vec{r}, t)|^2 \\ &= \frac{\epsilon_0}{m_e^2 c^3} \left(\frac{e^2}{4\pi\epsilon_0} \right)^2 \left| \hat{k}_s \times (\hat{k}_s \times \vec{E}_{0,i}) \right|^2.\end{aligned}\quad (4.5)$$

After applying the definition of the unit vectors in the chosen coordinate system, the scattered power for linearly polarized incident radiation with polarization angle ϕ (as defined in figure 4.2) is:

$$\frac{d\bar{P}_s}{d\Omega} = \frac{\epsilon_0}{2m_e^2 c^3} \left(\frac{e^2}{4\pi\epsilon_0} \right)^2 |\vec{E}_{0,i}|^2 (1 - \cos^2 \phi \sin^2 \theta). \quad (4.6)$$

For unpolarized light, using $\overline{\cos^2 \phi} = \frac{1}{2}$ and the incident intensity $I_i = \frac{1}{2} \epsilon_0 c |\vec{E}_{0,i}|^2$, the time-averaged scattered power per solid angle is then simply given by:

$$\frac{d\bar{P}_s}{d\Omega} = \left(\frac{e^2}{4\pi\epsilon_0 m_e c^2} \right)^2 \frac{1}{2} (1 + \cos^2 \theta) I_i = \frac{r_0^2 I_i}{2} (1 + \cos^2 \theta), \quad (4.7)$$

where $r_0 = e^2/(4\pi\epsilon_0 m_e c^2) = 2.818 \times 10^{-15}$ m is the classical electron radius. Obviously, r_0^2 is a very small quantity and therefore, large photon numbers and sensitive detectors are needed to realize successful scattering experiments.

4.2 X-ray scattering from matter

In a realistic scenario of a scattering experiment, a finite volume of matter has to be considered. This means there is a time-dependent electron distribution function, which is, especially in the warm dense matter regime, strongly connected to the atoms (or ions). This results in effects of the electronic structure within the atoms (ions) and the sample volume in general. Basically, these effects can be the consequence of collective or non-collective behavior of the electrons: Photon energy, scattering angle and sample parameters like temperature and density decide whether the collective or non-collective scattering regime can be accessed in an experiment. Usually, the parameter

$$\alpha = \frac{1}{k\lambda_s} \quad (4.8)$$

is used to define whether the motion of single electrons can be resolved within the scattering process. Here, λ_s is the screening length of the interaction potential of the electrons. In plasma physics λ_s is closely connected to the electron Debye length $\lambda_{D,e}$ and for many applications it is sufficient to use $\lambda_s = \lambda_{D,e}$. For $\alpha > 1$, the motion of single electrons is invisible for the scattering process and collective effects become important whereas $\alpha < 1$ defines the non-collective scattering regime [Glenzer and Redmer, 2009].

To describe the scattering process from matter, a scenario, as pictured in figure 4.3, is considered. The contribution of the scattered electric field from one electron to the total signal at the detector is given by the motion of an accelerated electron at the retarded time t' [Sheffield, 1975]:

$$t' = t - \frac{|\vec{R} - \vec{r}_j(t)|}{c} = t - \frac{R}{c} + \frac{\hat{k}_s \vec{r}_j(t')}{c}. \quad (4.9)$$

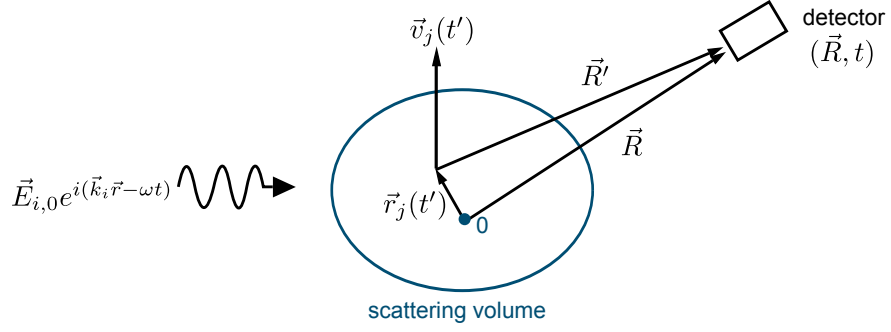


Figure 4.3: Realistic scattering scenario: The scattered signal recorded by the detector at a time t is the consequence of the acceleration of an electron at the retarded time t' within a finite scattering sample volume. For calculation purposes it is assumed that the detector is far away from the scattering volume, giving $|\vec{R}| \approx |\vec{R}'|$.

Here, the approximation $|\vec{R}| \gg |\vec{r}_j|$ has been applied (compare figure 4.3). Considering a scattering experiment, there is usually a spectrally resolved detector which measures radiation at a frequency ω_s and has an acceptance interval $[-d\omega_s/2, d\omega_s/2]$. A frequency-dependent expression of the scattered electric field can be obtained by Fourier transformation:

$$\tilde{E}_s(R, \omega_s) = \int_{-\infty}^{+\infty} dt \tilde{E}_s(R, t) e^{-i\omega_s t}. \quad (4.10)$$

The tilde underlines that $\tilde{E}_s(R, \omega_s)$ and $\tilde{E}_s(R, t)$ have different units. Applying the principle of the retarded time to the Fourier transform, the scattered field of one electron is then given by

$$\begin{aligned} \tilde{E}_{j,s}(R, \omega_s) &= \frac{r_0}{R} \left[\hat{k}_s \times \left(\hat{k}_s \times \vec{E}_{0,i} \right) \right] \int_{-\infty}^{+\infty} dt' e^{i \left[\omega_s \left(t' + \frac{R}{c} - \frac{\hat{k}_s \vec{r}_j}{c} \right) \right]} e^{i[\vec{k}_i \vec{r}_j(t') - \omega_i t']} \\ &= \frac{r_0}{R} e^{i\vec{k}_s \vec{R}} \left[\hat{k}_s \times \left(\hat{k}_s \times \vec{E}_{0,i} \right) \right] \int_{-\infty}^{+\infty} dt' e^{-i[\omega t' + \vec{k} \vec{r}_j(t')]} \end{aligned} \quad (4.11)$$

Hereby, equation (4.3) and the substitutions $\omega = \omega_i - \omega_s$, $\vec{k} = \vec{k}_s - \vec{k}_i$ as well as $|\vec{k}| = \omega/c$ have been used. To calculate the total scattered field \tilde{E}_s^T , the time-dependent distribution function of the electrons $f_e(\vec{r}, \vec{v}, t')$ has to be considered:

$$f_e(\vec{r}, \vec{v}, t') = \sum_j \delta(\vec{r} - \vec{r}_j(t')) \delta(\vec{v} - \vec{v}_j(t')), \quad (4.12)$$

where $\delta(x)$ is the Dirac delta-function. With this expression the total scattered field of all electrons in the scattering volume is given by:

$$\begin{aligned} \tilde{E}_s^T(R, \omega_s) &= \int d^3r \int d^3v \int dt' \tilde{E}_s(\vec{r}, t) f_e(\vec{r}, \vec{v}, t') e^{i \left[\omega_s \left(t' + \frac{R}{c} - \frac{\hat{k}_s \vec{r}_j}{c} \right) \right]} \\ &= \frac{r_0}{R} e^{i\vec{k}_s \vec{R}} \left[\hat{k}_s \times \left(\hat{k}_s \times \vec{E}_{0,i} \right) \right] \int d^3r \int d^3v \int dt' e^{-i[\omega t' + \vec{k} \vec{r}(t')]} f_e(\vec{r}, \vec{v}, t'). \end{aligned} \quad (4.13)$$

In the non-relativistic case the electric field is independent from the velocity \vec{v} . Therefore the \vec{v} -integration of the distribution function simply yields the electron density $n_e(\vec{r}, t')$. For the further calculation the electron density has to be expressed as Fourier integral:

$$n_e(\vec{r}, t') = \int \frac{d^3k'}{(2\pi)^3} \int \frac{d\omega'}{2\pi} \tilde{n}_e(\vec{k}', \omega') e^{i(\vec{k}' \vec{r} + \omega' t')}. \quad (4.14)$$

Here, $\tilde{n}_e(\vec{k}', \omega')$ is the Fourier transformation of the electron density in space and time. Again, the tilde underlines the different units of $\tilde{n}_e(\vec{k}', \omega')$ and $n_e(\vec{r}, t')$. Substituting the electron density in equation (4.13) and using $\int dy e^{i(x-x_0)y} = 2\pi\delta(x-x_0)$ and the three-dimensional analogon of this identity, the expression of the total scattered electric field can be simplified [Wünsch, 2011]:

$$\tilde{E}_s^T(R, \omega_s) = \frac{r_0}{R} e^{i\vec{k}_s \vec{R}} \left[\hat{k}_s \times (\hat{k}_s \times \vec{E}_{0,i}) \right] \tilde{n}_e(\vec{k}, \omega). \quad (4.15)$$

Using Parseval's theorem [Sheffield, 1975] the time averaged scattered power $d\bar{P}_s$ to a solid angle element $d\Omega$ can be expressed in terms of $\tilde{E}_s^T(R, \omega_s)$:

$$\begin{aligned} \frac{d\bar{P}_s}{d\Omega} &= \frac{R^2 \epsilon_0 c}{2} \lim_{T \rightarrow \infty} \frac{1}{T} \int_{-T/2}^{T/2} dt |\tilde{E}_s^T(R, t)|^2 \\ &= \frac{R^2 \epsilon_0 c}{2} \lim_{T \rightarrow \infty} \frac{1}{\pi T} \int_{\omega_s - d\omega_s/2}^{\omega_s + d\omega_s/2} d\omega_s |\tilde{E}_s^T(R, \omega)|^2 \end{aligned} \quad (4.16)$$

For an ensemble of N atoms (or ions) with nuclear charge Z , unpolarized light and using equation (4.15), this can be simplified to

$$\frac{d^2\bar{P}}{d\Omega d\omega_s} = I_i r_0^2 \frac{1}{2} (1 + \cos^2 \theta) N S(\vec{k}, \omega), \quad (4.17)$$

where

$$S(\vec{k}, \omega) = \lim_{T \rightarrow \infty} \frac{1}{2\pi N T} \langle |\tilde{n}_e(\vec{k}, \omega)|^2 \rangle \quad (4.18)$$

is the dynamic structure factor of the electrons which contains all the information of the microscopic system. The angle brackets $\langle X \rangle$ mark the ensemble average of the quantity X .

Dealing with free electrons only and assuming the non-collective scattering regime ($\alpha \ll 1$), the static structure factor $S(\vec{k}) = \int d\omega S(\vec{k}, \omega)$ can easily be calculated. For a single free electron, the density in Fourier space is $\tilde{n}_e(\vec{k}, \omega) = 2\pi\delta(\omega - \vec{k} \vec{v})$. Using $\delta^2(\omega) = \lim_{T \rightarrow \infty} \frac{T}{2\pi} \delta(\omega)$ [Hutchinson, 2005], the static structure factor is then simply one. In this case equation (4.17) represents exactly equation (4.7) for the single free electron. Considering a fully ionized plasma with an electron velocity distribution function f_v , the dynamic structure factor is directly proportional to this distribution: $S(\vec{k}, \omega) = \frac{1}{k} f_v(\frac{\omega}{k})$. Because the velocity distribution is normalized, the static structure factor $S(\vec{k})$ is simply the number of free electrons per atom, Z , for this case.

The definition of the structure factor in equation (4.18) is very practical to derive the connection between the scattered radiation power and electronic structure from the forced dipole radiation model. Concerning warm dense matter, however, atomic or ionic structure as well as free and bound electrons have to be considered which result in different scattering features. To connect these processes with the scattered radiation, another definition, which can be found in related literature and is totally equivalent to equation (4.18), is more often used in X-ray Thomson scattering publications [Chihara, 2000; Gregori et al., 2003]:

$$S(\vec{k}, \omega) = \frac{1}{2\pi N} \int dt' \langle \tilde{n}_e(\vec{k}, t) \tilde{n}_e^*(\vec{k}, t + t') \rangle e^{i\omega t'}. \quad (4.19)$$

Here, $\tilde{n}_e(\vec{k}, t)$ is the Fourier transform of the electron density $n_e(\vec{r}, t)$ in space. Assuming the general case of a partially ionized plasma consisting of N atoms (ions), Z_b bound electrons per atom and Z_f free electrons per atom, the electron density in Fourier space is given by:

$$\tilde{n}_e(\vec{k}, t) = \sum_{l=1}^N \sum_{j=1}^{Z_b} e^{i\vec{k}[\vec{r}_{jl}(t) + \vec{R}_l(t)]} + \sum_{m=1}^{NZ_f} e^{i\vec{k}\vec{r}_m(t)}, \quad (4.20)$$

where $\vec{R}_l(t)$ is the position of the l -th ion, $\vec{R}_l(t) + \vec{r}_{jl}(t)$ the position of the j -th bound electron in the l -th ion and $\vec{r}_m(t)$ the position of the m -th free electron. With this definition the dynamic structure factor can be decomposed to the sum of three terms, corresponding to elastic scattering from bound electrons (Rayleigh scattering), inelastic scattering from free electrons (Thomson scattering) and inelastic scattering from bound electrons (Thomson and Raman scattering, depending on the binding energy of the electrons compared to $\hbar\omega$) [Chihara, 2000]:

$$S(\vec{k}, \omega) = \underbrace{|f(\vec{k}) + q(\vec{k})|^2 S_{ii}(\vec{k}, \omega)}_{\text{elastic scattering}} + \underbrace{Z_f S_{ee}^0(\vec{k}, \omega)}_{\text{scattering from free electrons}} + \underbrace{Z_b \int \tilde{S}_{be}(\vec{k}, \omega - \omega') S_s(\vec{k}, \omega') d\omega'}_{\text{inelastic scattering from bound electrons}}. \quad (4.21)$$

Hereby, the following definitions have been applied:

$$\begin{aligned} f(\vec{k}) &= \left\langle \sum_{j=1}^{Z_b} e^{i\vec{k}\vec{r}_{jl}(t)} \right\rangle \\ q(\vec{k}) &= \frac{1}{2\pi N} \frac{\sqrt{Z_f}}{S_{ii}(\vec{k}, \omega)} \int dt' \left\langle \sum_l^N \sum_m^{Z_f} e^{i\vec{k}[\vec{R}_l(t') - \vec{r}_m(t+t')]} \right\rangle e^{i\omega t'} \\ S_{ii}(\vec{k}, \omega) &= \frac{1}{2\pi N} \int dt' \left\langle \sum_{l,m}^N e^{i\vec{k}[\vec{R}(t')_l - \vec{R}_m(t+t')]} \right\rangle e^{i\omega t'} \\ S_{ee}^0(\vec{k}, \omega) &= \frac{1}{2\pi N} \int dt' \left\langle \sum_{m,l}^{NZ_f} e^{i\vec{k}[\vec{r}_l(t') - \vec{r}_m(t+t')]} \right\rangle e^{i\omega t'} - \frac{|q(\vec{k})|^2}{Z_f} S_{ii}(\vec{k}, \omega) \\ S_s(\vec{k}, \omega) &= \frac{1}{2\pi N} \int dt' \left\langle e^{i\vec{k}[\vec{R}_l(t') - \vec{R}_l(t+t')]} \right\rangle e^{i\omega t'} \\ \tilde{S}_{be}(\vec{k}, \omega) &= \frac{1}{2\pi N} \int dt' \left(\left\langle \sum_{l,m=1}^{NZ_b} e^{i\vec{k}[\vec{r}_{al}(t') - \vec{r}_{am}(t+t')]} \right\rangle - |f(\vec{k})|^2 \right) e^{i\omega t'} \end{aligned}$$

Evidently, these quantities have special physical meanings which are listed in the following tabular:

$f(\vec{k})$	atomic form factor
$q(\vec{k})$	screening of the ions because of free electrons
$S_{ii}(\vec{k}, \omega)$	ionic structure factor
$S_{ee}^0(\vec{k}, \omega)$	free electron structure factor
$S_s(\vec{k}, \omega)$	self-motion of the ions
$\tilde{S}_{be}(\vec{k}, \omega)$	inelastic structure factor of bound electrons

For an isotropic system, all these functions, and therefore also the total dynamic structure factor, are only dependent on the absolute value of the scattering vector $|\vec{k}| \equiv k$. Thus, the term $S(k, \omega)$ will be used for convenience in the following.

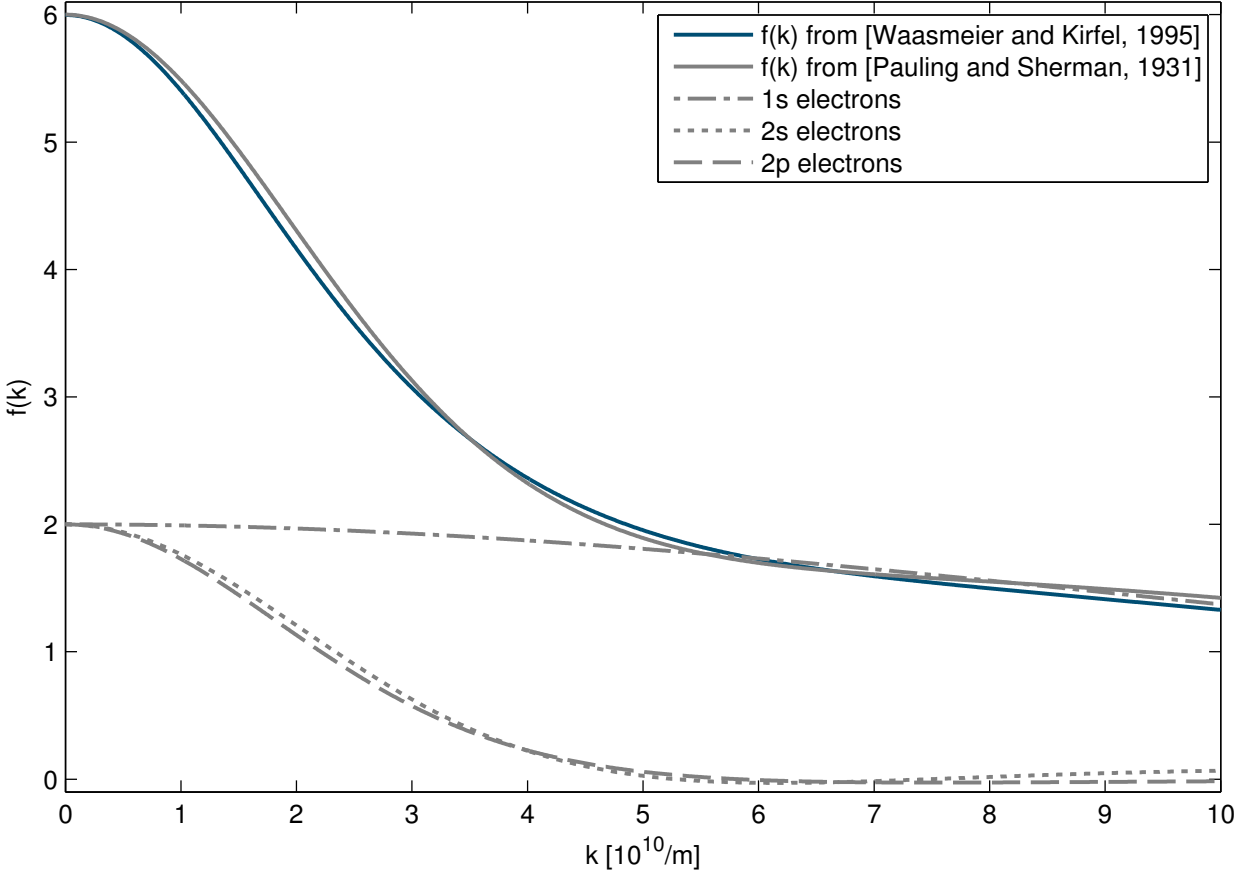


Figure 4.4: The atomic form factor of carbon from [Waasmaier and Kirfel, 1995] and [Pauling and Sherman, 1931]. The contributions of the different electron levels are also shown. These are important for the bound-free scattering (see section 4.2.3).

4.2.1 Elastic scattering

In the elastic scattering scenario, the recoil of the electron is directly transferred to the atom (or ion). Because those are much heavier than electrons, there is nearly no energy transfer in the scattering process for X-ray energies applied in typical warm dense matter experiments. That is the origin of the term "elastic scattering", as resolving the motion of the atoms (ions) in an experiment of X-ray scattering from a warm dense matter sample is usually not possible. Therefore, a sufficient approximation for the dynamic structure factor for elastic scattering is:

$$|f(k) + q(k)|^2 S_{ii}(k, \omega) = |f(k) + q(k)|^2 S_{ii}(k) \delta(\omega), \quad (4.22)$$

where $S_{ii}(k)$ is the static ion-ion structure factor. The consequence of the delta function is that the energy spectrum of the probe radiation is not shifted and broadened by the scattering process. Thus, the spectral shape of the probe radiation is totally conserved. The static ion-ion structure $S_{ii}(k)$ can directly be obtained via Fourier transform of the pair correlation function $g(\vec{r})$ (compare section 2.2):

$$S_{ii}(k) = 1 + \frac{N}{V} \int d^3r g(\vec{r}) e^{-i\vec{k}\vec{r}}. \quad (4.23)$$

Separating the coherent contribution at $\vec{k} = 0$ from the integral, this expression of the ion-ion structure gives

$$S_{ii}(k) = 1 + \frac{N}{V} \delta(\vec{k}) + \frac{N}{V} \int d^3r [g(\vec{r}) - 1] e^{-i\vec{k}\vec{r}} \quad (4.24)$$

For simplification, the delta function can be neglected for X-ray scattering applications, since only finite k -values are relevant in this case.

The atomic form factors $f(k)$ are usually obtained by numerical fits of experimental data [Waasmaier and Kirfel, 1995]. Another approach is the use of screened hydrogenic wave functions which also give the contributions of the different electron levels in an atom [Pauling and Sherman, 1931]. In this model, the atomic form factors of the K- and L-shell electrons are given by analytical functions [Pauling and Sherman, 1931]:

$$f_{1,0}(k) = \frac{1}{\left[1 + \left(\frac{ka_B}{2Z_{1,0}}\right)^2\right]^2} \quad (4.25)$$

$$f_{2,0}(k) = \frac{1 - \left(\frac{ka_B}{2Z_{2,0}}\right)^2}{\left[1 + \left(\frac{ka_B}{2Z_{2,0}}\right)^2\right]^4} \quad (4.26)$$

$$f_{2,1}(k) = \frac{\left[1 - 2\left(\frac{ka_B}{2Z_{2,1}}\right)^2\right] \left[1 - \left(\frac{ka_B}{2Z_{2,1}}\right)^2\right]}{\left[1 + \left(\frac{ka_B}{2Z_{2,1}}\right)^2\right]^4}. \quad (4.27)$$

Here, $Z_{n,l} = Z - z_{n,l}$ is the effective nuclear charge seen by the electron in the quantum state n, l . In addition to the quantum numbers, the screening constants $z_{n,l}$ are also dependent on the total number of bound electrons in the atom (ion). For example ionized carbon has smaller screening constants than atomic carbon. Tables containing atomic and ionic screening constants for various elements can be found in [Pauling and Sherman, 1931]. For atomic carbon, the effective nuclear charges are: $Z_{1,0}=5.81$, $Z_{2,0}=3.96$ and $Z_{2,1}=3.09$. The total form factor of the atom (ion) is given by the sum of all contributions of the single electrons:

$$f(k) = \sum_{n,l} f_{n,l}(k) \quad (4.28)$$

For low- Z elements, the analytical hydrogen-like model resembles the experimental data fits of the atomic form factor reasonably well (see figure 4.4).

Free electrons, which screen the Coulomb potential of the ions and follow the ion motion can give an additional contribution to the elastic scattering [Chihara, 1987]. The calculation of $q(k)$ for a warm dense matter state is rather complicated as the electron-ion potential has to be known [Gericke et al., 2010]. However, for the scattering angles implemented in the experiments in the framework of this thesis, $q(k)$ is expected to be close to zero [Wünsch, 2011] and thus, can be neglected.

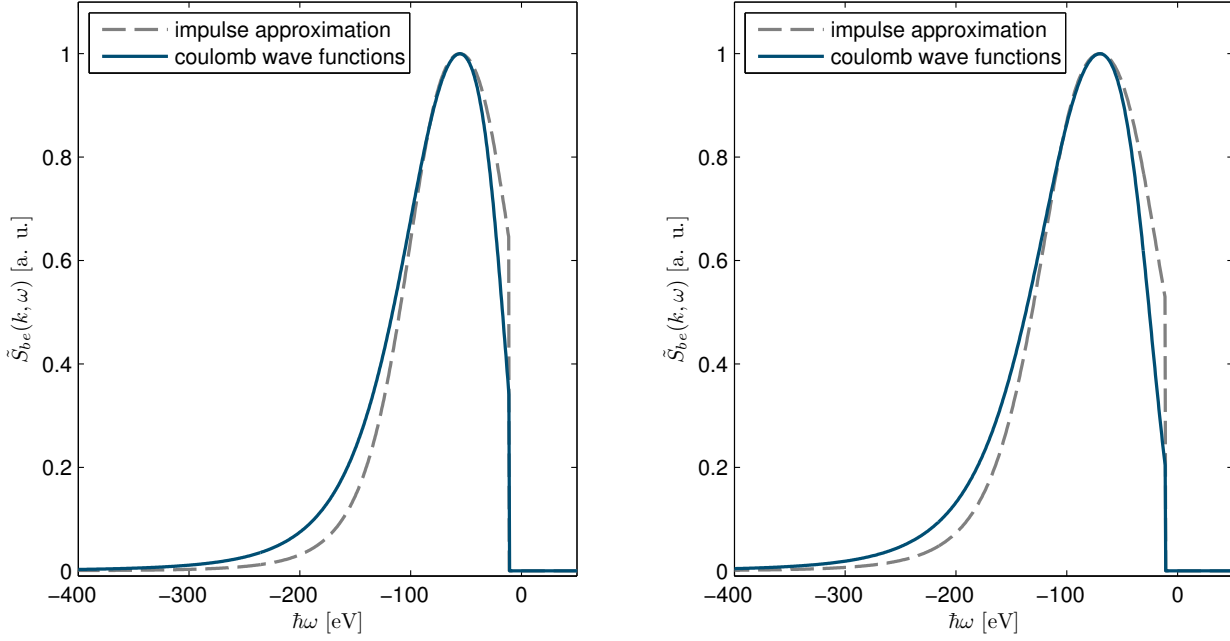


Figure 4.5: Bound-free dynamic structure factor $\tilde{S}_{be}(k, \omega)$ profiles of carbon for a photon energy of 4750 eV and 126° scattering angle. The cut-off at small energy shifts is due to the binding energies of the L-shell electrons. The contribution of the tightly bound K-shell electrons can be neglected.

4.2.2 Inelastic scattering from free electrons

Inelastic scattering from free electrons is a popular tool for the measurement of basic plasma parameters. In the collective scattering regime the electron density can be obtained [Glenzer et al., 2007] and, as shown before, non-collective scattering spectra directly represent the electron velocity distribution which gives the electron temperature. The corresponding structure factor $S_{ee}^0(k, \omega)$ can be formally derived from the fluctuation-dissipation theorem [Kubo, 1957; Glenzer and Redmer, 2009; Gregori et al., 2003, 2007]. However, the presence of free electrons in the shock-compressed carbon state, which was reached in the experiments presented in this thesis, is relatively unlikely (see chapter seven). Additionally, if there were free electrons, the inelastic scattering features would not change enough to detect a sufficient difference compared to inelastic scattering from bound electrons (see next section) because of the relatively low temperatures. Therefore, the discussion of the inelastic free electron scattering feature is not necessary for the data analysis in the context of this thesis.

4.2.3 Inelastic scattering from bound electrons

Considering bound electrons, there are two processes of inelastic scattering: Raman scattering where the electron is transferred to an excited bound state or, if the energy transfer to the energy is larger than the ionization potential, bound-free scattering, where the electron is transferred to the continuum. The contribution of Raman scattering to the recorded spectra in X-ray scattering experiments for the characterization of warm dense matter is typically negligible [Gregori et al., 2003, 2004]. Therefore, Raman scattering will be ignored in the following. Bound-free scattering, however, usually gives a strong contribution in X-ray scattering experiments using elements with populated L-shell and a non-collective scattering geometry.

For weakly bound electrons, which means $|E_b/E_C|^2 \ll 1$, where E_b is the binding energy of the electron and $E_C = \hbar^2 k^2 / (2m_e)$ the Compton energy, the "impulse approximation" [Eisenberger and Platzman, 1970] is a common treatment of bound-free scattering [Gregori et al., 2004]. In this approximation it is assumed that the electron-photon interaction occurs on a very short time scale, so the nuclear potential seen by the electron does not change during the scattering process. Therefore the electrons can be treated as free and the Doppler broadening of the scattered radiation is defined by the initial velocity distribution of the electrons within the atom or ion. Using hydrogenic wave functions for the distribution of bound electrons, the profiles of the impulse approximation for K- and L-shell electrons have the following form [Bloch and Mendelsohn, 1975]:

$$J_{1,0}(k, \omega) = \frac{8}{3\pi Z_{1,0}(1 + \xi^2/Z_{1,0}^2)^3} \quad (4.29)$$

$$J_{2,0}(k, \omega) = \frac{64}{9\pi Z_{2,0}} \left[\frac{1}{3(1 + 4\xi^2/Z_{2,0}^2)^3} - \frac{1}{(1 + 4\xi^2/Z_{2,0}^2)^4} + \frac{4}{5(1 + 4\xi^2/Z_{2,0}^2)^5} \right] \quad (4.30)$$

$$J_{2,1}(k, \omega) = \frac{64}{15\pi Z_{2,1}} \frac{1 + 20\xi^2/Z_{2,1}^2}{(1 + 4\xi^2/Z_{2,1}^2)^5}, \quad (4.31)$$

where

$$\xi = \frac{m_e a_B}{\hbar k} \left(\omega - \frac{\hbar k^2}{2m_e} \right). \quad (4.32)$$

As mentioned above, this is only correct to the order of $|E_b/E_C|^2$. Since the Compton energy of the experiments presented in this thesis is 50 to 60 eV and the binding energy of carbon L-shell electrons is ~ 11 eV, it is useful to include higher order corrections. The impulse approximation assumes plane waves for the final state of the electrons. An improvement can be obtained by using Coulomb wave functions for the final states, as done by [Schumacher et al., 1975]. This results in an asymmetric correction of the bound-free profile which has been verified experimentally [Holm and Ribberfors, 1989]. The contribution of one bound electron to the dynamic bound-free structure factor is then given by

$$J_{n,l}(k, \omega) = \frac{2^{4(l+1)} n^2 (n-l-1)! (l!)^2 m_e \sqrt{1+p^2}}{2\pi^2 (n+l)! \alpha_f \hbar Z_{n,l}} [\Phi_{n,l}(1 + \eta_-^2) - \Phi_{n,l}(1 + \eta_+^2)] \quad (4.33)$$

where α_f is the fine structure constant and the definitions

$$p = \sqrt{\left(\frac{\hbar \omega}{m_e c^2} - 1 \right)^2 - 1}, \quad (4.34)$$

$$\eta_- = \frac{n \left(p - \frac{\hbar k}{m_e c} \right)}{\alpha_f Z_{n,l}}, \quad \eta_+ = \frac{n \left(p + \frac{\hbar k}{m_e c} \right)}{\alpha_f Z_{n,l}} \quad (4.35)$$

have been used. The shell functions Φ_{nl} can be found in [Schumacher et al., 1975] and have the following expressions for K- and L-shell electrons:

$$\Phi_{1,0}(x) = \frac{1}{x^3} \quad (4.36)$$

$$\Phi_{2,0}(x) = 4 \left(\frac{1}{3x^3} - \frac{1}{x^4} + \frac{4}{5x^5} \right) \quad (4.37)$$

$$\Phi_{2,1}(x) = \frac{1}{4x^4} - \frac{1}{5x^5} \quad (4.38)$$

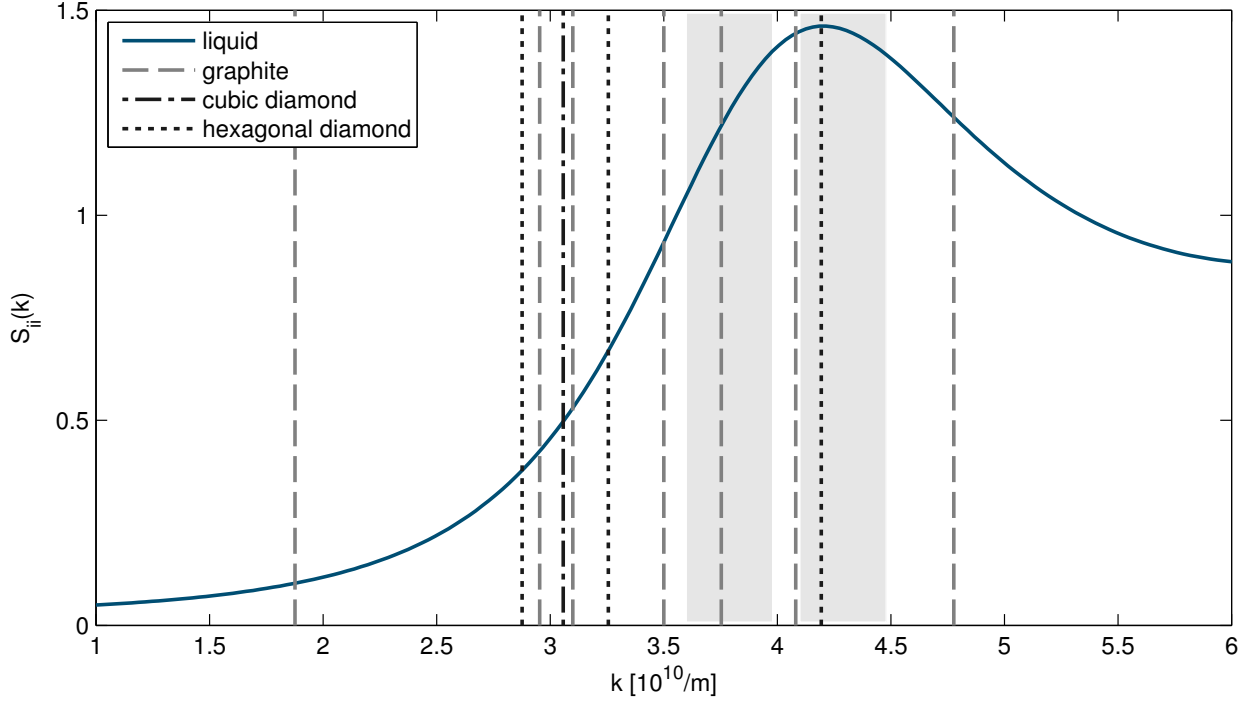


Figure 4.6: Diagram of the expected ion-ion structure factor for liquid carbon with a density of 4 g/cm^3 , compared to the relevant crystal phases of carbon. The positions of the strongest Bragg maxima of graphite, cubic and hexagonal diamond are represented by vertical lines. The gray shaded area shows the region of k values covered by the scattering spectrometers in the experiment. The approximate structure factor of liquid carbon was calculated via the HNC approach (thanks to Kathrin Wünsch).

Calculating the total profiles, it has to be considered that bound-free transitions are only allowed if the energy transferred to the electron exceeds its binding energy. Thus, the total structure factor of the inelastic scattering by bound electrons [Gregori et al., 2004] (for both impulse approximation and Coulomb waves)

$$\tilde{S}_{be}(k, \omega) = \left[\sum_{n,l} (1 - f_{n,l}^2(k)) \right] \left[\sum_{n',l'} J_{n',l'}(k, \omega) \right] \quad (4.39)$$

has a cut-off at $\omega = E_b/\hbar$ and is zero for $|\omega| < E_b/\hbar$ (see figure 4.5). The factor in front of the sum of the spectral bound-free profiles accounts for the possibility of elastic scattering [James, 1962].

4.3 Measurement and characterization of phase transitions

The spectral intensity of scattered radiation can be very sensitive to phase transitions, as the static ion-ion structure factor $S_{ii}(k)$ directly reflects the atomic or ionic correlations of the sample material. Therefore, especially the elastic scattering can vary strongly for a solid-liquid phase transition, which was investigated in the framework of this thesis. The amount of variation is mainly dependent on the implemented experimental scattering geometry. For a cold crystal, like graphite, scattering is dominated by the elastic scattering if the conditions of Bragg reflection at a crystal plane are fulfilled by the experimental setup. If the scattering angle is chosen the way that no Bragg condition can be implemented, the scattering signal will be dominated by inelastic scattering from

weakly bound electrons. If the contributions of free electrons can be neglected, the static electron structure factor for this case is given by [James, 1962]:

$$S(k) = |f(k)|^2 S_{ii}(k) + \sum_{n=1}^{Z_{wb}} (1 - f_n^2(k)). \quad (4.40)$$

Hereby, Z_{wb} is the number of electrons which are weakly bound compared to the energy transferred within the scattering process ($E_b < \hbar\omega$). Sometimes the contribution of the bound electrons is simplified by assuming that every bound electron gives approximately the same contribution to the atomic (or ionic) form factor [Gregori et al., 2004; Pelka et al., 2010]:

$$\sum_{n=1}^{Z_{wb}} (1 - f_n^2(k)) \approx Z_{wb} \left[1 - \left(\frac{f(k)}{Z} \right)^2 \right]. \quad (4.41)$$

This approximation, however, is not true for the k -values applied in the experiments presented in this thesis (compare for example figure 4.4). Due to the fact that not all electrons contribute to the bound-free term, this approximation gives roughly a deviation of 10 % for the applied photon energy and scattering angles.

During the solid-liquid phase transition, the structure factor $S_{ii}(k)$ changes dramatically from a function with narrow spikes at the position of the Bragg peaks to a more continuous function in the liquid (see figure 4.6). Because the contribution of the weakly bound electrons can be estimated to be nearly equal for solid and liquid, X-ray scattering is able to monitor the phase transition if the chosen scattering angle results in a large difference of $S_{ii}(k)$ for the two phases. Besides monitoring, X-ray scattering is also able to characterize phase transitions: If the ratio of elastic scattering to inelastic scattering x_{el}/x_{inel} can be resolved in a scattering experiment, an absolute value of $S_{ii}(k)$ can be measured by using equation (4.40):

$$S_{ii}(k) = \frac{1}{|f(k)|^2} \left[\sum_{n=1}^{Z_{wb}} (1 - f_n^2(k)) \right] \frac{x_{el}}{x_{inel}}. \quad (4.42)$$

This can be realized, for example, by implementing large scattering angles which result in sufficient frequency shifts of the inelastic scattering that elastic and inelastic scattering can be distinguished on the detector. Additionally, the energy spread of the probe radiation has to be as low as possible to separate the two features. This directly leads to the experimental part of thesis where this method has been realized for the solid-liquid phase transition of shock-compressed graphite.



5 Experimental methods

In the framework of this thesis two experimental campaigns at the target area Z6 of the *GSI Helmholtzzentrum für Schwerionenforschung* were planned, prepared and performed. Both experiments on the characterization of laser-driven shocks and the use of X-ray scattering as diagnostic tool for warm dense matter have never been realized before at GSI. Therefore, the first campaign was planned to be a test run for optimizing the achievable pressures in the laser-driven shocks and the generation of X-rays. Additionally, first X-ray scattering spectra were already obtained within this first run. Due to the analysis of these results, the experimental setup of the second campaign was modified for a more detailed structure analysis of the generated state of matter. The setup of both experimental campaigns, the applied laser systems, targets, instruments and detectors are briefly presented in this chapter.

5.1 Experimental setup at the target area Z6 at GSI

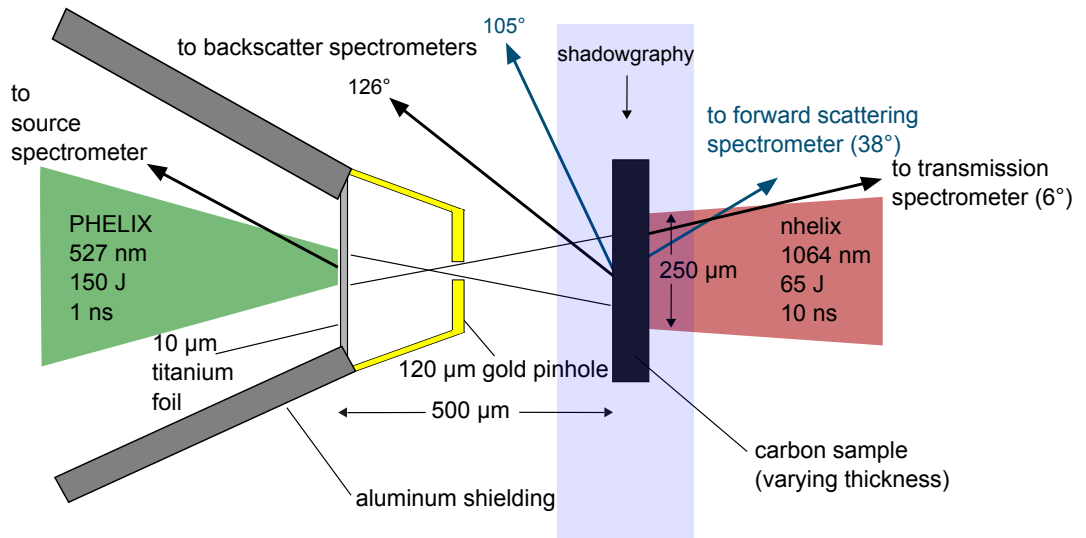


Figure 5.1: Principal experimental scheme for both experimental campaigns. The modifications of the second campaign are marked by **color**.

The general experimental scheme for both experimental campaigns was as follows (see figure 5.1): The *nhelix* laser system was used to launch shock waves into graphite samples of 100 µm to 200 µm thickness. The standard laser parameters of the *nhelix* system during the first campaign were ~ 65 J in 9 ns (FWHM) with a focal spot of ~ 250 µm in diameter, resulting in driving intensities of $\sim 1.5 \times 10^{13}$ W/cm². During the second campaign, the typical laser parameters of the *nhelix* system were only slightly different: ~ 60 J in 11 ns (FWHM) with a focal spot of ~ 200 µm in diameter, resulting in driving intensities of $\sim 1.7 \times 10^{13}$ W/cm². In both experimental campaigns, the long pulse option of the high energy laser system *PHELIX* (pulse energy 150 J, pulse length 1 ns, wavelength 527 nm) was focused onto a 10 µm thick titanium foil to a spot size of ~ 100 µm for the generation of the probe radiation X-rays. The resulting intensities of $\sim 10^{15}$ W/cm² were optimal to efficiently drive titanium helium- α radiation at 4.75 keV which was used as X-ray source in the experiment. The X-ray radiation was collimated by a gold pinhole in front of the titanium foil.

magnetic base plates
for focus cameras:
a nhelix

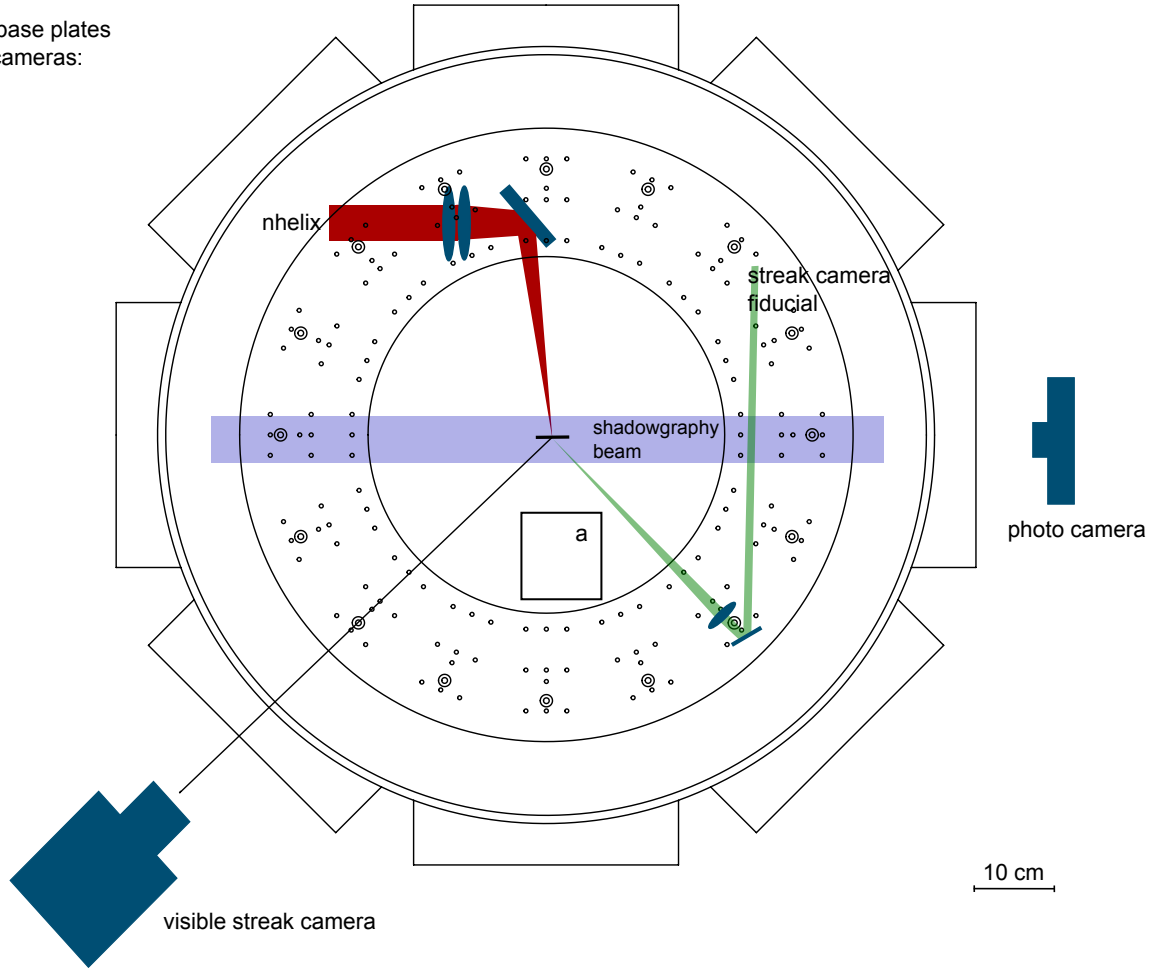


Figure 5.2: Schematic of the experimental setup in and around the target chamber at Z6 for the characterization of the shock waves by velocity measurements during the first experimental campaign.

For the target design, it was crucial to ensure the shielding of the scattering spectrometer from a direct line-of-sight to the X-ray source. Additionally, the scattering angles had to be well defined by the pinhole. This was realized with special micro-machining and galvanic techniques in the target laboratory of TU Darmstadt (see section 5.3.1).

The main X-ray diagnostics in the experiments were X-ray spectrometers consisting of flat or curved HOPG crystals as dispersive element and image plates as detectors (see sections 5.3.3 and 5.3.4). These spectrometers were monitoring the X-ray source radiation spectrum, the radiation which was transmitted through the graphite samples and the scattered radiation at scattering angles of 38° , 105° (both second campaign only) and 126° (first and second campaign). For the characterization of the thermodynamic state in the laser driven shock wave, the shock transit time through the graphite samples and the expansion velocity of the target rear side had to be determined. The shock transit time was measured by a visible streak camera which monitored the optical self-emission of the heated material at the moment of shock release (see section 5.2.3). The expansion velocity of the shock release at the target rear side was simultaneously imaged by a multi-frame shadowgraphy instrument (see section 5.2.2). Finally, a photo camera was mounted which generated time-integrated optical images of the interactions in all experiments.

Altogether, three different experimental setup schemes were realized during the experimental

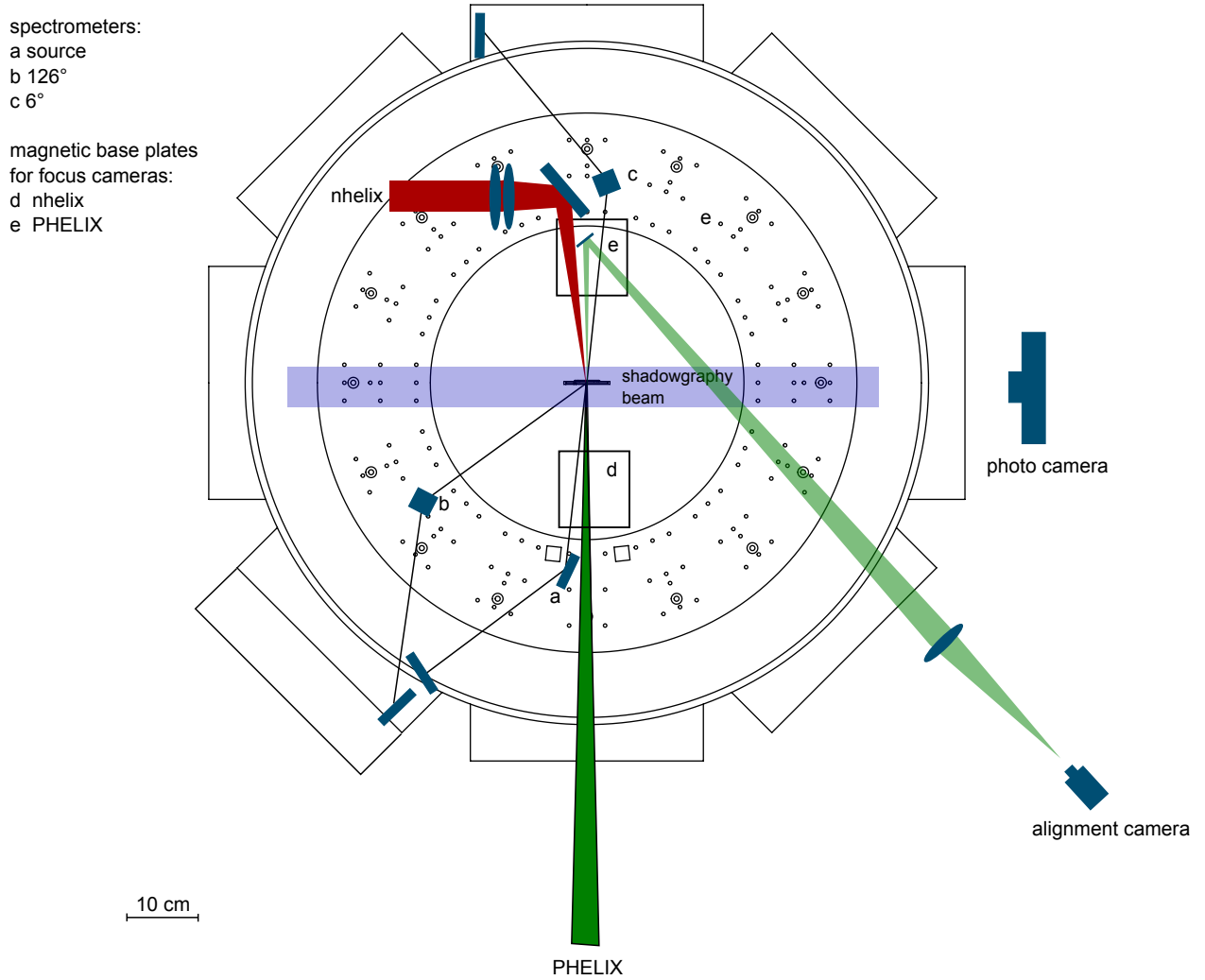


Figure 5.3: Schematic of the experimental setup in and around the target chamber at Z6 for the X-ray scattering measurements during the first experimental campaign.

campaigns. The design of the first setup of the first experimental campaign (see figure 5.2) was relatively simple because it was only for the characterization of the thermodynamic state in the laser-driven shock via the velocity measurements with visible streak camera and multi-frame shadowgraphy. As a relative time reference (a so-called fiducial), the light of a 500 ps laser pulse, which was diffusely reflected from the target mount, was simultaneously collected by the visible streak camera. However, for the second setup of the first experimental campaign, the visible streak camera and its timing fiducial beam line had to be removed. Instead, three HOPG spectrometers and alignment cameras for the adjustment of the *PHELIX* laser focal spot were installed (see figure 5.3). With the setup designs of the first campaign, it was not possible to alternate between characterizing the laser-driven shock by velocity measurements and the X-ray scattering experiment. Therefore, no changes of the *nhelix* laser system parameters were possible after completing the velocity measurements in this campaign. This situation was different in the second campaign. Here, an experimental setup design could be realized which allowed that all diagnostics for both velocity and X-ray scattering measurements could be in place at the same time (see figure 5.4). Furthermore, two additional curved HOPG spectrometers were mounted, covering the scattering angles 38° and 105°. A 10 cm target chamber extension flange was necessary to achieve the optimal imaging properties of the available HOPG crystals for the 105° and 126° scattering spectrometers.

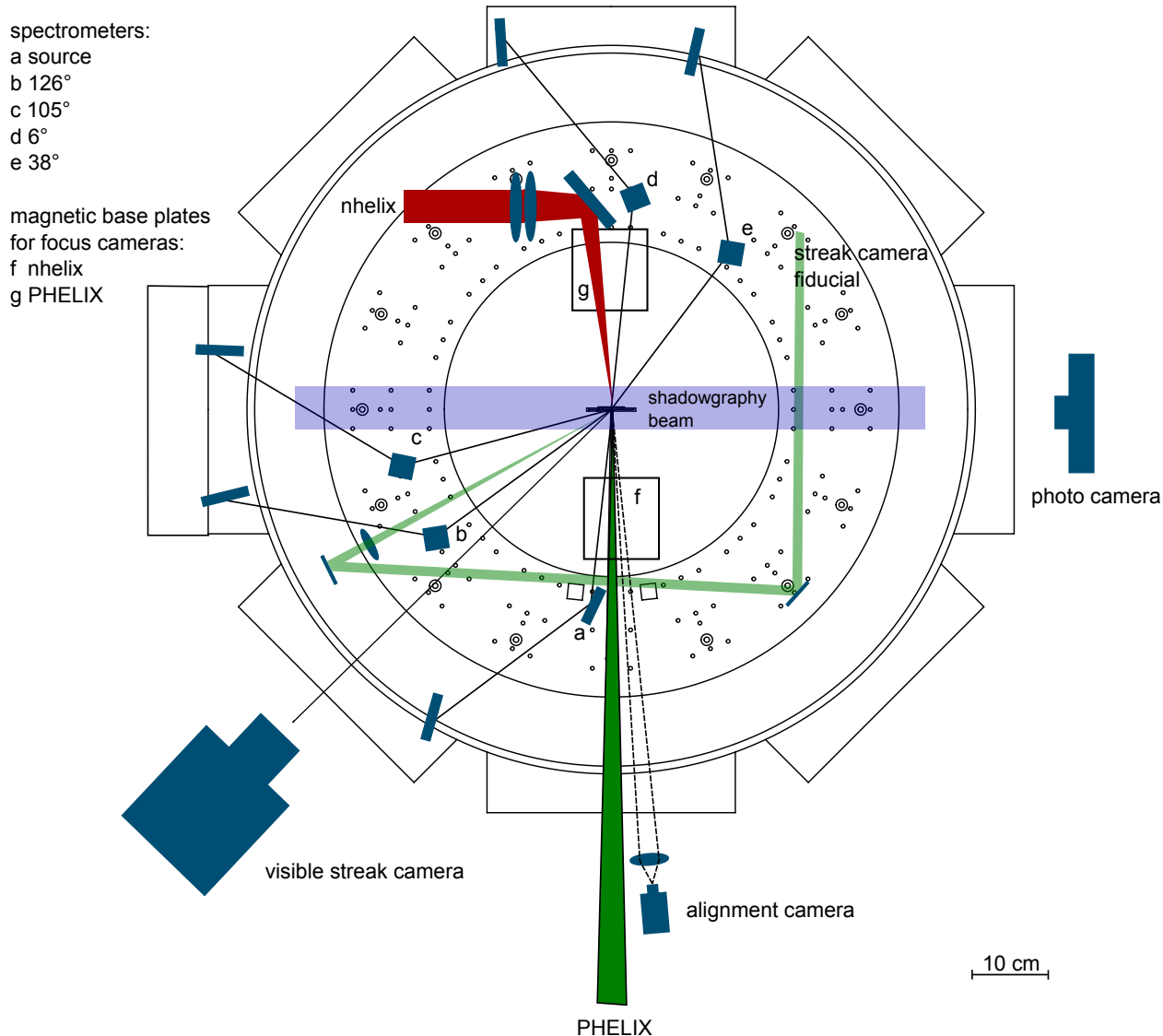


Figure 5.4: Schematic of the experimental setup in and around the target chamber during the second experimental campaign. Both the diagnostics for velocity and X-ray scattering measurements are in place at the same time. Therefore, it was possible to alternate between characterizing the laser-driven shock by velocity measurements and the X-ray scattering experiments.

The typical sequence of steps for both experimental campaigns was as follows: First the shock drive was optimized by tuning the focus of the drive laser. If the surface of the shock breakout was smooth and the shock transit time in favored regions, the focusing lens was not touched any longer. Then, the shock transit was characterized using different graphite sample thicknesses, the visible streak camera and the shadowgraphy. Now, the alignment of the HOPG spectrometers could be checked by focusing the *PHELIX* laser onto a free-standing titanium foil. If the titanium-helium- α line transition is not monitored by all spectrometers, they can be realigned. The next step are so called "Null shots" where a backlighter cone is irradiated by *PHELIX* without a carbon sample being in place. These tests are very important to ensure only scattered radiation reaches the scattering spectrometers. Therefore, exclusively the source and the transmission spectrometers should detect titanium helium- α radiation in this case. The scattering spectrometers should not see anything. "Null shots" can also be used to reduce the background on the scattering spectrometers. Finally,

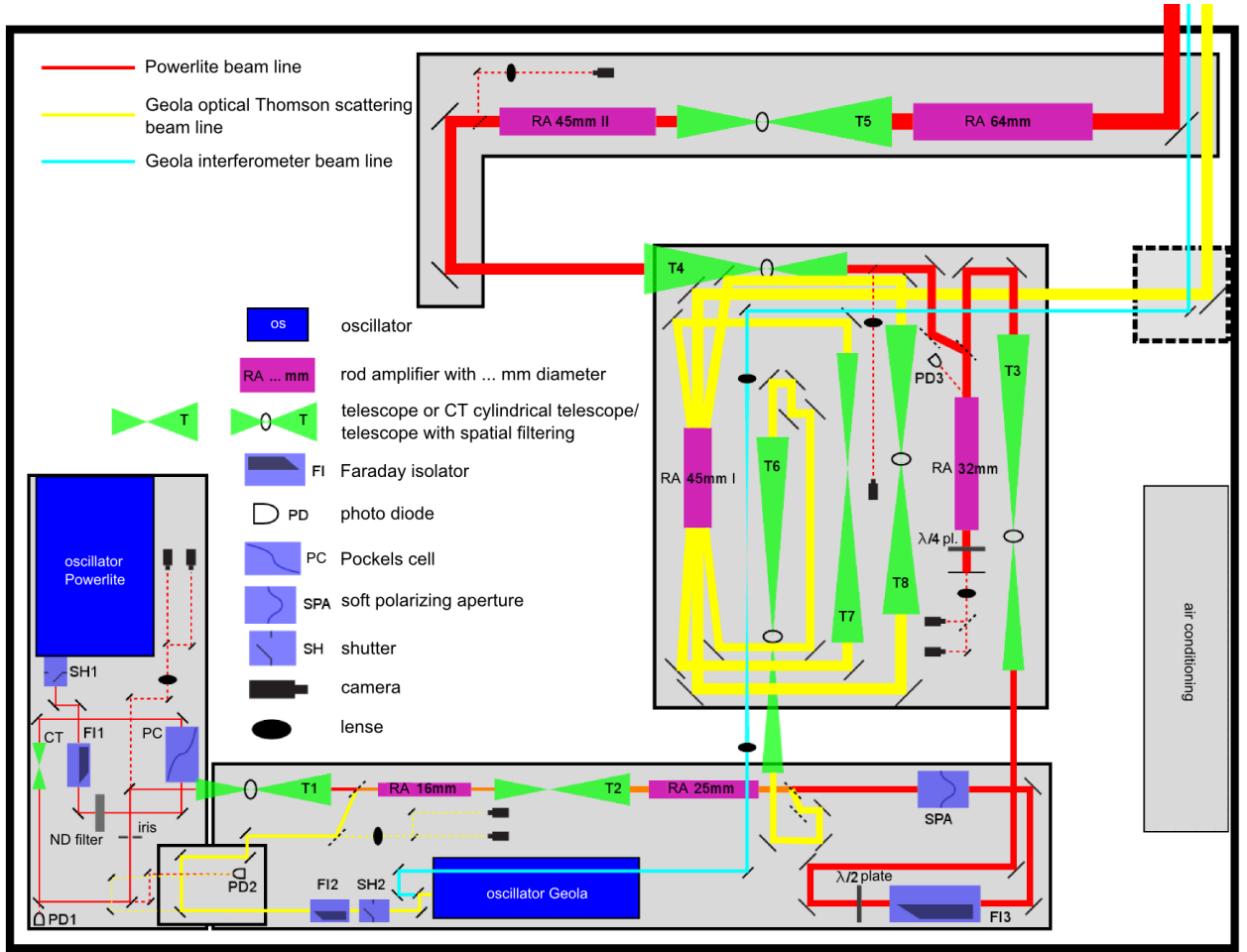


Figure 5.5: Schematic of the *nhelix* laser system [Schumacher, 2007].

the graphite samples can be mounted and scattering from cold samples as well as from shocked samples can be performed alternating in arbitrary order. The setup of the second experimental campaign additionally allowed for another characterization of the laser-driven shock by velocity measurements in between.

5.1.1 The *nhelix* laser system

In all experiments the Nd:YAG/glass laser system *nhelix* (**n**anosecond **h**igh **e**nergy laser for **i**on beam experiments) [Schaumann et al., 2005] was used for the shock drive, shadowgraphy diagnostics and streak camera timing fiducial. The *nhelix* system contains two oscillators, Powerlite Precision 8000 (which will be called Powerlite in the following) and Geola Mini B100 GSI (which will be called Geola in the following), for the generation of the primary laser pulses. Additionally, there is a chain of flash-lamp-driven Nd:glass rod amplifiers and various pulse cleaning elements (spatial filters, soft polarizing aperture, see figure 5.5).

The Powerlite oscillator, a Q-switched Nd:YAG oscillator (1064 nm wavelength), delivers a laser pulse with a Gaussian time profile, containing ~ 200 mJ in 15 ns (FWHM). Directly behind the oscillator, an external Pockels cell is available to generate shorter pulse lengths with, compared to the primary pulse, steeper rising and falling edges of the time profile. The shortest available pulse length that can be obtained with this Pockels cell is 6 ns. In the experiments presented in this thesis pulse lengths of 9-11 ns (FWHM) were used. The temporal pulse profile is measured with a photo

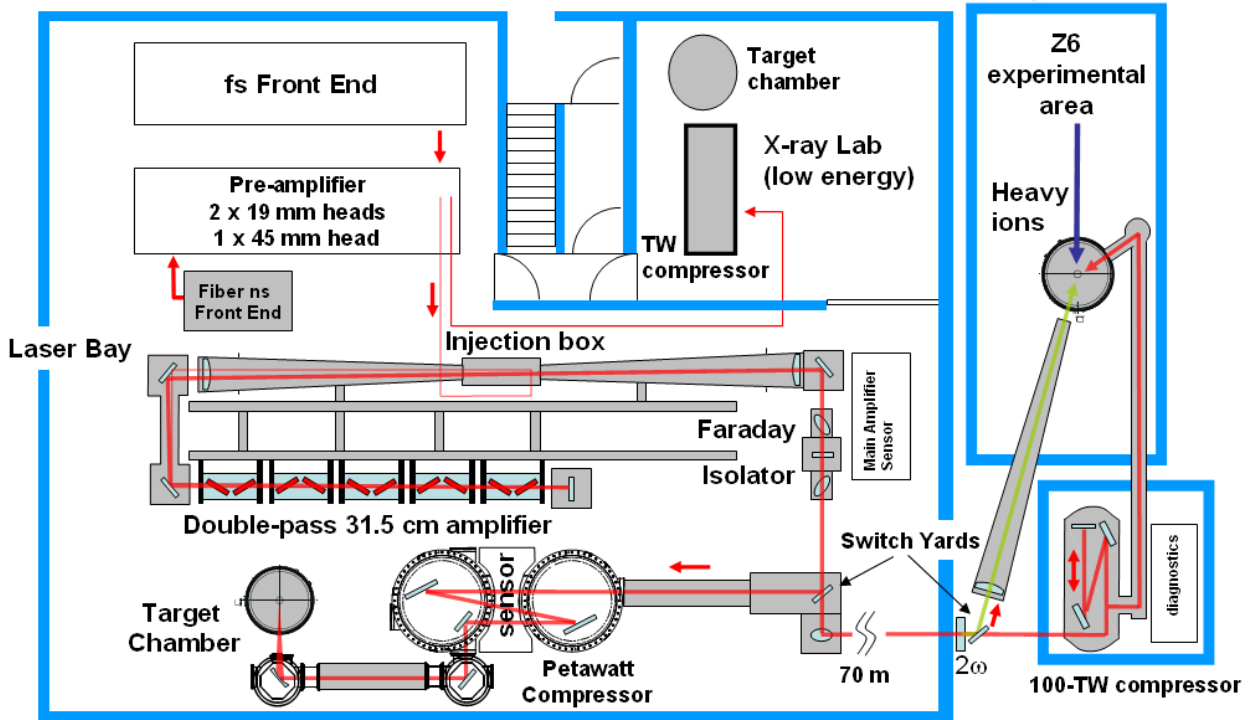


Figure 5.6: Schematic of the *PHELIX* laser system [Bagnoud et al., 2010].

diode directly behind the Pockels cell. The pulse energy can be varied by tuning the voltage of the capacitors which drive the flash lamps of the amplifiers. The maximum pulse energy that can be achieved with *nhelix* is, in the current setup, ~ 100 J in 10 ns. Due to a growing damage inside the last amplifier rod (64 mm), the corresponding amplifier is at present only weakly pumped and the other amplifiers are not driven at the limit, too. Therefore, the maximum pulse energy achieved during the experimental campaigns presented in this thesis did not exceed ~ 70 J. The repetition rate of the full energy system is 60 minutes.

The Geola oscillator is also a Q-switched Nd:YAG oscillator with a fundamental wavelength of 1064 nm. The primary pulses of 5 ns in length are shortened with a SBS (stimulated Brillouin scatter) cell to a pulse length of 500 ps and the energy of one pulse is typically around 120 mJ. The Geola pulse can be injected into two different beam lines (compare figure 5.5). The yellow beam path, which was originally designed for optical Thomson scattering experiments [Müssig, 2008], is currently not in operation. For the experiments presented in this thesis, only the relatively simple beam line marked in blue is important. It is used to transfer the Geola pulse through two BBO crystals for frequency tripling towards the optical ring which generates the pulse train needed for the shadowgraphy of the target rear side expansion. This specific diagnostics is presented in detail in section 5.2.2. Additionally, a frequency-doubled fraction of the original Geola pulse is used as a timing fiducial for the visible streak camera which was applied for the measurement of the shock transit time through the carbon samples. This diagnostics is explained in detail in section 5.2.3.

5.1.2 The *PHELIX* laser system

A schematic of the basic build-up of the *PHELIX* laser system at GSI is illustrated in figure 5.6. There are two separate front ends which generate laser pulses with pulse durations of either 0.7 ns to 20 ns (nanosecond front end) or 500 fs to 10 ps (femtosecond front end). The fundamental wavelength of both front ends is 1053 nm. After passing through several Nd:glass amplifier sec-

tions and various pulse forming elements, the laser pulses can be delivered to three different target areas: Z6 (which was used by the experiments presented in this thesis), X-ray lab and the target chamber in the *PHELIX* laser hall.

For the experiments in the framework of this thesis, only the nanosecond front end of *PHELIX* was applied. This is based on a continuous wave fiber laser. After passing through a pulse generator and a fiber amplifier, an intensity modulator forms pulses with nearly arbitrary temporal profile and a pulse duration of 0.7 ns to 20 ns. A regenerative amplifier stage then raises the pulse energy to ~ 20 mJ. The repetition rate of the nanosecond frontend is 0.5 Hz. The following pre-amplifier section increases the pulse energy to ~ 10 J which can then be sent to the double-pass main amplifier. There, five flash-lamp-driven Nd:glass disc amplifiers can boost the pulse energy up to 1 kJ in 10 ns. In fact, the pulse energy limit is not set by the amplifiers but by the damage threshold of the Faraday rotator after the main amplifier section. The maximum infrared energy that could be used for the experiments in the framework of this thesis was 300 J in 1 ns. In the transport beam line towards Z6, a DKDP crystal is used for frequency doubling the infrared to green ($\lambda=527$ nm). This crystal has a conversion efficiency of roughly 50 %. Therefore, the maximum energy for the X-ray generation in the experiments was ~ 150 J in 1 ns. Finally, the laser pulse is focused by a lense with 4 m focal length to a focal spot of ~ 100 μm in diameter. The repetition rate of the full energy system is 90 minutes.

5.2 Realization and characterization of laser-driven shock waves

As described in the previous section, the laser system *nhelix* was used for the shock drive of the carbon samples. For the characterization of the thermodynamic state in the shock wave, two velocities had to be measured. In the experiments, these were the shock velocity and the expansion velocity of the shock breakout at the target rear side, the so-called free surface velocity (compare chapter 3.5). The characteristics of the applied carbon targets and the instruments for the velocity measurements are presented in this section.

5.2.1 Carbon targets

The applied carbon targets were samples of isostatically pressed synthetic polycrystalline graphite (quality standard R6650, manufactured by *SGL Carbon*). The density of all graphite targets was 1.84 g/cm^3 , which is 81.4 % of the ideal graphite crystal density of 2.26 g/cm^3 . Therefore, the targets were porous materials in the sense of chapter 3.5.2 which simplifies reaching higher temperatures in the shocked matter. For possible comparisons with past and future experiments, further properties of the applied graphite samples, which are relevant for shock compression, are listed in the following tabular [SGL Carbon, 2012].

property	value	test standard
average grain size	7 μm	-
bulk density	1.84 g/cm^3	DIN IEC 604113/203
open porosity	10 Vol. %	DIN 66133
medium pore size	0.8 μm	DIN 66133
compressive strength	0.15 GPa	DIN 51910
ash value	<100 ppm	DIN 51903

The sample dimensions were $5 \times 3 \text{ mm}^2$ and the thickness was varied from 50 μm to 200 μm . The accuracy of the thickness, which was determined by weighing the samples, is 5 μm . As pressed polycrystalline graphite is naturally a material with a very rough surface (root mean square (RMS)

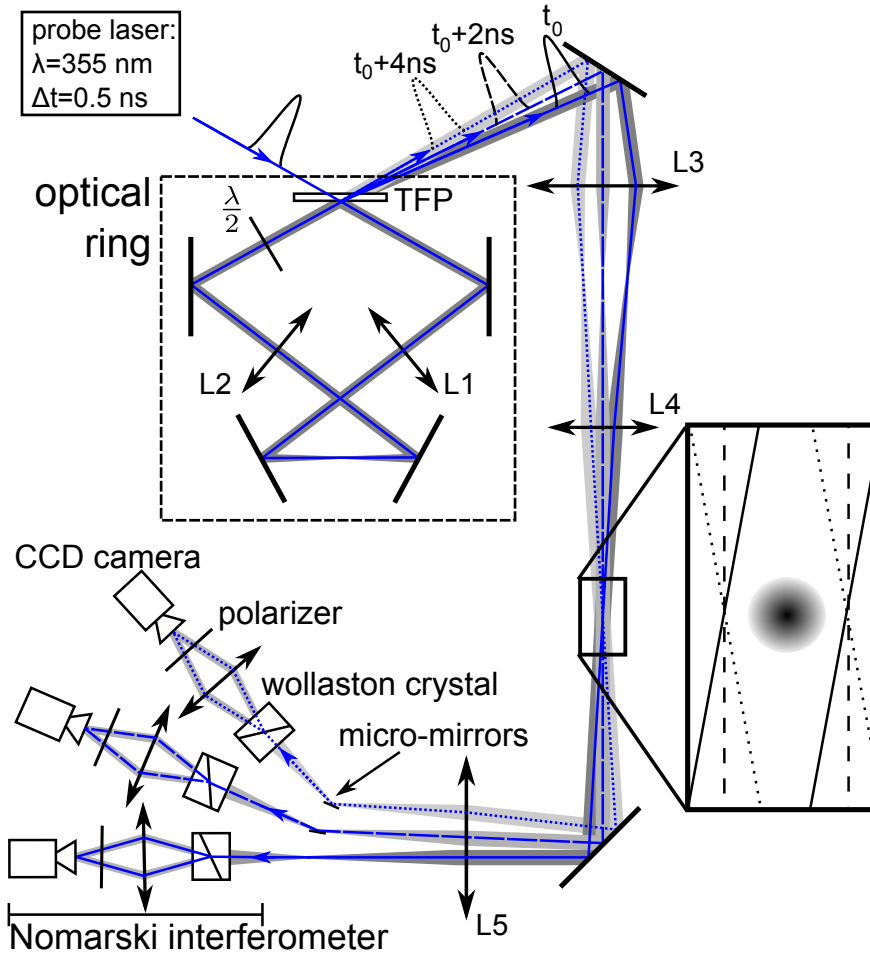


Figure 5.7: Schematic of the multi-frame Nomarskii interferometer which is available at GSI [Börner et al., 2012].

roughness of the order $\sim 10 \mu\text{m}$), the samples had to be specially machined to guarantee a smooth shock drive. There exists, indeed, the so-called shock stability [Drake, 2006] which typically reduces the inhomogeneities of a shock front over propagation time. Nevertheless, the influence of already present laser focus inhomogeneities should not be intensified by a large surface roughness. Therefore, the surface facing the drive beam was elaborately polished by the target laboratory of the GSI Helmholtzzentrum für Schwerionenforschung. Finally, a satisfactory RMS surface roughness of $\sim 100 \text{ nm}$ could be achieved. This was measured by an atomic force microscope (AFM) of the material science division at GSI. Furthermore, the target rear side was polished as well, but not with such an effort. To guarantee a smooth target thickness for the velocity measurements, which directly looked at the target rear side, an RMS surface roughness of $\sim 1 \mu\text{m}$ was machined on this side.

5.2.2 Shadowgraphy

The multi-frame shadowgraphy instrument, which was applied as diagnostics of the expansion velocities of the shock breakout, is originally an imaging interferometer to measure the time-dependent free electron density evolution of laser-driven plasmas [Börner et al., 2012; Frank, 2012]. However, by detuning the interference fringes, this diagnostics well serves as a multi-frame shadowgraphy. In addition to the shock characterization, the shadowgraphy could also be used for expansion studies of the targets for X-ray production.

The heart of this instrument is an optical ring device which generates a laser pulse train where the exiting single pulses have a fixed time delay of 2 ns. The working principle of this device is as follows (see figure 5.7): A thin-film polarizer (TFP), which forms the entrance into the optical ring, transmits only the p-polarized part of the frequency-tripled Geola oscillator pulse into the ring. The s-polarized part is reflected and this reflex is the first pulse of the pulse train. Inside the ring, which is defined by four mirrors, the polarization angle is rotated by a $\lambda/2$ plate. A fraction of the laser light is then extracted by the thin-film polarizer out of the ring. This is the second pulse of the pulse train. An afocal imaging system, consisting of two lenses inside the ring (L1 and L2), images the rear side of the thin-film polarizer on itself. Therefore, the beam profile is conserved. After every round-trip, another fraction of laser light is extracted. The 2 ns time-delay of the single pulses is given by the optical path length which is defined by the fixed mirrors and thus cannot be changed. The separate pulses leave the optical ring with slightly different pointing angles due to a small tilt of the thin-film polarizer. In the following, the surface of the thin-film polarizer is imaged to the laser-plasma interaction zone inside the target chamber by two lenses (L3 and L4). In this way, the different pointings again overlap in the region of interest. After passing the laser-plasma interaction zone, the different pointing angles are still present. This characteristic is used to image the time shifted pulses onto separate cameras, one for each pulse. This is done by small mirrors and another lens (L5). Further details on the construction and design of the whole multi-frame interferometry instrument can be found in the Master Thesis of Michael Börner [Börner, 2010].

5.2.3 Streak camera

As the material inside the shock wave is heated up to several thousand degrees, the shock release on the target rear side is combined with the Planckian emission of visible light. This radiation can be detected by sensitive and fast optical cameras if sufficient shielding from the bright light, which is generated at the laser-plasma interaction zone, is ensured. In the experiments presented in this thesis, an optical streak camera, type *HAMAMATSU* C2830 temporal disperser with M2548 slow speed streak sweep unit [Hamamatsu Photonics K.K., 1990], was applied to determine the moment of shock release which gives the shock transit time through the carbon sample. The working principle of this camera is briefly described in this section.

Streak cameras generate time-resolved one-dimensional images by transforming the temporal characteristics of collected light into a spatial profile in one dimension on the detector. The remaining detector dimension gives the spatial information. Considering the *HAMAMATSU* C2830, this principle is realized as follows: The collected light is directed onto a photocathode through a small entrance slit which defines the available spatial dimension of the final pictures. At the photocathode, electrons are produced via the photoelectric effect. These electrons are then accelerated by the high voltage of an accelerating electrode. A time-dependent electric field component, which is generated by two capacitor plates transversal to the direction of the electron propagation, deflects the electrons. Due to this time-dependent deflection, the electrons are then swept across a micro channel plate (MCP) which multiplies the impacting electrons. The amplified electron image finally impinges upon a phosphor screen which emits light where electrons have hit the surface. This phosphor screen is monitored by a triggered CCD camera (16 bit) which produces the final image of the streak camera.

The *HAMAMATSU* C2830 with sweep unit M2548 can apply streak times from 1 ms down to 10 ns. The labeling "slow speed streak sweep unit" has to be seen in the context that the fastest optical streak cameras can reach time resolutions as low as ~ 200 fs [Hamamatsu Photonics K.K., 2010]. As the shock transit times through the carbon samples were expected to be between 10 ns and 20 ns,

the streak time setting of 50 ns was chosen. Because the CCD camera does not image the full area of the phosphor screen, this setting corresponds to a time window of 31.9 ns which can be seen in one image (1024x1024 pixels). The time calibration was performed using a 500 ps reference pulse at 532 nm which could be extracted from the frequency-tripling setup of the shadowgraphy instrument. A faint stray light reflection of this pulse on the target mount was imaged by the streak camera for different time delay settings. This gave a calibration value of (31.2 ± 0.5) ps/pixel. This is not the real time resolution of the streak camera as the entrance slit is not infinitely small. In the experiments presented in this thesis, the slit width corresponds to ~ 15 pixels on the final image. Therefore the temporal resolution of this setting was roughly 500 ps. The reference pulse from the Geola oscillator was still in place within the shock characterization experiments. As the streak camera has an intrinsic trigger jitter, the timing relative to the drive laser and the other diagnostics can directly be reproduced by the presence of the reference pulse.

5.3 X-ray generation and scattering

The X-rays for probing the carbon samples were generated by focusing the *PHELIX* laser system onto a titanium foil of 10 μm thickness. The pulse energy of 150 J in 1 ns was concentrated in a focal spot with ~ 100 μm diameter and resulted in driving intensities of $\sim 10^{15}$ W/cm². These laser intensities efficiently produce helium-like titanium ions (Ti^{20+}) in the highly collisional transport region of the laser-plasma interaction. These conditions result in a high transition rate of the helium-alpha line emission which produces photons of the energy 4.75 keV (see chapter 7.2). For application in X-ray scattering experiments, this bright X-ray source has to be well characterized, especially the radiation spectrum. Additionally, the scattering geometry has to be well defined which means that a large angle-spread should be avoided. Furthermore, it has to be ensured that the spectrometers which record the scattered photons from the carbon sample are perfectly shielded from the direct light of the backlighter laser-plasma interaction. The target design and alignment methods which were able to fulfill these requirements for the experiments presented in this thesis as well as the X-ray spectrometers for the characterization of the source and scattered radiation are described in this section.

5.3.1 X-ray backlighter target design and fabrication

The target design is maybe the most crucial element in laser-based X-ray scattering experiments for the characterization of warm dense matter samples. Typically, the WDM samples are very small (several hundred microns). Therefore the laser-driven X-ray source has to be placed very close to the object of interest that a high number of photons can be used for probing. Thereby, all requirements for shielding, angle-spread and open lines-of sight for the spectrometers and alignment cameras have to be considered.

The design which was chosen in the experiments presented in this thesis is shown in figure 5.8. The drive beam of the *PHELIX* laser system is guided through a cone which is drilled into an aluminum housing. A two-stepped cone structure made of gold is mounted on the opening of the aluminum cone. The titanium target foil is glued on the step inside the gold cone structure. This results in a distance of the titanium foil to the pinhole between 250 μm and 270 μm . The wall thickness of the gold structure is 15 μm to 20 μm which ensures a sufficient shielding of the 4.75 keV X-rays. The pinhole with a diameter of 120 μm guides the generated X-rays onto the carbon sample and defines the scattering geometry. The distance of the pinhole to the carbon sample is 250 μm which leaves enough space for a line-of-sight from the probed target region to the two scattering spectrometers in backscattering geometry. An additional shine-shield on the aluminum housing prevents radiation of the large plasma plume to be seen by these two spectrometers.

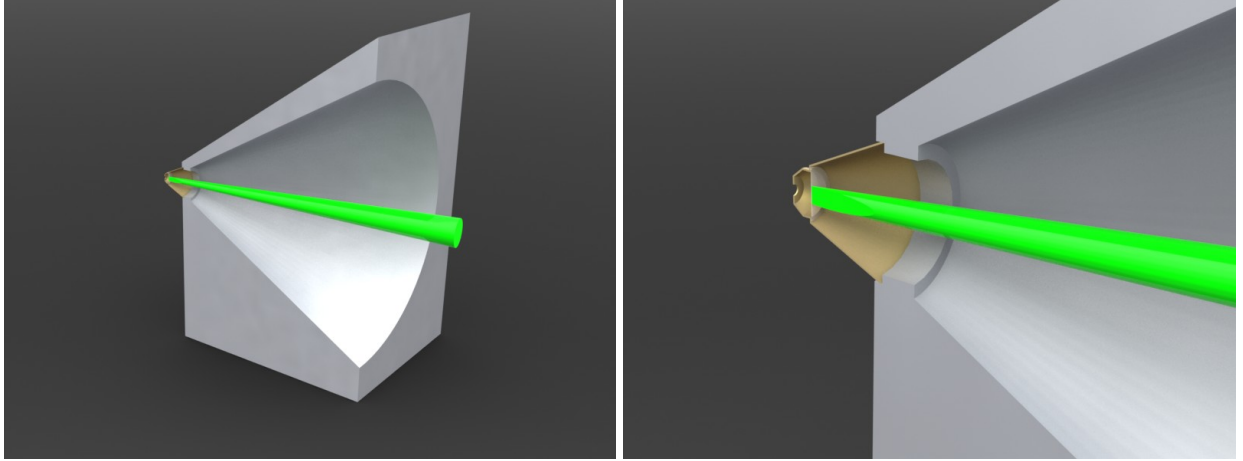


Figure 5.8: Cut through the backlighter cone: The aluminum cone and the two-stepped gold cone with embedded titanium foil and pinhole are drawn together with the incident backlighter laser (thanks to Gabriel Schaumann).

This concept was realized by the detector and target laboratory of TU Darmstadt. Especially the fabrication of the two-stepped gold cone structure with the embedded titanium foil is rather complex and time-consuming. As a first step, blanks made of brass are formed by a computer-guided turning lathe. These blanks are then coated with gold in an electroplating bath. In the following, a precise computer-guided laser-cutting assembly removes most of the gold at the edges of the pinhole and the cone entry. These edges are then cleaned from the last gold remnants by shortly dunking them into a bath of nitrohydrochloric acid (aqua regia). In the next step, the brass blank is dissolved in a bath of nitric acid which leaves the finished gold cone structure. Finally, the titanium foil which was prepared by the computer-guided laser-cutting assembly is placed under a microscope onto the step in the gold cone and is fixed with instant adhesive. It is to mention that every production step requires precise measurements using microscopes to ensure the required specifications.

5.3.2 Alignment methods

Since there are two target components (the backlighter and the carbon samples) and two laser systems (backlighter drive and shock drive) involved in the experiments, sophisticated alignment methods are necessary. The backlighter and carbon targets were positioned relative to each other using special mechanical six-axes micro-manipulators which are mounted on a magnetic base plate. The positions were defined using a pre-alignment setup which was placed next to the target chamber and consisted of two spatially calibrated cameras. The aligned target components could then simply be transferred to the magnetic mount inside the target chamber. The motorized six-axes target manipulator then moves the target to the absolute position inside the chamber.

Figure 5.9 shows a regular image of an aligned combination of backlighter target and carbon sample on the left side. On the right, the time-integrated laser-plasma interaction is imaged. Information that can be obtained from these two pictures is for example that the additional shine shield mounted at the aluminum housing of the backlighter cone is really necessary to shield the spectrometers from the plume of the plasma corona. Furthermore it is clearly visible that the impact of the *nhelix* shock drive is at the right height compared to the end of the gold cone which contains the titanium foil.

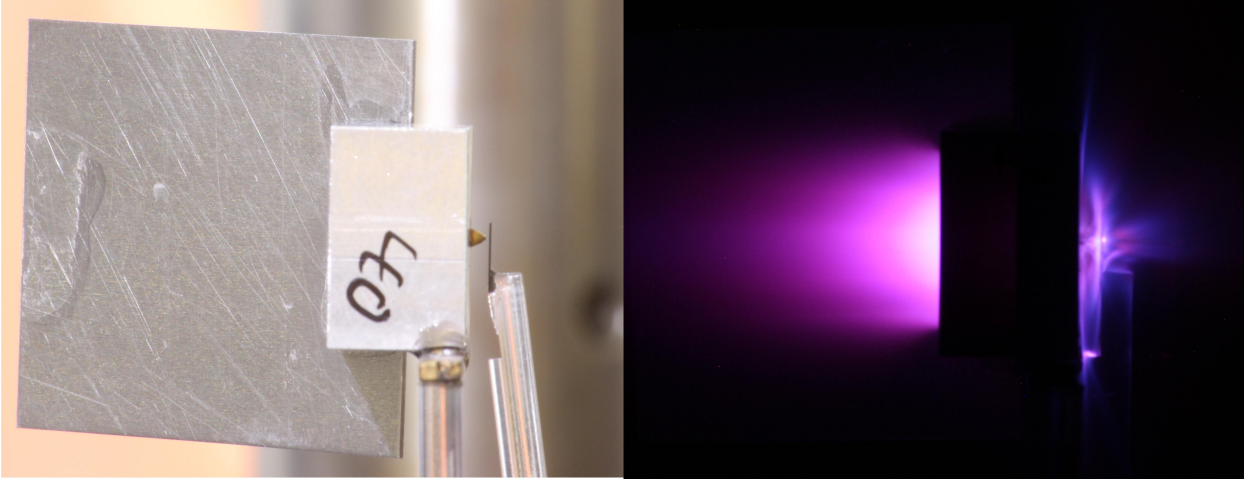


Figure 5.9: Picture of the aligned targets inside the target chamber and the time integrated image of the interaction with the two lasers. The *PHELIX* laser is focused into the backlighter cone from the left and *nhelix* is hitting the carbon foil from the right.

5.3.3 HOPG crystals

The measurement of the relatively faint scattering signals necessarily requires high efficiency X-ray spectrometers with high spectral resolution. This is usually obtained with X-ray diffraction from crystal planes where constructive interference occurs if a Bragg condition is fulfilled:

$$\sin \theta_B = m \frac{hc}{2E_{ph}d} \quad (5.1)$$

Here, θ_B , the so-called Bragg angle, is the angle enclosed by the incoming radiation and the crystal plane, m is the diffraction order, E_{ph} the photon energy of the incoming radiation and d the spacing of the crystal planes. In theory, a perfect graphite crystal ($d=3.35 \text{ \AA}$) has the highest available integrated diffraction reflectivity for X-rays ($\sim 6 \times 10^{-3}$ rad for 4.75 keV [Renninger, 1954]). Unfortunately, nature does not provide ideal single graphite crystals which are large enough for spectroscopic applications. Nevertheless, synthetic highly orientated pyrolytic graphite (HOPG), which consists of highly orientated graphite micro-crystallites, nearly reaches the integrated reflectivity value of a flawless crystal [Pak et al., 2004]. Typical values for the standard deviation of the crystallites (mosaics) from a perfectly parallel orientation are 0.1° to 1° . Due to the mosaic spread, the spectral resolution of a HOPG crystal does not approach that of ideal crystals. However, this drawback can partially be overcome using a special geometry: If the experimental setup allows the distances from X-ray source and X-ray detector to the HOPG crystal to be exactly equal, the spectral resolution of the spectrometer will strongly improve. This is due to the so called mosaic focusing effect [del Rio et al., 1998].

HOPG is typically coated on glass substrates which in principal can have an arbitrary shape. Therefore, concavely curved HOPG surfaces are often applied in X-ray scattering experiments to achieve an additional focusing or even imaging effect. The applied geometry for the scattering spectrometers, which were applied in the experiments presented in this thesis, was the so called von Hamos geometry [v. Hamos, 1933]. Here, cylindrically curved crystals will focus X-rays from the source to the detector if, as it is with mosaic focusing, the source has the same distance to the crystal as the detector. The focal line of the von Hamos geometry is along the axis of curvature

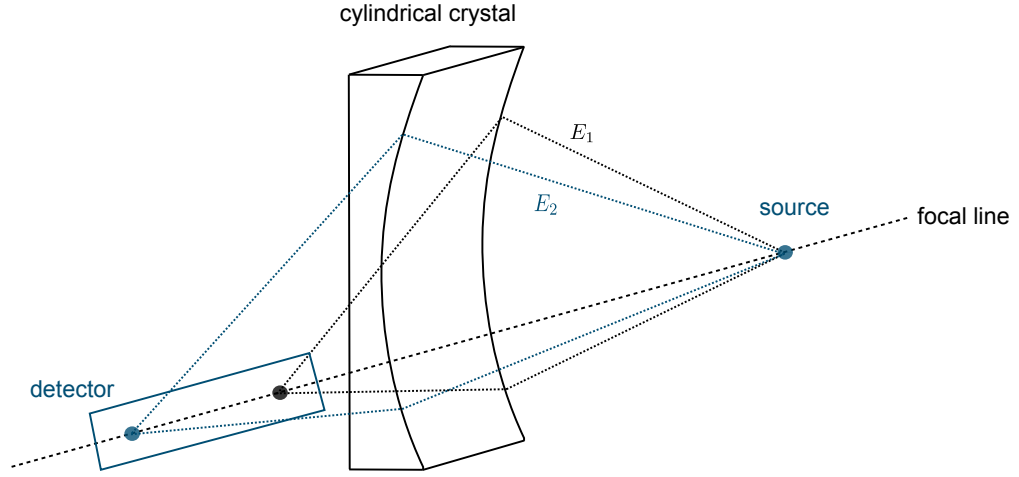


Figure 5.10: Sketch of the von Hamos geometry with a curved crystal for the two different photon energies E_1 and E_2 . In this image, E_2 is larger than E_1 .

of the cylindrical crystal (see figure 5.10). The distance source-crystal and crystal-detector F and the distance source-detector L are in this geometry then simply given by

$$F = \frac{R}{\sin \theta_B} \quad (5.2)$$

$$L = \frac{2R}{\tan \theta_B}, \quad (5.3)$$

where R is the radius of curvature of the crystal. The different parameters of the HOPG crystals which were mounted in the experiments are listed in the following table:

spectrometer	R	geometry	F
source	flat crystal	mosaic focusing	247 mm
transmission	110 mm	mosaic focusing	239 mm
scatter 38°	100 mm	mosaic focusing & von Hamos	257 mm
scatter 105°	110 mm	mosaic focusing & von Hamos	282 mm
scatter 126°	110 mm	mosaic focusing & von Hamos	282 mm

5.3.4 Image plates

The detector which was used to collect the diffracted X-ray spectra from the HOPG crystals were computed radiography image plates (IPs) [Rowlands, 2002; Otten, 2007]. These were originally developed for imaging purposes in medical applications but meanwhile, IPs have also become a very common X-Ray detector in the field of laser-plasma physics [Paterson et al., 2008]. The working principle of image plates is the so-called photostimulated luminescence: Incident X-ray photons excite photostimulable phosphors, which are embedded in a plastic layer, to a meta-stable state. Image plates of the type AGFA MM 3.0 were applied for the experiments presented in this thesis. These use the very sensitive photostimulable phosphor BaSrFBrI:Eu. After exposing the image plates to X-rays, the decay of excited meta-stable states can be stimulated by irradiation of red laser light. Hereby, blue light is emitted which can be collected by a scanning unit. From these light signals, the X-ray signal on the image plate can then be reproduced. The software of the scanner type *Fuji Film FLA-7000*, which was applied in the experiments presented in this thesis,

first produces a raw 16 bit gray value image. This image is then converted to the more practical PSL unit using the formula:

$$\text{PSL} = \left(\frac{\text{px}}{100} \right)^2 \times \frac{4000}{S} \times 10^{L \left(\frac{\text{QL}}{G} - 0.5 \right)}. \quad (5.4)$$

pix	pixel size in μm = 50
S	sensitivity = 10000
L	latitude setting = 5
QL	gray scale level of the pixel = values between 1 and 65536
G	number of total gray scale levels = 65536

The intensity of the photostimulated luminescence directly scales with the X-ray dose to which the image plate was exposed. This scaling is linear over many orders of magnitude [Paterson et al., 2008] and the photon energies, which can efficiently be detected, range from few ten eV [Ben-Kish et al., 2000; Kraus, 2009] to several hundred keV [Meadowcroft et al., 2008]. By handling the image plates in an experiment, one should bear in mind that also red photons from ambient light can stimulate the decay of the meta-stable states. Therefore, it is important to keep image plates in the dark from exposure to readout. Another issue is that the excited states decay over time with a half life of the order of one hour [Meadowcroft et al., 2008; Philipp, 2011]. Thus, it is useful to assign the same time interval from exposure to readout for image plates which signals have to be compared quantitatively in intensity.

In the experiments presented in this thesis, the image plates were protected by a closed housing and filters from visible and XUV light inside the target chamber. The detectors of the transmission and source spectrometers were covered with thin aluminum foils. By stacking these foils, the signal level of the source and transmission spectrometers could be adjusted to useful values. During the first experimental campaign, the detector of the scattering spectrometer was shielded by a 125 μm thick beryllium foil. Beryllium is a very useful material for completely blocking visible and XUV light and efficiently transmitting X-rays at the same time. However beryllium foils are very brittle and easily disintegrate. The resulting dust is very toxic. Therefore, beryllium foils have to be specially secured in an experiment which complicated the access to the target chamber in this case. As two more scattering spectrometers were in place in the second campaign, the beryllium filters were replaced by black plastic foils in the second experimental campaign because of practical reasons. This resulted in a slight increase of the background levels of the scattering spectrometers. However, the signal-to-noise ratio was still acceptable in the second campaign and the experimental work was much less complicated.

6 Simulations

For the experiment design and the analysis of the data obtained by the two experimental campaigns presented in this thesis, simulations were necessary. This holds true for the hydrodynamics of the laser-driven shock wave as well as for the microscopic structure of the achieved warm dense matter state of carbon. The applied simulation methods and the obtained results are presented in this chapter.

6.1 Hydrodynamics of the shock waves

As described in chapter three, the interaction of an intense laser with a solid state sample can be modeled using hydrodynamics in combination with radiation transport. Thus, a code package for simulating the laser-matter interaction with hydrodynamics basically needs to solve the Euler fluid equations:

$$\frac{\partial \rho}{\partial t} + \vec{\nabla}(\rho \vec{v}) = 0 \quad (6.1)$$

$$\frac{\partial(\rho \vec{v})}{\partial t} + \vec{\nabla}(\rho \vec{v} \vec{v} + P) = \vec{f}_{\text{ext}} \quad (6.2)$$

$$\frac{\partial(\rho \epsilon + \frac{1}{2} \rho \vec{v}^2)}{\partial t} + \vec{\nabla} \left[\vec{v} \left(\rho \epsilon + \frac{1}{2} \rho \vec{v}^2 + P \right) \right] = -\vec{\nabla} \vec{j}_{\text{therm}} - \vec{\nabla} \vec{S} + q_{ib}. \quad (6.3)$$

Hereby, the important quantities are the sources and sinks of energy density in equation (6.3): laser energy absorbed by inverse bremsstrahlung q_{ib} , heat conduction $-\vec{\nabla} \vec{j}_{\text{therm}}$ and total radiation transport $-\vec{\nabla} \vec{S}$. The latter has to be calculated by integration of the radiation transport equation over all frequencies (compare chapter three):

$$\vec{\nabla} \vec{S} = c \int d\omega \kappa_{\omega} (u_{\omega, \text{Planck}} - u_{\omega}). \quad (6.4)$$

However, equations (6.1) to (6.4) do not yet form a completely closed system. In addition, a working radiative hydrodynamic code necessarily requires the equation of state as well as the opacities of all applied materials:

$$\epsilon = \epsilon(\rho, P) \quad (6.5)$$

$$\kappa_{\omega} = \kappa_{\omega}(\epsilon, \rho, P). \quad (6.6)$$

Thus, equations (6.1) to (6.6) finally form the system of equations that has to be solved. Thereby, the equation of state and the opacities are the most crucial input because those are not sufficiently known for hot dense plasma states or warm dense matter. Typically, approximate semi-empirical tables, like the very common SESAME database [Lyon and Johnson, 1992], are used to estimate the equation of state and opacities in radiative hydrodynamic codes.

For modeling a physical system in a code, the closed system of equations has to be discretized on a numerical grid. Thereby, two different coordinate approaches are typically applied: On the

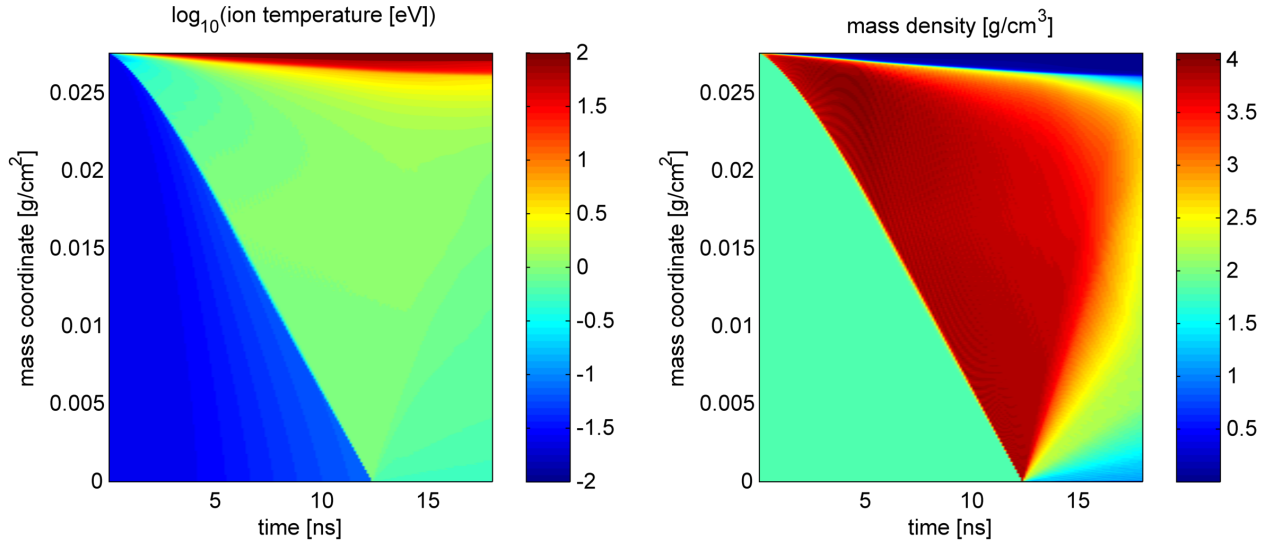


Figure 6.1: 1D simulation of a laser-driven shock in graphite by HELIOS using the SESAME equation of state.

one hand Eulerian coordinates which leave the numerical grid fixed in space and on the other hand Lagrangian coordinates where the grid cells move and deform in space over time but always enclose the same amount of mass. Therefore, Lagrangian coordinates are often called mass coordinates.

The radiative hydrodynamic codes which were applied in the framework of this thesis were the one-dimensional HELIOS code version 4.4 and the two-dimensional MULTI2D code version 5.1. Both packages, their properties and the results related to laser-driven shocks in graphite are presented in the following subsections.

6.1.1 Simulations with HELIOS

The radiation hydrodynamics code HELIOS is a component of the software package *PRSIM Software tools* from *PRISM-CS* [MacFarlane et al., 2006]. It solves the radiative hydrodynamic equations (either using a two-fluid approach or one fluid only) on a one-dimensional Lagrangian grid where planar, cylindrical or spherical symmetry can be chosen. An artificial fluid viscosity guarantees the stability of shock solutions. The implemented standard heat transfer mechanism is the Spitzer model. Alternatively, it is possible to define a constant heat conductivity or to choose a hybrid option where a mixture of the Spitzer model and a constant heat conductivity is implemented. Furthermore, two radiation transport models can be applied: Either a multi frequency group flux limited diffusion approach or a multi frequency and multi angle group transport model (planar geometry only) can be selected. The HELIOS code can apply the included PROPACEOS equation of state and opacity package as well as SESAME equation of state tables. Because of easy handling and reasonable results, using HELIOS simulations is very common for the analysis of X-ray scattering data from laser-driven shocks [Garcia Saiz et al., 2008; Kritcher et al., 2008; Kugland et al., 2009; Kritcher et al., 2009; Neumayer et al., 2010]:

Figure 6.1 shows HELIOS simulation results of a laser-driven 150 μm thick graphite sample which was discretized into 500 Lagrangian zones. The SESAME table No. 7832 was the applied equation of state and the opacities were calculated from the included PROPACEOS 4.0 tables for carbon. The driving laser intensity of $1.25 \times 10^{13} \text{ W/cm}^2$ was chosen to reproduce the experimentally ob-

served shock transit time of 12.5 ns (see chapter seven) in the simulation. Additionally, the laser time profile was modeled to correspond to the experimental conditions: 4 ns linear rise to the maximum intensity, then 7 ns constant drive at the maximum value and finally again 4 ns linear decrease of the laser intensity to zero. The results which can be seen in figure 6.1 are as follows: Due to the rise time of the laser intensity, the shock speed is increasing during the first 4 ns. After that, the shock front moves with constant velocity through the sample until the moment of shock release at the target rear side at 12.5 ns. The Lagrangian mass coordinates illustrate the amount of homogeneity of the thermodynamic parameters within the shock wave. HELIOS calculates a density of $\sim 3.87 \text{ g/cm}^3$ and a temperature of $\sim 0.95 \text{ eV}$ inside the shocked material for these input parameters.

Using the PROPACEOS tables not only for opacities but also for the equation of state already leads to quite different results: First of all, now a driving laser intensity of $1.0 \times 10^{13} \text{ W/cm}^2$ is necessary to achieve the experimentally observed shock transit time of 12.5 ns. Using PROPACEOS, the calculated density of the shocked material is then $\sim 3.55 \text{ g/cm}^3$ and the temperature $\sim 0.78 \text{ eV}$. Obviously, these deviations underline the poor understanding of carbon in this temperature and pressure regime. For both simulations the preheating of the sample due to radiation transport is well below 0.01 eV (100 K).

6.1.2 Simulations with MULTI2D

Due to the fact that the focal spot of the shock drive was with $\sim 200 \mu\text{m}$ diameter in the same order of magnitude as the thickness of the applied graphite samples, a perfectly one-dimensional shock drive was not realized within the experiments presented in this thesis. Therefore, a two-dimensional simulation of the shock drive was unavoidable to identify and analyze resulting effects. For this purpose, the simulation package MULTI2D [Ramis et al., 2009] was chosen, as this code was already well applied in the laser and plasma physics group of TU Darmstadt [Löb, 2008]. In contrast to HELIOS, the MULTI2D code is available open source, mainly written in C++. Thus, personal modifications are easily possible. The simulation input files have to be coded in the script language r94 [Ramis, 2010]. This allows for a high level of flexibility as the implementation of sophisticated loops, calculations and data access is also possible directly within the input script.

The MULTI2D code was originally developed for handling problems connected to ion-beam-driven inertial confinement fusion [Ramis et al., 1988]. It solves the hydrodynamic and radiation transport equations on a two-dimensional triangular grid using cylindrical symmetry. Thereby, it is possible to choose either Eulerian or Lagrangian coordinates. For radiation transport, a multi-group model is applied which allows for dividing the transport contributions in different solid angle and photon energy groups. For opacity input, tables or simple analytical models can be used. Heat conduction by electrons is modeled by the Spitzer approach or the basic flux-limited transport model. The equation of state input is realized via tables of SESAME-like structure. The implemented inverse-bremsstrahlung-based energy deposition by laser is only a simple modification of the original model of the energy deposition by heavy ion beams. For example, laser light is completely absorbed at the critical density, whereas in reality, some fraction would be reflected. Another deficit of the MULTI2D code is that an ionization model is, so far, completely missing. This is because the main materials of interest for this code have typically been fully ionized hydrogen isotopes. Therefore, the ionization state of the simulated materials has to be defined as initial condition.

For the simulation of the laser-driven shock wave in graphite, Eulerian coordinates with four different spatial regions were applied. Usually, Lagrangian coordinates are preferred in hydro

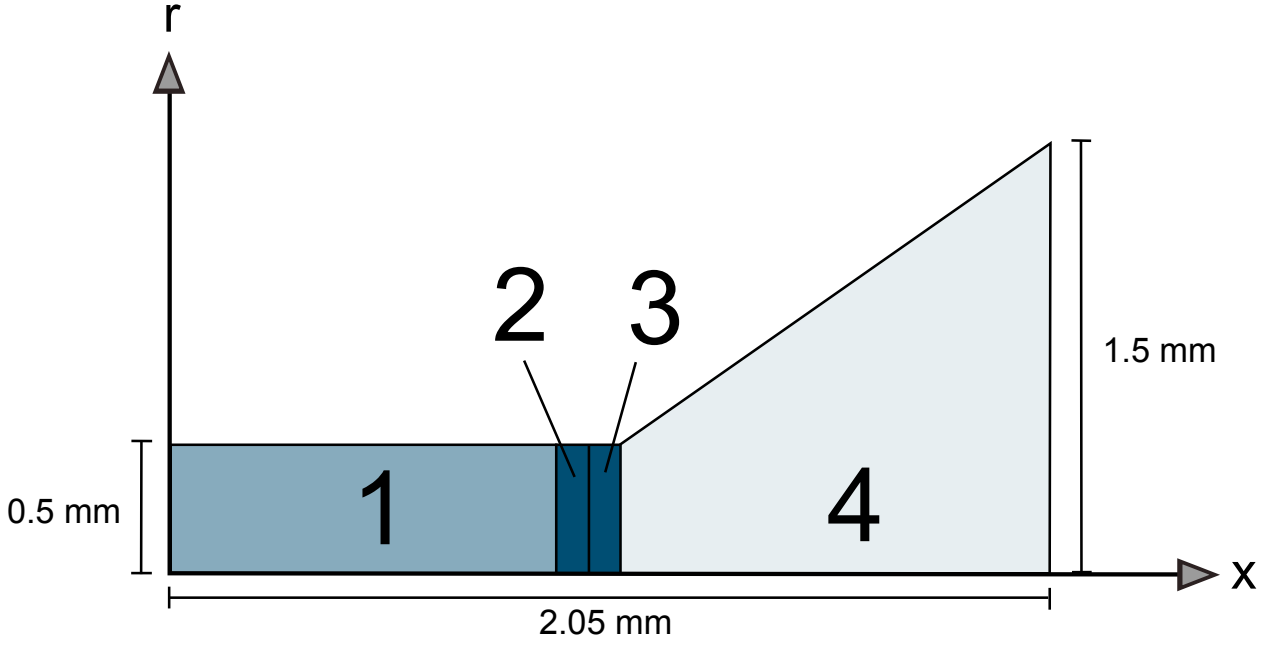


Figure 6.2: Definition of the different simulation regions in the applied Eulerian grid. The drive laser is incident from the right.

simulations because those typically need less grid cells than Eulerian coordinates and therefore less computer time. However, Lagrangian coordinates were not practical in this case as the very fast expansion of the plasma corona resulted in strong zone squeezing or even in overlapping grid boundaries. These two occasions both force the Lagrange calculation to crash. More sophisticated Lagrange codes solve such problems using individual dynamic resizing and reconnection of the Lagrangian grid cells. The implementation of a dynamic rezoning algorithm would in principle also be possible within MULTI2D, but is definitely out of the scope of this thesis. Fortunately, simulations applying Eulerian coordinates resulted in very stable and reasonably fast simulations using a spatial grid with a special zone structure. The applied basic radial and axial grid structure dimensions for these simulations are shown figure 6.2: The laser is incident from the right. In the initial state, regions one and four are filled with a thin carbon gas to ensure numerical stability due to the laser impact and the shock breakout. Furthermore, the right end of region four is larger in radial dimension to cover the most important regimes of the expanding plasma corona. The regions two and three contain the carbon sample. Important quantities for the numerical resolution and stability are the numbers of radial zones $N_{z,r}$, the number of axial zones $N_{z,x}$ and the so-called axial and radial zone factors $\alpha_{z,x}$ and $\alpha_{z,r}$. The latter give the size ratio of neighboring zones in radial and axial direction:

$$\alpha_{z,x} = \frac{\Delta x_{m+1}}{\Delta x_m} \quad (6.7)$$

$$\alpha_{z,r} = \frac{\Delta r_{n+1}}{\Delta r_n}, \quad (6.8)$$

where m, n are the zone indices in axial and radial directions, respectively. The grid geometry parameters of the shock drive simulations are listed in the following table:

region no.	Δx [μm]	material	ρ [g/cm^3]	$N_{z,x}$	$\alpha_{z,x}$	$N_{z,r}$	$\alpha_{z,r}$
1	900	carbon	5×10^{-4}	180	1.00	150	1.00
2	75	carbon	1.84	60	1.01	150	1.00
3	75	carbon	1.84	60	0.98	150	1.00
4	1000	carbon	1×10^{-8}	50	1.04	150	1.00

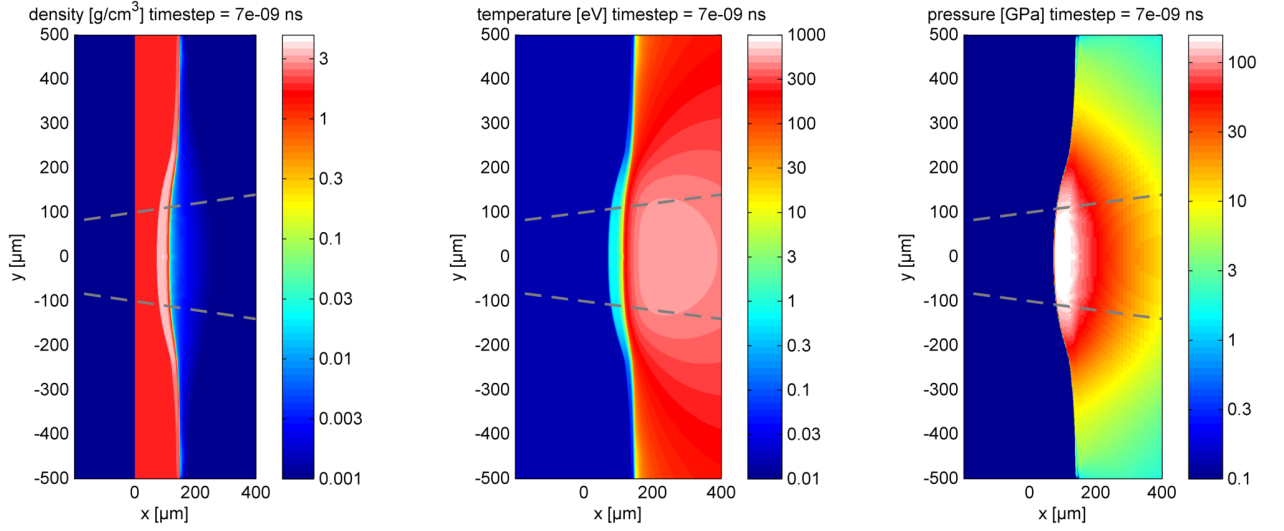


Figure 6.3: MULTI2D simulation: drive laser impact +7 ns.

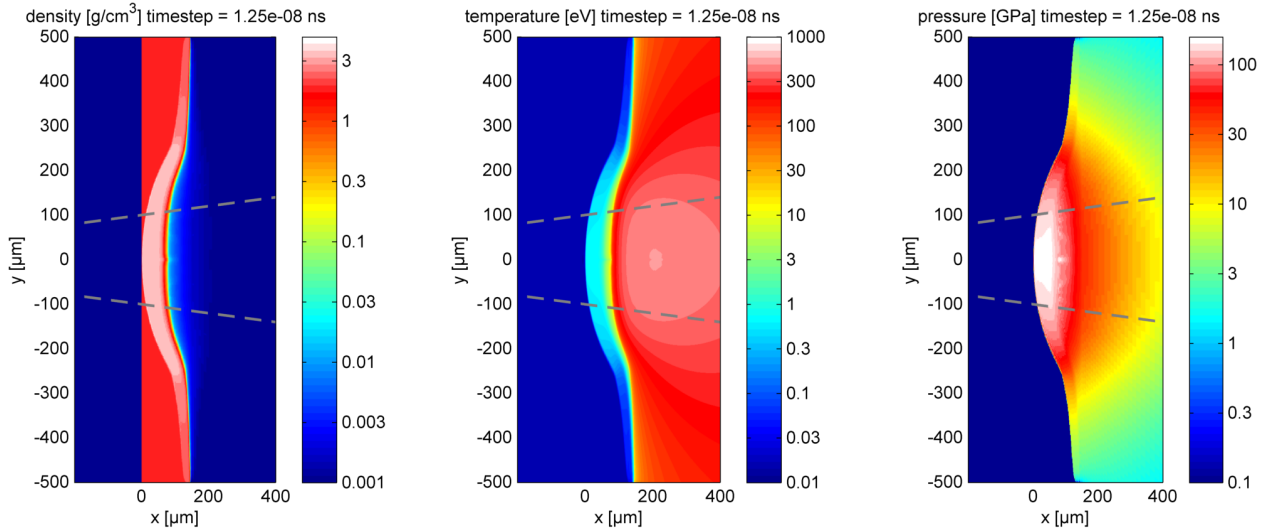


Figure 6.4: MULTI2D simulation: drive laser impact +12.5 ns.

The laser time profile was modeled identically to the HELIOS simulations: 4 ns linear rise to the maximum intensity, then 7 ns constant drive at the maximum value and finally again 4 ns linear decrease of the laser intensity to zero. The laser radial focus profile is represented by a super-Gaussian curve with a width of 220 μm (FWHM). This focal spot profile reproduced the experimentally observed radial dimensions of the shock release very well. A drive laser-intensity of $1.5 \times 10^{13} \text{ W/cm}^2$ then results in a shock transit time of 12.5 ns, as observed in the experiment. The applied equation of state is the SESAME table No. 7832. The opacities are implemented by an analytical model [Murakami et al., 1990].

MULTI2D simulation results of the laser-driven shock for different time steps showing the quantities density, temperature and pressure are presented in figures 6.3 to 6.5. In all pictures the laser is incident from the right. At 7 ns after the shock drive, the laser intensity is at its maximum. At 12.5 ns after the drive laser impact, the shock wave reaches the rear side of the carbon sample. At 17 ns after the drive laser impact, the gradients at the rear side due to the shock release, especially concerning density and pressure, are clearly visible.

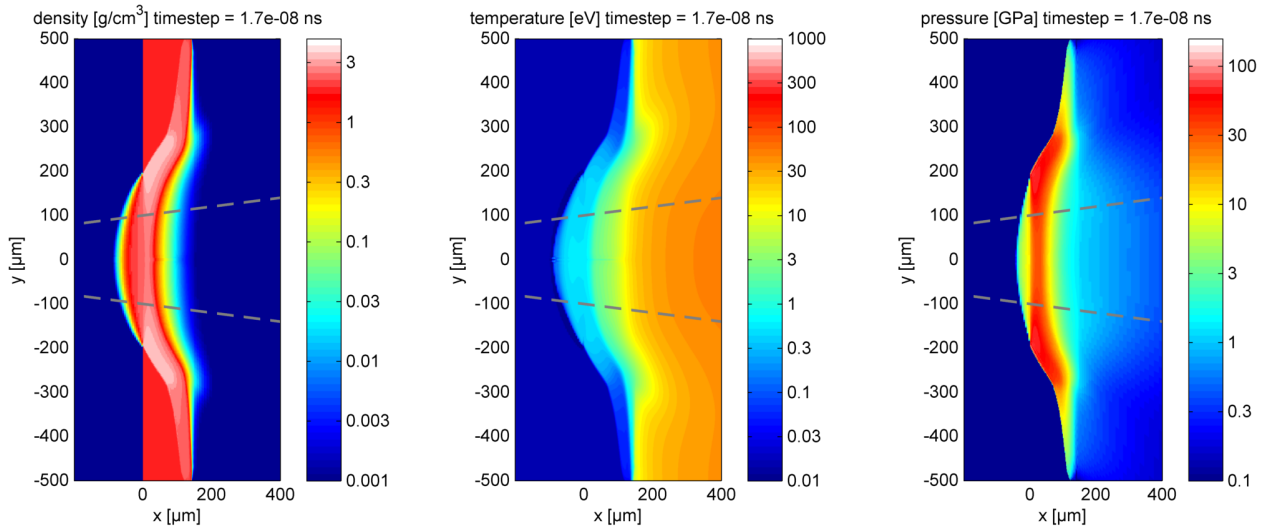


Figure 6.5: MULTI2D simulation: drive laser impact +17 ns.

The channel which was probed by the X-rays in the experiments is shown by gray dashed lines in figures 6.3 to 6.5. While the shock waves propagates within the carbon sample, the thermodynamic parameters are relatively homogeneous inside the regions which are mainly accessed by the X-rays. The hot plasma corona is also covered by the X-rays, but fortunately, it does not give much contribution to the scattering signal. This is discussed in detail in section 7.3. The preheat due to radiation transport is, like in the HELIOS simulations, well below 0.01 eV.

6.1.3 Comparison

Figure 6.6 presents a comparison of HELIOS and MULTI2D simulations of the laser-driven shock for the parameters density, temperature and pressure. Each simulation is shown for the time-step 12.5 ns after the drive laser impact and therefore represents a completely shocked sample. The main difference between the one- and two-dimensional calculations is definitely the size of the transport domain. In the HELIOS simulations, the transport domain is much larger than in the MULTI2D calculations. This can be explained by the fact that the plasma has one more dimension for expansion in the 2D-simulation. This is especially visible in the density and pressure diagrams. However, a similar but smaller difference in the transport domain between HELIOS and one-dimensional MULTI1D simulations has already been described and discussed by [Löb, 2008]. The difference in the applied opacity models (HELIOS: PROPCEOS tables, MULTI2D: analytical function) was most probably responsible for these deviations.

Concerning the thermodynamic parameters inside the shock wave, there are also significant differences between the different simulations. Even the two HELIOS-1D simulations have considerable deviations from each other due to the different equations of state, SESAME and PROPCEOS. Mean thermodynamic values of the shock wave calculated by the different simulations are given in the following table.

simulation	density [g/cm ³]	temperature [eV]	pressure [GPa]
HELIOS - SESAME	3.87	0.95	175
HELIOS - PROPCEOS	3.55	0.78	154
MULTI2D - SESAME	3.76	0.70	147

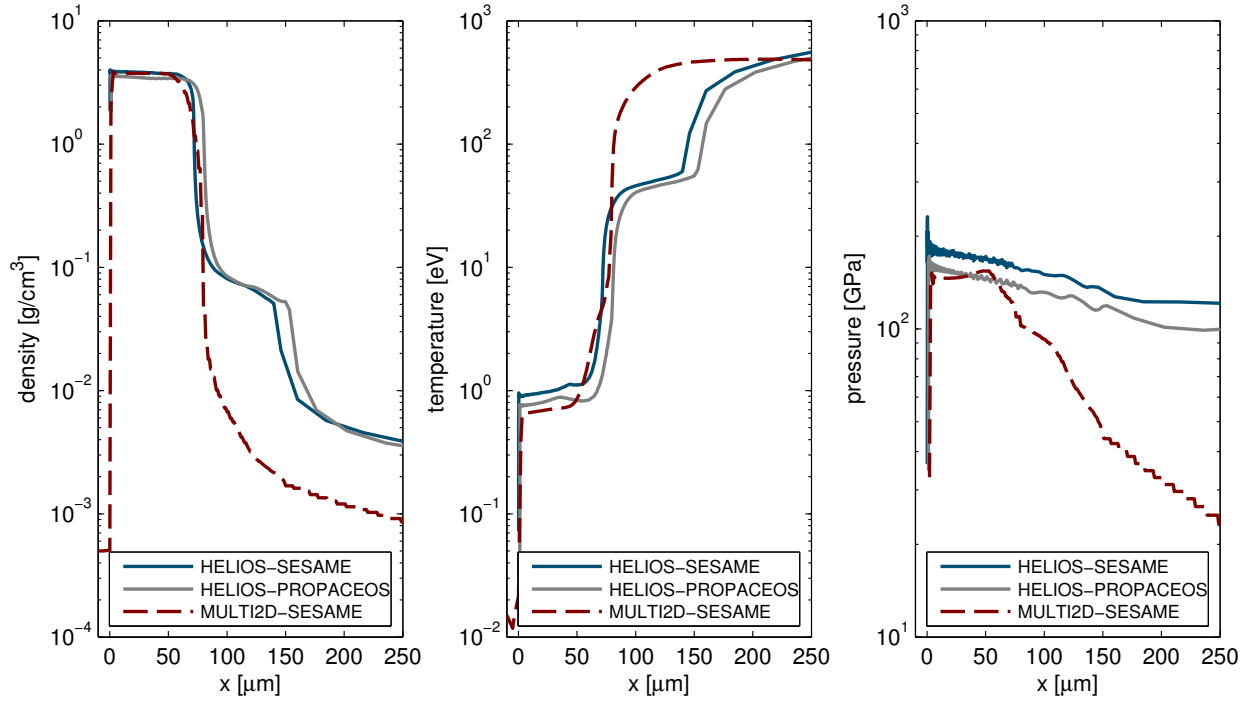


Figure 6.6: Comparison of the thermodynamic parameters density, temperature and pressure in the shock wave for the different simulations.

The deviations of the HELIOS-SESAME simulations from the MULTI2D calculation, which also applied the SESAME tables, is reasonable. As the shock wave undergoes rarefaction in radial direction, the parameters pressure, density and temperature are reduced compared to the one-dimensional case.

In conclusion, it can be stated that hydro simulations are a very valuable tool to estimate the thermodynamic parameters inside the laser-driven shock. However, they do not contain any information about the microscopic structure. This has to be estimated by different tools, for example in the way that is presented in the following section.

6.2 Ab-initio simulations

The final aim of the experiments presented in this thesis was the characterization of the microscopic structure change inside shock-compressed graphite. Therefore, it is important to have theoretical concepts to which the obtained data can be compared for a proper analysis. So far, the most precise tool to calculate the microscopic structure of matter states like shock-compressed graphite in the 100 GPa regime are so-called ab-initio simulations. These were already mentioned in chapter two and will be explained in more detail in this section.

6.2.1 DFT-MD

The most common method for these ab-initio simulations is the application of density functional theory (DFT) in combination with Monte-Carlo simulations of the molecular dynamics (MD). Hereby, the Born-Oppenheimer approximation is used which allows for decoupling the electrons from the ion motion. The latter is treated by classical MD and the electronic forces which effect the ions are determined by a full quantum DFT calculation of the electrons.

The basis of the density functional theory is the so-called Hohenberg-Kohn theorem which states that, for a given system of N electrons with a given potential $V(\vec{r})$, there is only one possible electron density distribution in the ground state [Hohenberg and Kohn, 1964]. Thus, all information about the N -particle quantum system is included in the ground state electron density. To obtain solutions, the interacting electronic system is technically transformed into a virtual system of non-interacting electrons by hiding the interactions in a specially chosen potential, the so-called Kohn-Sham potential [Kohn and Sham, 1965]

$$V_{KS}(\vec{r}) = V_{ext}(\vec{r}) + V_{Hartree}(\vec{r}) + V_{xc}(\vec{r}). \quad (6.9)$$

Here, $V_{ext}(\vec{r})$ is an external potential acting on the electrons, for example the Coulomb potential of the nuclei. The second term, the so-called Hartree term, is the potential generated by the electron density distribution $n_e(\vec{r})$:

$$V_{Hartree}(\vec{r}) = \frac{e^2}{4\pi\epsilon_0} \int d^3r' \frac{n_e(\vec{r}')}{|\vec{r} - \vec{r}'|}. \quad (6.10)$$

The interactions are expressed by the exchange-correlation potential $V_{xc}(\vec{r})$ which is defined by

$$V_{xc}(\vec{r}) = \frac{\delta}{\delta \tilde{n}_e(\vec{r})} E_{xc}[\tilde{n}_e(\vec{r})] \Big|_{\tilde{n}_e(\vec{r})=n_e(\vec{r})} \quad (6.11)$$

where the exchange correlation energy $E_{xc}[\tilde{n}_e(\vec{r})]$ is functionally dependent on the density and contains all the complexities of the many-electron system. With this description, the interacting system of N electrons fulfills a set of N single particle Schrödinger equations:

$$\left[-\frac{\hbar^2}{2m_e} \vec{\nabla}^2 + V_{KS}(\vec{r}) \right] \psi_i(\vec{r}) = \epsilon_i \psi_i(\vec{r}), \quad i = 1 \dots N. \quad (6.12)$$

Here, $\psi_i(\vec{r})$ are single particle wave functions in the virtual Kohn-Sham potential with corresponding energy eigenvalues ϵ_i . The total electron density distribution is then simply given by

$$n_e(\vec{r}) = \sum_{i=1}^N |\psi_i(\vec{r})|^2. \quad (6.13)$$

Knowing the density distribution, the corresponding total ground state energy can be calculated:

$$E[n_e(\vec{r})] = \sum_{i=1}^N \epsilon_i + E_{xc}[n_e(\vec{r})] - \int d^3r V_{xc}(\vec{r}) n_e(\vec{r}) - \frac{e^2}{8\pi\epsilon_0} \int d^3r d^3r' \frac{n_e(\vec{r}) n_e(\vec{r}')}{|\vec{r} - \vec{r}'|}. \quad (6.14)$$

This energy is a functional of the electron density. By using variational methods for this functional, this expression has to be minimized to obtain the ground state electron density distribution. The big advantage of this concept is that highly coupled multi-particle wave functions of the interacting electronic system can be avoided in the solution process. Choosing a proper description of $E_{xc}[n_e(\vec{r})]$, for example the local density approximation [Kohn and Sham, 1965], gives the possibility to perform calculations of much larger electronic systems than it is possible using many-particle wave functions. This is why DFT is very successful in calculating the structure of large molecules and chemical reactions. In 1998, Walter Kohn was awarded the Nobel prize in chemistry for this achievement [Kohn, 1999]. However, DFT can be used in the same way for the simulation of several hundred or thousand atoms under warm dense matter conditions.

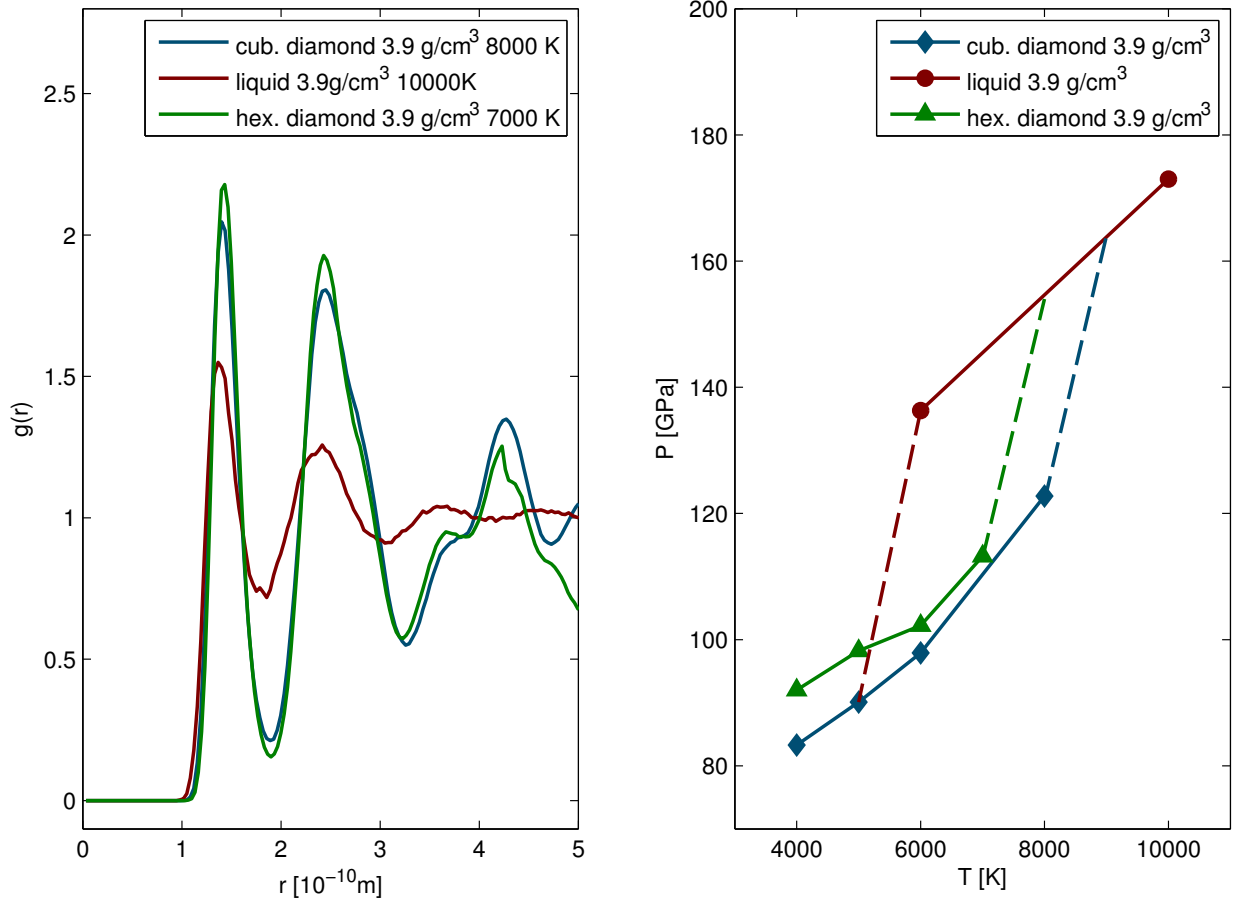


Figure 6.7: Results of the DFT-MD simulations. On the left: Exemplary pair correlation functions. On the right: pressure-temperature diagram.

6.2.2 Microscopic structure of shock-compressed graphite

The DFT-MD-method was applied for the calculation of the microscopic structure of shock-compressed graphite for conditions which could be achieved in the experiments. All presented DFT-MD simulations were performed by Jan Vorberger from the Centre for Fusion Space and Astrophysics of the University of Warwick using the *Vienna Ab-Initio Simulation Package (VASP)* [Kresse and Hafner, 1993, 1994; Kresse and Furthmüller, 1996]. A cubic sample volume with periodic boundary condition is filled with ~ 200 carbon atoms ordered according to the different investigated structures. For the whole simulation volume the temperature of interest is defined and is kept fixed during the simulation time. Further details concerning the special simulation setup for carbon in the WDM regime can be found in the supplemental material of [Pelka et al., 2010].

Simulated pair correlation functions for microscopic states which might be present inside the laser-driven shock are shown on the left side of figure 6.7. First, there is diamond which is compressed to 3.9 g/cm^3 and heated to 8000 K. The so-called layered diamond is a graphite structure which is compressed nearly exclusively on the c-axis to 3.9 g/cm^3 and heated to 7000 K. This structure represents hexagonal diamond (or lonsdaleite) in this pressure regime [Mundy et al., 2008]. The resulting pair correlation function is only slightly different from compressed usual cubic diamond on a first glance. The correlations of the liquid state at 3.9 g/cm^3 and 10000 K, however, show considerable deviations. The resulting radial distribution function is significantly smoother than those of the solid phases. The left diagram of figure 6.7 shows the performed simulation runs

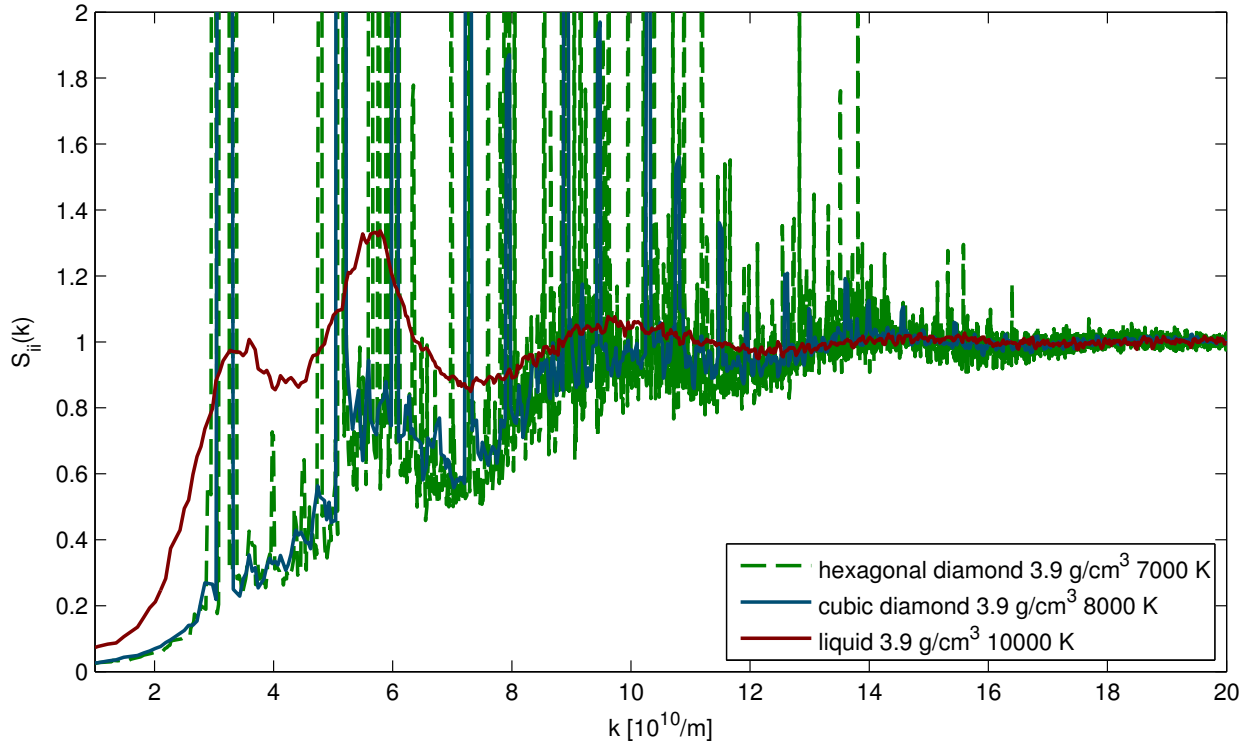


Figure 6.8: Structure factors which are obtained by Fourier transformation of the DFT-MD pair correlation function for cubic diamond, layered hexagonal diamond and liquid carbon.

in a pressure-temperature space. Obviously, there is some hysteresis: layered (hexagonal) diamond is stable up to ~ 7000 K before it transforms to the liquid phase, diamond is stable up to ~ 8000 K. Liquid carbon can be cooled down to ~ 6000 K before it transforms to cubic diamond. Comparing the density, temperature and pressure values to the hydrodynamic simulations indicates that all three phases are possible matter states which might be present inside the laser-driven shock.

The quantity which can be accessed by the X-ray scattering experiments is the static structure factor $S_{ii}(k)$. From the simulations, it can be calculated by Fourier transformation of the radial distribution function $g(r)$. The results of the three exemplary cases are shown in figure 6.8. For the two solid phases, there are a lot of remaining Bragg maxima resulting in spiked peaks. The height of these maxima is difficult to determine as the structure factor S_{ii} in dependence of the absolute value of the scattering vector \vec{k} is in principal only defined for an isotropic medium which is the contrary of a crystal. The graphs representing the crystal phases in figure 6.8 are generated by averaging over all possible orientations of a single crystal. For the polycrystalline samples which were applied in the experiments presented in this thesis, the maxima are expected to have much smaller values than for single crystals, depending on the size of the micro-crystallites [Pecharsky and Zavalij, 2003]. Therefore it may be not possible to distinguish between the Bragg maxima of a polycrystalline solid and the structure features of the liquid phase which are smoothed remnants of these peaks. Hence, the measurement of the phase transition should cover the region where no Bragg condition is implemented and the structure factor increases strongly for the liquid phase. The diagram in figure 6.8 clearly underlines that the region of k -values around 4 \AA^{-1} was very well chosen in the experiments to be able to distinguish between the liquid and solid state in this pressure regime.

7 Experimental results and discussion

In this chapter, the results of the two experimental campaigns at the *GSI Helmholtzzentrum für Schwerionenforschung*, performed in March/April 2011 and February/March 2012, are presented. The applied analysis methods are explained, the obtained data are discussed and compared to corresponding theoretical descriptions, especially the hydrodynamic and ab-initio simulations presented in the previous chapter.

7.1 Thermodynamic state in the shock wave

As described in chapter three, the thermodynamic quantities density, pressure and specific internal energy within a shock wave can be determined by measuring the shock velocity v_s and the particle velocity v_2 . Applying the doubling rule, v_2 can be substituted by $\frac{1}{2}v_{FS}$, where v_{FS} is the velocity of the free surface expansion due to the shock release. Using the Rankine-Hugoniot equations and assuming that the pressure of the shocked material is much larger than in the initial state ($P_2 \gg P_1$), the parameters density, pressure and specific internal energy within the shock wave are given by

$$\rho_2 = \frac{\rho_1 v_s}{v_s - v_2} \approx \frac{\rho_1 v_s}{v_s - \frac{1}{2}v_{FS}} \quad (7.1)$$

$$P_2 = \rho_1 v_s v_2 \approx \frac{1}{2} \rho_1 v_s v_{FS} \quad (7.2)$$

$$\epsilon_2 = \frac{1}{2} v_s v_2 \left(1 - \frac{v_s - v_2}{v_s} \right) \approx \frac{1}{4} v_s v_{FS} \left(1 - \frac{v_s - \frac{1}{2}v_{FS}}{v_s} \right). \quad (7.3)$$

Thus, knowing the initial density and measuring the two velocities, these quantities can easily be deduced. Unfortunately, the temperature is not directly accessible by the Rankine-Hugoniot equations as the increase of specific internal energy has to be splitted into thermal and potential energy due to compression (see chapter three). This ratio is strongly dependent on the microscopic structure and the atomic interaction potential. Therefore, a theoretically modeled equation of state is necessary to obtain the temperature from velocity measurements using the Rankine-Hugoniot equations.

Concerning the shock velocity, figure 7.1 shows two images which were recorded by the visible streak camera. The image on the left side shows a reference image in focus mode of the carbon target and the surrounding aluminum shielding where the entrance slit is completely open. The aluminum shielding prevents a direct line of sight onto the hot plume of the plasma corona which emits very bright light. The size of the entrance slit in streak mode is indicated by two horizontal lines. The image on the right side of figure 7.1 shows a swept image of the shock release from the target on the left. With the timing given by the Geola fiducial pulse on the right of the shock breakout, the shock transition time through the carbon sample can be determined. Due to the viewing angle of 45° to the target surface (see figures 5.2 and 5.4), the expansion of the shock breakout can be seen by the streak camera as well. However, the spatial resolution is not as good as the shadowgraphy diagnostics can offer for measuring the free surface velocity.

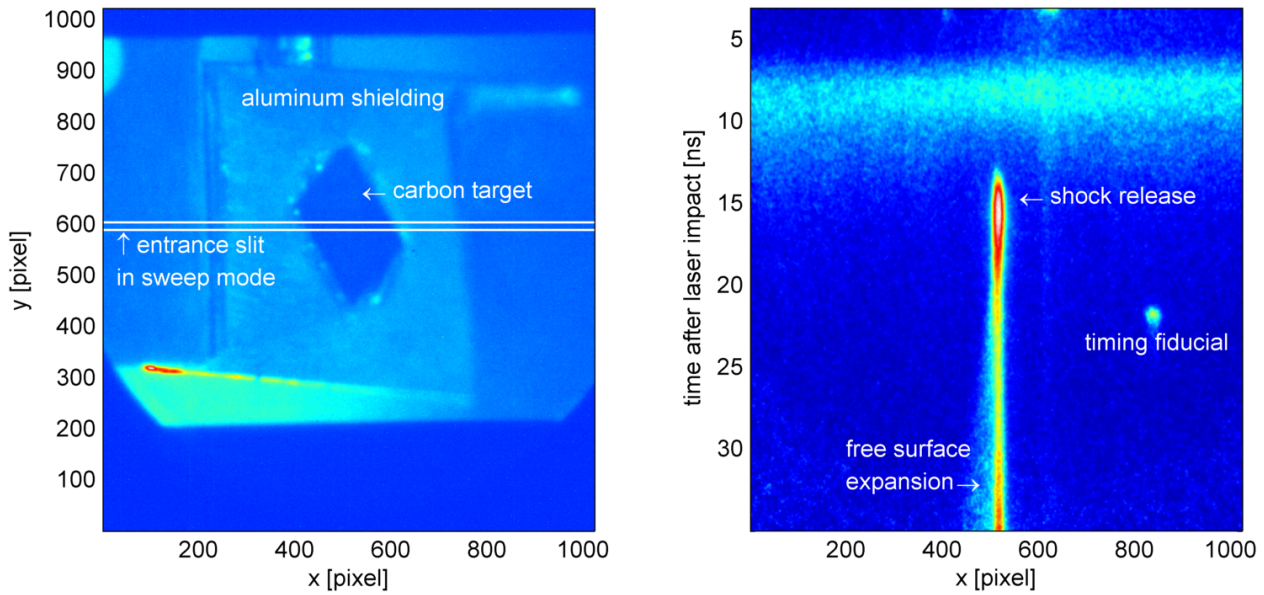


Figure 7.1: Measurement of the shock velocity with a visible streak camera. On the left: reference picture of the carbon target. On the right: streaked image of the area which is defined by the entrance slit.

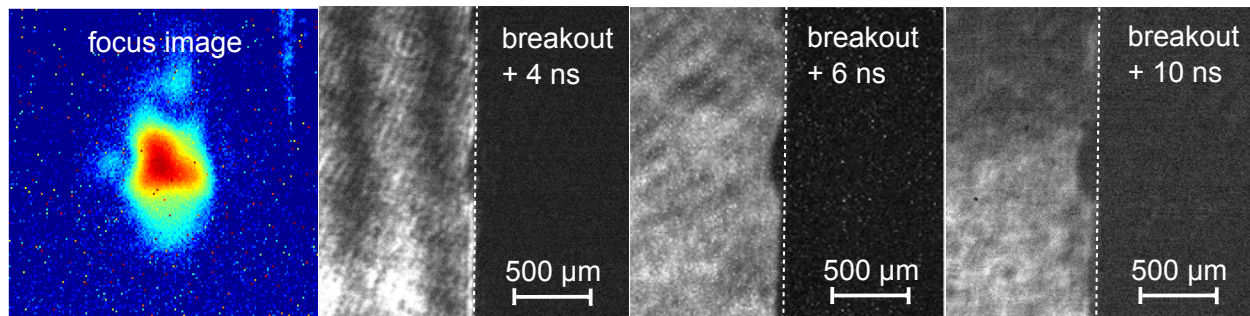


Figure 7.2: Measurement of the shock breakout speed with multi-frame shadowgraphy. These pictures show the expansion of the rear side of the same target at different times. The dashed line indicates the initial target surface.

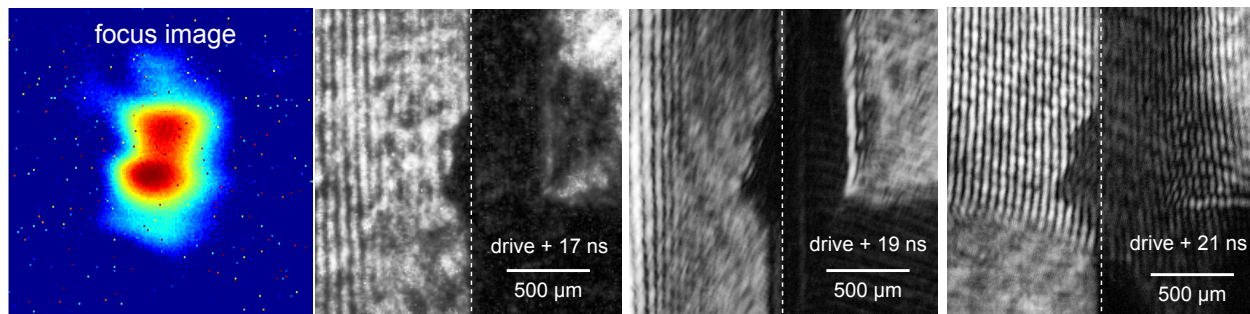


Figure 7.3: Example of a shock release on the target rear side of low quality caused by a laser focus with a double peak structure. The dashed line indicates the initial target surface.

In figure 7.2, an example of a shock release at the target rear side can be seen. The temporal resolution of the images is given by the Geola oscillator pulse length of 500 ps (see section 5.1.1). The spatial resolution of the pictures is $\sim 5 \mu\text{m}$, depending on the particular time frame. Following the different positions of the shock breakout relative to the initial target surface, the free surface velocity can be determined. Additionally, information about size and quality of the drive laser focal spot at full energy can be inferred from analyzing the shape of the release front. Figure 7.3 shows an example of a low quality focal spot with a double peak structure. This effect could then be corrected by re-adjusting the final focusing optics.

For a proper data analysis, the experimental conditions during the two campaigns have to be considered. In the experiments, the drive laser intensity varied from shot to shot (standard deviation $\sim 6\%$). Therefore it is important to know an approximate scaling of the velocities to the laser power. This can be obtained by using the derived scaling law for the ablation pressure (see equation (3.18)). Assuming a linear relation between shock velocity v_s and particle velocity v_2 for small variations (which is indeed a very good approximation [Zeldovic and Raizer, 1966]), a scaling relative to the drive laser intensity can be obtained:

$$v_s \propto v_2 \propto \sqrt{P_2} \propto I_L^{1/3}. \quad (7.4)$$

Comparing the two experimental campaigns, the properties of the drive laser were slightly different in pulse energy, pulse duration, focal spot size and focal spot profile. Therefore, it cannot be assumed that the conditions inside the shock wave were exactly the same in these two experiments. Thus, the following results concerning the velocity measurements are divided into two sections, one for each experimental campaign.

7.1.1 Experimental campaign March/April 2011

For the first experiment, the measured propagation of shock wave and shock release is shown in figure 7.4. Varying the thickness of the graphite samples, different stages of the shock propagation can be accessed. The shock transit times presented in figure 7.4 were obtained by the optical emission of the shock release which was monitored by a visible streak camera (see chapter five). The transition times clearly show a two-dimensional behavior of the shock wave: the shock propagation slows down for larger graphite thicknesses. This effect seems to be even larger than expected by the MULTI2D simulation. Therefore, a power function is fitted to the data and the shock velocity at a certain propagation time is then given by the local derivative of this curve. It is to mention that all values of the shock transit times in this diagram have already been scaled according to the fluctuating laser intensity to a standard laser energy of 62 J using equation (7.4). The standard deviation of laser energy has been 3.52 J for a mean value of 62.2 J. Therefore, the influence on shock and particle velocities is not too large due to the relatively insensitive $I_L^{1/3}$ scaling. However, the accuracy of the fit curve is significantly improved by this method.

The propagation of the shock release at the target rear side is shown in the right diagram of figure 7.4. For a clear view, the timescale in this image is not connected to the drive laser impact but to the shadowgraphy frame. The time +2 ns corresponds to the first shadowgraphy frame, +4 ns to the second, and so on. The larger errorbars in the second frame are due to less magnification of the imaging system in this frame. The position values shown in this diagram are already corrected for the fluctuating laser intensity in the same way as the shock transit times. Applying a linear fit to the data obtained by the multi-frame shadowgraphy, the expansion velocities v_{FS} are given by the slope of the fit curves. In principal, the shock transit times can also be deduced from the shadowgraphy data by extrapolating the linear fit to the start point of the shock release. This

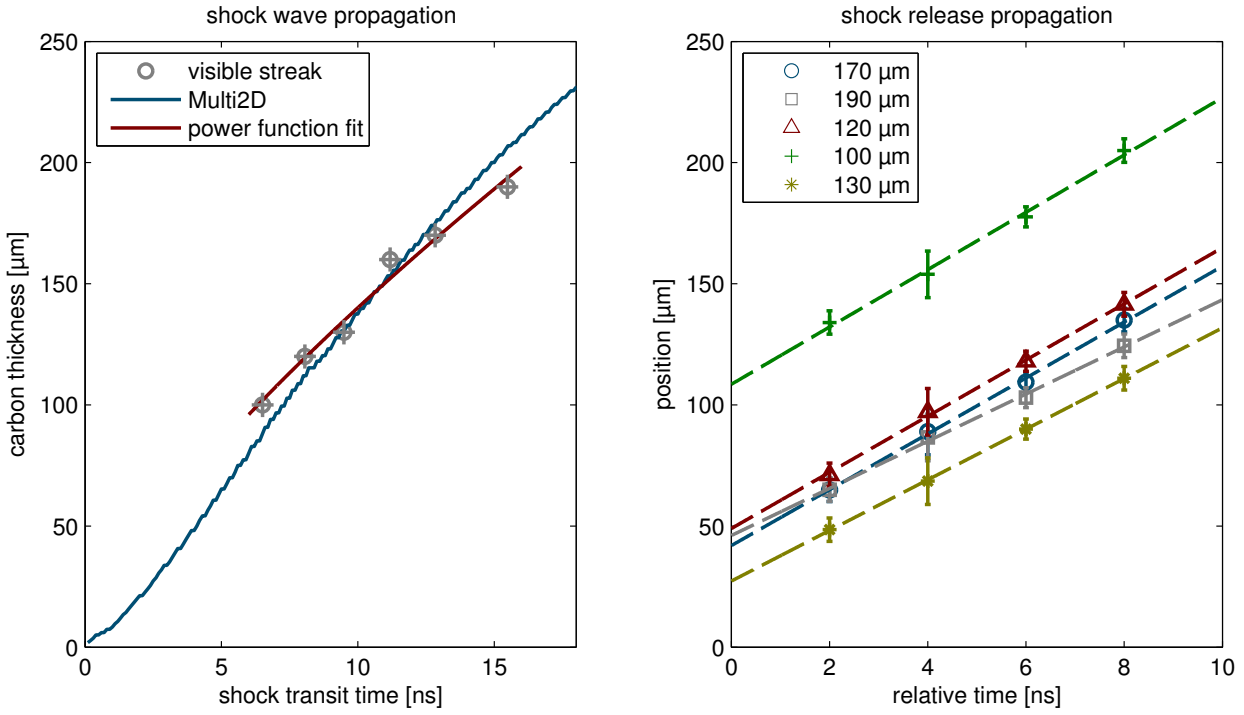


Figure 7.4: On the left: Shock breakout times for different target thicknesses measured by the visible streak camera compared to the propagation simulated by MULTI2D and a power function fit curve ($d = 25.48(t_{\text{trans}}/\text{ns})^{0.7402} \mu\text{m}$). On the right: Propagation of the shock release from the target rear side measured by the multi-frame shadowgraphy. Both diagrams show only data of the first experimental campaign.

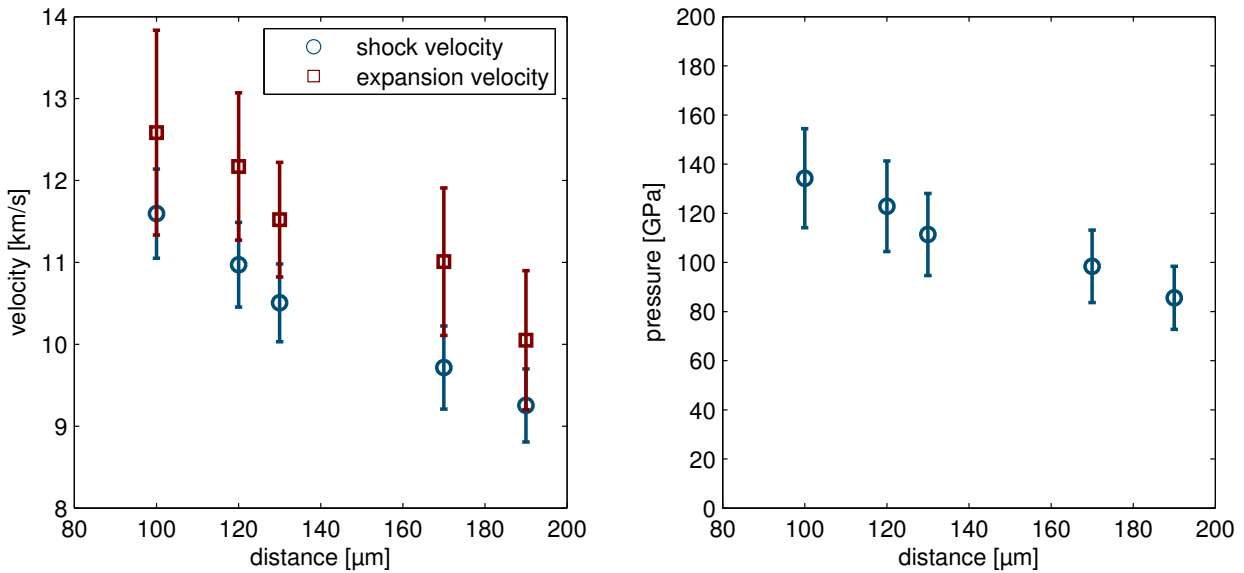


Figure 7.5: On the left: measured shock velocity and velocity of the free surface expansion for different target thicknesses in the first experimental campaign. On the right: Resulting pressures applying the Rankine-Hugoniot equations and the doubling rule.

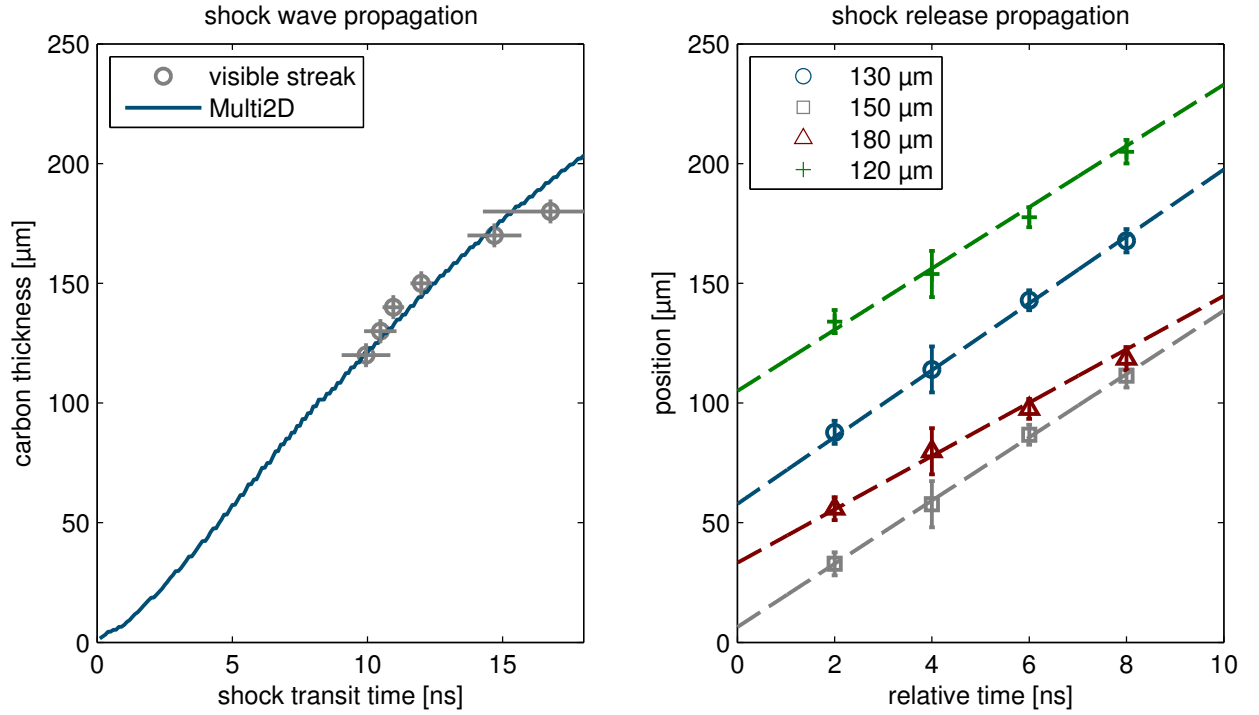


Figure 7.6: On the left: Shock breakout times for different target thicknesses measured by the visible streak camera compared to the propagation simulated by MULTI2D. On the right: Propagation of the shock release from the target rear side measured by the multi-frame shadowgraphy. Both diagrams show only data of the second experimental campaign.

method, however leads to results which are by far not as accurate as the measurements obtained by the visible streak camera.

A diagram of the resulting shock and free surface velocities for this experimental campaign is shown on the left side of figure 7.5. The decrease of these velocities for larger target thicknesses is clearly visible which again underlines the presence of a not perfectly planar shock drive. Using the Rankine-Hugoniot equations in combination with the doubling rule, the thermodynamic parameters can be obtained from the two velocities for completely shocked samples of varying thickness. This is possible despite the slightly two-dimensional behavior of the shock wave because the one-dimensional Rankine-Hugoniot equations have still to be true close to the shock front. The diagram on the right side of figure 7.5 shows the pressures calculated by this method. After a propagation distance of 90 μm, the pressure within the shock wave is (134 ± 19) GPa whereas (86 ± 11) GPa are achieved at 190 μm. The latter was the chosen target thickness for the X-ray scattering experiments in this campaign and therefore of special interest. The densities which are measured via this method are relatively constant at (3.9 ± 0.3) g/cm³ for the different target thicknesses. This is not surprising as the Hugoniot curve in a pressure-density diagram is very steep in this regime (see figure 7.8).

7.1.2 Experimental campaign February/March 2012

A different focus profile and slightly larger pulse durations of the drive laser during the second experimental campaign requires the laser-driven shock to be characterized again in detail. The shock transit times for different target thicknesses are shown on the left side of figure 7.6. Some of the errorbars in this diagram are larger compared to the data obtained in the first campaign due

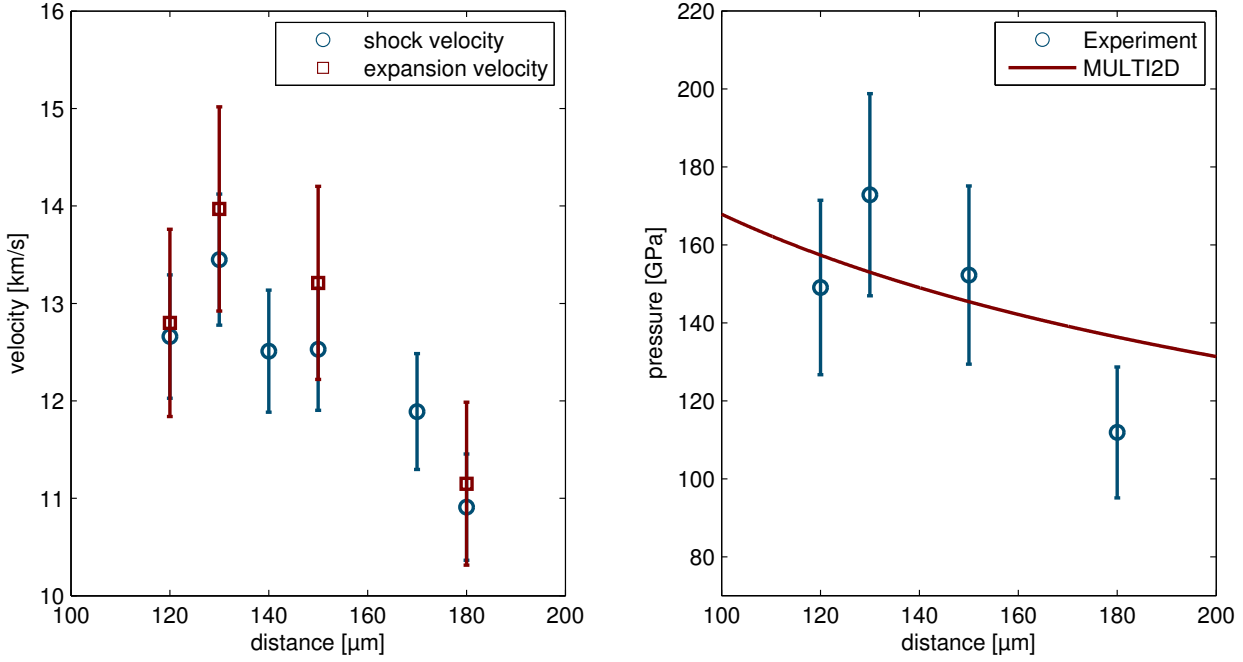


Figure 7.7: On the left: measured shock velocity and velocity of the free surface expansion for different target thicknesses in the second experimental campaign. On the right: Resulting pressures applying the Rankine-Hugoniot equations and the doubling rule compared with the simulation results of MULTI2D.

to a low signal level on the visible streak camera. Nevertheless, the shock characteristics can be deduced and in this experiment the propagation seems to be more planar than in the previous experiment. For example, the shock motion now is very well modeled by the MULTI2D simulations. Most probably, there has been an intensity spike in the focus profile during the first experimental campaign which could be avoided in the second campaign.

Like in the previous experiment, the free surface propagation is measured via multi-frame shadowgraphy. The resulting positions of the shock release are shown on the right side of figure 7.6 and again suggest a linear motion within the errorbars. All values drawn in the two diagrams of figure 7.6 are scaled for the varying laser intensity. The fluctuations in this campaign lead to a standard deviation of 3.77 J for a mean value of 63.9 J

The deduced shock and free surface velocities are shown in the left diagram of figure 7.7. Again, there is a decrease for larger target thicknesses due to two-dimensional effects. However, these are not as distinct as monitored in the first experimental campaign. Another difference is that the measured velocities are slightly larger in comparison to the previous experiment. This is due to the smaller focal spot which resulted in higher drive laser intensities despite the marginally increased pulse duration. Thus, the pressures inside the shocked material which are shown in the right diagram of figure 7.7 are also larger compared to the measurements of the first campaign. As the shock transit times very well follow the MULTI2D calculations, it is reasonable to compare the pressures to the simulation results as well. Again, there is suitable agreement with the simulations, as depicted in the diagram. The densities obtained by the velocity measurements are $(4.0 \pm 0.3) \text{ g/cm}^3$ and thus comparable to the first campaign.

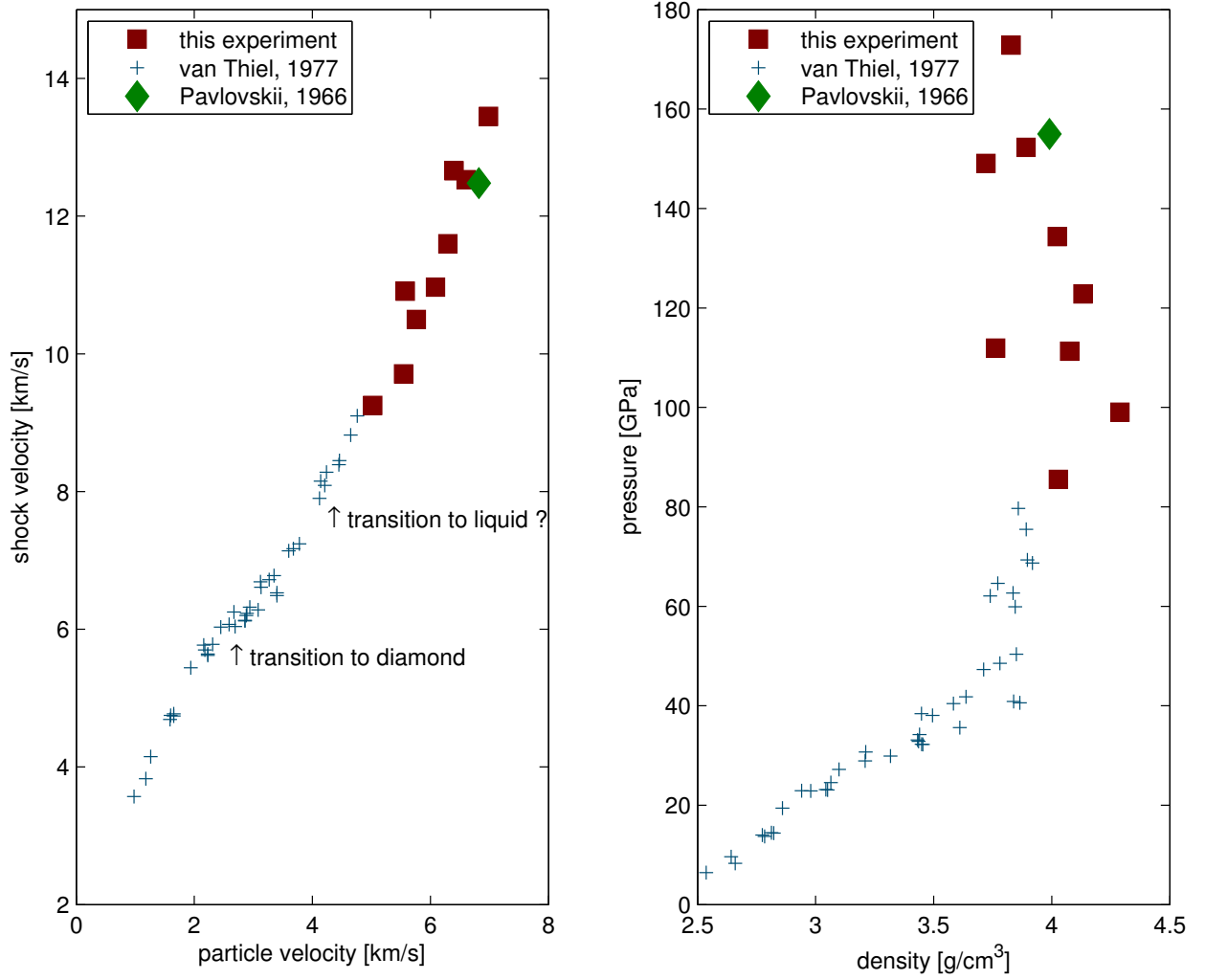


Figure 7.8: Comparison of the obtained Hugoniot data with measurements on porous graphite with similar initial density published in [van Thiel, 1977] and [Pavlovskii and Drakin, 1966].

7.1.3 Hugoniot data

The velocities which were obtained by the visible streak camera and the multi-frame shadowgraphy can be drawn in a diagram of particle and shock velocity. Hereby, the doubling rule has to be applied to calculate v_2 . This is done in figure 7.8 where also very precise measurements using porous graphite of similar initial density by [van Thiel, 1977] are shown. This high quality data was obtained by the Lawrence Livermore National Laboratory using flyer plates which were driven by explosives and gas guns. In the velocity diagram there is an obvious change in slope at a particle velocity of $v_2 \approx 2.5$ km/s. This value corresponds to a pressure of ~ 20 GPa and clearly shows the onset of the transition to diamond [Gust, 1980].

Going to larger velocity values, there might be a slight additional change in slope at $v_2 \approx 4.2$ km/s. This feature is very small, though, and could just be a random deviation. However, measurements on porous graphite with slightly lower and larger density which are also published in [van Thiel, 1977] show a similar behavior exactly at the same value of v_2 . Additionally, this small feature can also be found in other high precision measurements performed by the Los Alamos National

Laboratory which used the same type of porous graphite [Marsh, 1980]. The combination of all these experiments might be a hint (definitely not a proof) that the transition to the liquid for this type of graphite starts at $v_2 \approx 4.2$ km/s.

The measured velocities of the experiments presented in this thesis well continue the literature data at the upper end in the velocity and the pressure-density diagrams. The latter shows why velocity measurements have to be very precise to gain accurate information about thermodynamic parameters within a shock wave: a small data deviation of velocities can still result in large variations in the pressure-density diagram. However, the Hugoniot data which were obtained by the experiments of this thesis are very valuable because they fall into a region which is nearly uncovered by experiments so far. In fact, nearly all published Hugoniot measurements of porous graphite with initial density close to 1.84 g/cm^3 finish at ~ 100 GPa. This seemed to be the limit of the applied two-staged gas guns in those times [Gust, 1980]. There is only one data point from high explosives by [Pavlovskii and Drakin, 1966] ($\rho_1 = 1.82 \text{ g/cm}^3$, $v_2 = 6.82 \text{ km/s}$, $v_s = 12.48 \text{ km/s}$, $\rho_2 = 4.0 \text{ g/cm}^3$, $P_2 = 155 \text{ GPa}$) which directly falls into the the region accessed by the experiments in the framework of this thesis. These values fit very well to the presented measurements but are, however, given without any error estimation. Nevertheless, this data point, which could directly access v_2 , supports the assumption that the doubling rule is still valid in this pressure regime. In addition, the Hugoniot data which were obtained in the framework of this thesis are shown in numbers together with an error estimation in the following table.

ρ_1 [g/cm ³]	v_2 [km/s]	v_s [km/s]	ρ_2 [g/cm ³]	P_2 [GPa]
1.84	5.0±0.4	9.3±0.5	4.0±0.3	86±11
1.84	5.5±0.4	9.7±0.5	4.3±0.3	99±12
1.84	5.8±0.4	10.5±0.5	4.1±0.3	111±15
1.84	5.6±0.4	10.9±0.5	3.7±0.3	112±15
1.84	6.1±0.5	11.0±0.6	4.1±0.3	123±17
1.84	6.3±0.5	11.6±0.6	4.0±0.3	134±19
1.84	6.4±0.5	12.7±0.6	3.7±0.3	149±22
1.84	6.6±0.5	12.5±0.6	3.9±0.3	152±22
1.84	7.0±0.5	13.5±0.7	3.8±0.3	173±25

For a clearer view, the corresponding errors are not shown in figure 7.8. Extrapolating the literature data suggests, that the densities should sit in a window between 3.7 g/cm^3 and 4.1 g/cm^3 for the regime which was accessed by the experiments presented in this thesis. This is in very good agreement with the hydrodynamic simulations using the SESAME equation of state. The PROPACEOS tables result in too low densities. These Hugoniot measurements in combination with the DFT-MD simulations show that conditions were reached inside the laser-driven shocks where three different carbon phases are in principal existent: cubic diamond, hexagonal diamond and liquid carbon. Which state is really present had to be determined by X-ray scattering.

7.2 X-ray generation

In this section, the generated X-ray radiation is discussed. This includes first of all a study using the time-resolved shadowgraphy to ensure that the applied targets work properly in the experiments. After that, the spectral composition of the applied line transition is investigated. Comparing the radiation spectrum to the collisional-radiative codes PrismSpect [MacFarlane et al., 2003] and FLYCHK [Chung et al., 2005] allows for estimations of the source size and the plasma parameters where the Ti-He- α radiation was generated. Additionally, the conversion efficiency of laser pulse energy to the applied X-ray line transition is discussed. This leads to an estimation in what ex-

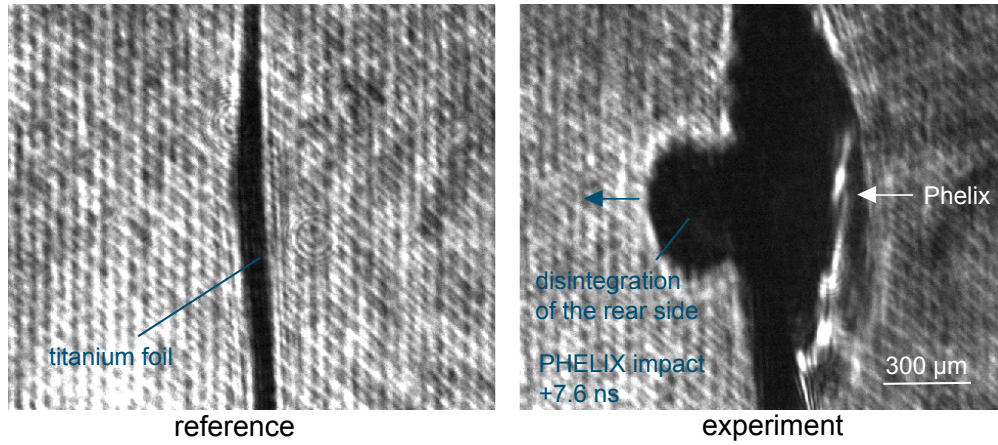


Figure 7.9: Shadowgraphy images for the investigation of the backlighter foil disintegration. Major disintegration of the rear side only starts after all the laser energy has been delivered to the titanium foil.

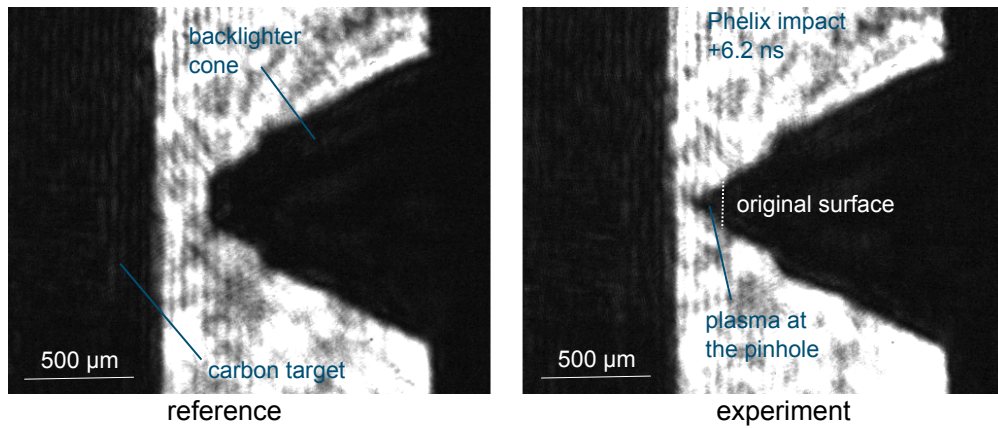


Figure 7.10: Shadowgraphy images of the backlighter cone pinhole disintegration. The pinhole is not blocked for the X-rays during the major laser-matter interaction time.

tend the carbon samples can already be heated by the probe-radiation. Finally, the angular X-ray distribution which is generated by the pinhole of the backlighter cone is calculated.

7.2.1 Shadowgraphy images

In addition to the shock breakout characterization, the multi-frame shadowgraphy instrument was also a very useful diagnostics for the backlighter drive. Using the shadowgraphy it could for example be ensured that the drive laser is not able to burn a hole into the titanium foil during the laser-matter interaction time. This was a major problem in a previous experiment where thin plastic foils were applied as backlighter targets. As a result, the X-ray producing plasma could expand to the scattering target and the source radiation was directly visible for the scattering spectrometers due to the disintegration of the backlighter during the laser interaction time. This scenario could be excluded in the experiments presented in this thesis by analyzing the shadowgraphy images (see fig 7.9).

Another application of the shadowgraphy is examining a possible disintegration of the gold cone, especially the pinhole. This is not an unrealistic scenario as a big fraction of the laser energy is converted to low energy X-rays at the titanium foil. This radiation is partially transmitted through the

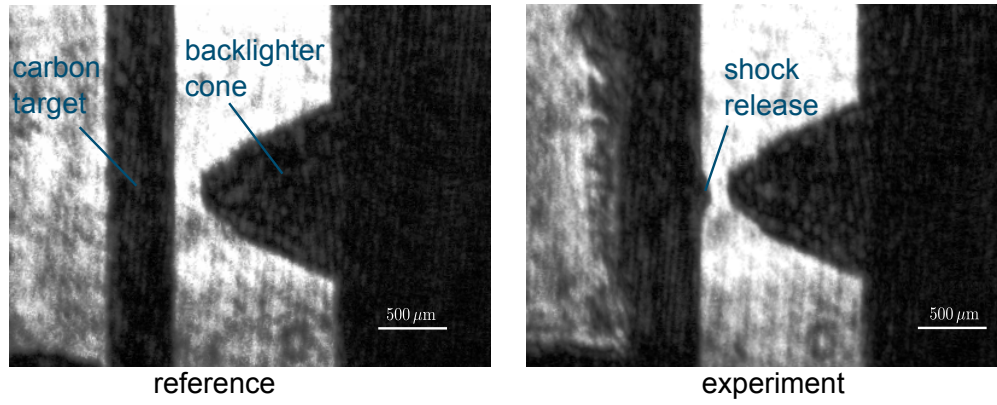


Figure 7.11: Shadowgraphy images of the shock release in front of the backlighter cone pinhole. This ensures that the shock-driving laser is adjusted correctly relative to the backlighter setup.

backlighter foil and the small cone with the pinhole then acts as hohlraum cavity which increases the energy density of the radiation field. If the gold walls at the pinhole are heated enough that the pinhole will close during the laser-interaction time a substantial part of the X-rays for probing the carbon sample would be blocked. However, the shadowgraphy monitored visible effects connected to the disintegration of the pinhole like in figure 7.10 not until 3 ns after the impact of the *PHELIX* pulse.

Finally, the shadowgraphy could also be used to reassure that the laser responsible for the shock drive was aligned correctly in respect to the opening in the backlighter conus. For example, figure 7.11 shows the center of a shock release directly in front of the backlighter cone. Thus, it can be deduced that is really the shocked part of the carbon sample which is probed by the X-rays.

7.2.2 Spectral features of the source radiation and resulting plasma parameters

An example of a titanium helium- α spectrum which was measured by the source spectrometer during the experiments is shown in figure 7.12. The triple peak structure of the observed line can be explained as follows: the main transition ($1s2p \rightarrow 1s^2 1P \rightarrow 1S$) at 4.74963 keV is the strongest line followed by the so-called intercombination line ($1s2p \rightarrow 1s^2 3P \rightarrow 1S$) at 4.72693 keV. The third peak at roughly 4.710 keV is a composition of satellite lines caused by lithium-like ions ($1s2p^2 \rightarrow 1s^2 2p$ with all possible spin couplings of excited and ground state). These line features can be used to estimate the plasma parameters temperature and density of the source plasma. The intensity of the intercombination line in comparison to the main transition is strongly density-dependent [Kunze, 1981]. Furthermore, the presence of the satellite peaks strongly varies with temperature. Codes which solve the collisional radiative rate equations are able to generate synthetic spectra which can be fitted to the experimentally obtained data.

Another parameter which has to be included to compare the monitored spectra to PrismSpect and FLYCHK, is the line width. In the experiment this is mainly given by the instrumental broadening of the detector and the finite source size. To compare the spectral intensity measured in the experiment $I_{\text{exp}}(E)$ with the calculated spectra $I_{\text{CR-code}}(E)$, the latter has to be convoluted with the spectral broadening due to the reflection at the HOPG crystal, $g_{\text{HOPG}}(E)$, and detection at the image plate, $g_{\text{IP}}(E)$:

$$I_{\text{exp}}(E) = I_{\text{CR-code}}(E) * g_{\text{HOPG}}(E) * g_{\text{IP}}(E). \quad (7.5)$$

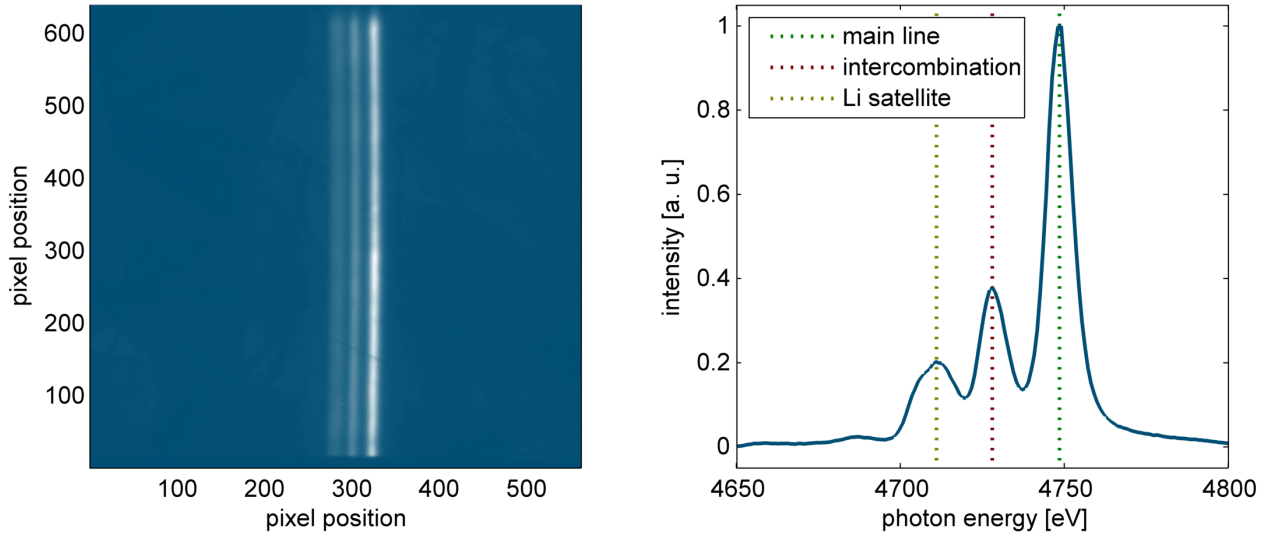


Figure 7.12: On the left: scanner image of an exposed source spectrometer image plate. On the right: energy-calibrated horizontal lineout of the image plate, averaged over 200 pixel lines.

Here, $f(E) * g(E)$ represents the convolution of the spectral functions $f(E)$ and $g(E)$ which is defined by

$$f(E) * g(E) = \int_{-\infty}^{+\infty} f(E)g(E - E')dE'. \quad (7.6)$$

The influence of the source size is contained in the spectral broadening of the HOPG reflection. The FWHM of the profile $g_{\text{HOPG}}(E)$ is given by

$$\Delta E = c_{\text{spec}}d_{\text{source}}, \quad (7.7)$$

where d_{source} is the X-ray source size and c_{spec} is a constant which depends on the spectrometer geometry and the rocking curve of the applied HOPG crystal [Schollmeier, 2004]. In the experiments presented in this thesis the value of this constant is $c_{\text{spec}}=75 \text{ eV/mm}$ and the profile $g_{\text{HOPG}}(E)$ is assumed to be Gaussian.

The broadening caused by the image plates has a Lorentz profile for this IP type [Seely et al., 2008]:

$$g_{\text{IP}}(E) = \frac{1}{2\pi} \frac{\Gamma}{E^2 + \Gamma^2/4}. \quad (7.8)$$

The FWHM Γ of this profile is energy dependent and can be determined by the derivative of a sharp edge imaged by the IP using the desired photon energy. For the applied AGFA MM 3.0 image plates in combination with the FUJI FLA-7000 scanner, the value is measured to be $\Gamma=4.6 \text{ eV}$ for a photon energy of 4.75 keV.

Using these profiles, the simulated spectra can be compared to the experiments using three free parameters: electron temperature, ion density and X-ray source size. Figure 7.13 shows an example of an optimization calculation using the CR-code PrismSpect where these three parameters were varied. It is clearly visible that the observed spectrum can be very well modeled by this code. Additionally, the color plot on the right side of figure 7.13 shows that this result represents a stable minimum in temperature-density space for the determined source size of $71 \mu\text{m}$. This value fits

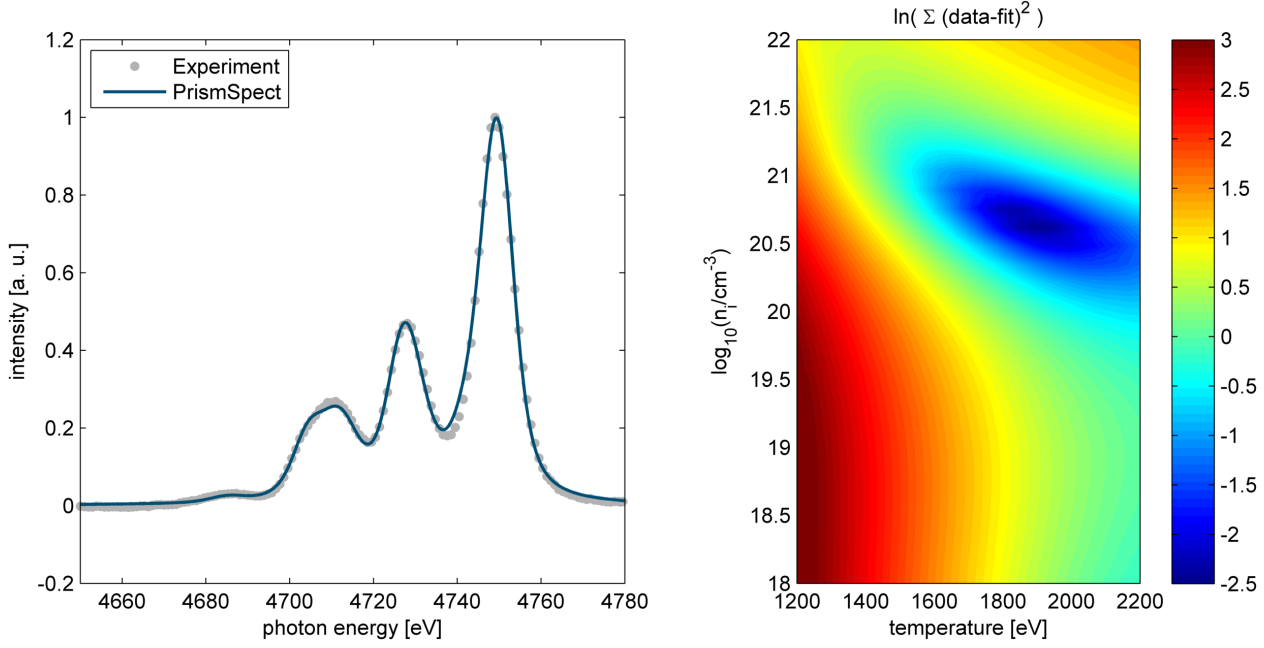


Figure 7.13: On the left: fit of the source spectrum using the CR-code PrismSpect. The resulting parameters are $T_e=1880$ eV, $n_i=4.0 \times 10^{20}$ cm $^{-3}$ and $d_{\text{source}}=71$ μm . On the right: color plot of the fit quality in the density-temperature space where the source size is kept fixed at the optimum value. The PrismSpect fit gives a very stable minimum and very good agreement with the measured spectrum.

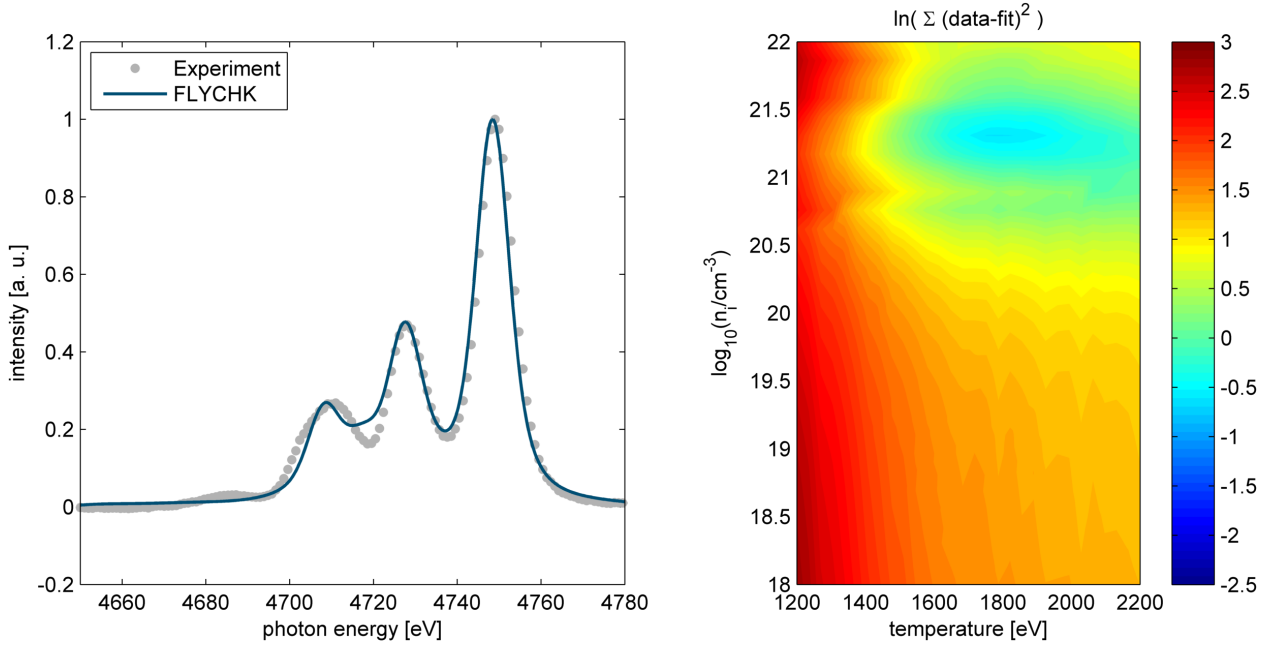


Figure 7.14: On the left: fit of the source spectrum using the CR-code FLYCHK. The resulting parameters are $T_e=1770$ eV, $n_i=2.0 \times 10^{21}$ cm $^{-3}$ and $d_{\text{source}}=78$ μm . On the right: color plot of the fit quality in the density-temperature space where the source size is kept fixed at the optimum value. Obviously, the stability and quality of the FLYCHK fit is not as good as the PrismSpect calculations.

very well to the typical focal spot images of the *PHELIX* laser at Z6 [Schumacher, 2012]. The obtained plasma parameters $T_e=1880$ eV and $n_i=4.0\times10^{20}\text{ cm}^{-3}$ are also reasonable for conditions of efficient titanium helium- α production.

As seen in figure 7.14, the source spectrum reproduction with FLYCHK is not as good as with PrismSpect. This is mainly due to the fact that the modeled satellite lines do not perfectly match the measured spectrum. Additionally, the resulting ion density of $n_i=2.0\times10^{21}\text{ cm}^{-3}$ which corresponds to an electron density of $n_e=4.0\times10^{22}\text{ cm}^{-3}$ seems a bit overestimated. This value is already close to solid density but the generation of thermal high energy X-rays is most efficient closely behind the critical density. Furthermore, the minimum in temperature-density space for the FLYCHK fits is not as stable and as it can be obtained by the PrismSpect calculations.

It is to mention that the exemplarily analyzed source spectrum is taken from the data which were obtained in the second experimental campaign. In fact, the source characteristics of the first campaign are only slightly different. PrismSpect fits a little lower temperatures ($T \approx 1750$ eV), similar ion densities ($n_i \approx 3.7\times10^{20}\text{ cm}^{-3}$) and a larger source size ($\sim 120\text{ }\mu\text{m}$). FLYCHK gives the same trend: $T \approx 1650$ eV, $n_i \approx 2.0\times10^{21}\text{ cm}^{-3}$ and a source size of $\sim 125\text{ }\mu\text{m}$. These results are reasonable as a larger focal spot results in less intensity to heat the backlighter plasma. Thus, this is an indication that the focal spot for the X-ray generation during the first campaign was of slightly lower quality compared to the second campaign.

This small study shows very well the power of the spectral analysis for the characterization and optimization of thermal X-ray backlighter radiation. Especially PrismSpect obtains very realistic results for the Ti-He- α line transition.

7.2.3 Conversion efficiency of laser energy to X-rays

As the presented experiments were the first which used the *PHELIX* laser for an X-ray scattering experiment, the conversion efficiency η_L from laser energy E_L to X-rays is a very interesting quantity. It is defined by

$$\eta_L = \frac{E_X}{E_L}, \quad (7.9)$$

where E_X is the total energy of all X-ray photons produced by the applied line transition, in this case the titanium helium- α transition. This value can be accessed by an absolutely calibrated spectrometer with efficiency η_{spec} . For the applied flat HOPG crystal mounted in mosaic focusing geometry, this efficiency is given by

$$\eta_{\text{spec}} = \frac{w\tau_f R_{\text{int}}}{8\pi d}, \quad (7.10)$$

where w is the signal length on the detector in non-dispersive direction, τ_f the accumulated transmission of all filters inside the spectrometer, R_{int} the integrated HOPG-reflectivity for the given photon energy and d the distance from the X-ray source to the HOPG crystal [Kugland et al., 2009]. For the source spectrometer, the values for the experiments in the framework of this thesis were as follows: $w=28$ mm, $\tau_f=2.6\%$, $R_{\text{int}}=3$ mrad and $d=247$ mm. This results in a spectrometer efficiency of $\eta_{\text{spec}} \approx 3.6\times10^{-7}$. Hereby, the most uncertain quantity is R_{int} which was not measured explicitly for this crystal. The typical integrated reflectivities for HOPG crystals at the photon energy 4.75 keV vary from 1 to 4 mrad. The deviations are caused by the mosaicity which is often differing for every single crystal. However, this estimation is just aimed to find the rough order of magnitude for the conversion efficiency. Therefore, a variation of $\sim 50\%$ is still acceptable

and a typical error statement for this kind of measurements [Glenzer and Redmer, 2009].

The total energy detected by the image plates E_{spec} is given by multiplying the integrated PSL value I_{IP} with the IP response η_{IP} (which is typically specified in PSL/photon) and the photon energy E_{ph} . Thus, the final expression for the total X-ray energy which was emitted in the whole solid angle of 4π is then:

$$E_X = \frac{E_{\text{spec}}}{\eta_{\text{spec}}} = \frac{8\pi d}{w\tau_F R_{\text{int}}} E_{ph} \eta_{IP} I_{IP}. \quad (7.11)$$

There is an existing calibration for the applied image plate type MM 3.0 with top coating for 5.8 keV giving $\eta_{IP}=1.3$ mPSL/photon [Philipp, 2011]. In this energy regime, the IP response is approximately linear [Meadowcroft et al., 2008]. Therefore, for a photon energy of 4.75 keV, an IP response of ~ 1.1 mPSL/photon can be assumed. Applying equation (7.11) gives a mean laser to X-ray conversion efficiency of $\eta_L \approx 4.8 \times 10^{-3}$ with a standard deviation of 2×10^{-3} for the experiments presented in this thesis [Roth, 2012]. This is a relatively high value in comparison to other 527 nm laser systems where such experiments have been performed and conversion efficiencies from 1×10^{-3} to 3×10^{-3} have been measured [Glenzer and Redmer, 2009].

7.2.4 Estimated heating of the carbon sample by probe radiation X-rays

Knowing the values of X-ray conversion efficiency η_L , it is possible to estimate the energy that is deposited by the probe radiation within the carbon sample. Fortunately, only the 4.75 keV radiation is able to transmit through the titanium backlighter foil efficiently. More energetic Lyman- α photons are not produced in high numbers and important lines of lower energy only exist in the region around 1 keV. This photon energy is not high enough to transmit effectively through the titanium foils. The absorbed X-ray energy from the surface to a penetration depth x_1 is given by

$$E_{\text{abs}}(x_1) = E_L \eta_L \tau_{Ti} \frac{\Delta\Omega_{\text{sample}}}{4\pi} \frac{1}{l_0} \int_0^{x_1} e^{-x/l_0} dx, \quad (7.12)$$

where $\Delta\Omega_{\text{sample}}$ is the solid angle of radiation which can reach the sample. The absorption length l_0 for the photon energy 4.75 keV inside graphite of density 1.84 g/cm^3 is $245 \text{ }\mu\text{m}$. τ_{Ti} accounts for transmission losses of the titanium foil for its own helium- α radiation. The temperature increase of the cold sample is then given by dividing the absorbed energy by the heat capacity for constant volume c_V and the mass of the heated part of the carbon sample m_{sample} :

$$\Delta T = \frac{E_{\text{abs}}}{c_V m_{\text{sample}}}. \quad (7.13)$$

The values in the following table are calculated by two assumptions: one exploiting the error margins for maximum possible heating and one using the mean values for a most realistic scenario. The values for $x_1=10 \text{ }\mu\text{m}$, $m_{\text{sample}}=1.3 \times 10^{-9} \text{ kg}$ and $c_V=8000 \text{ J/(kg K)}$ are fixed.

	E_L [J]	η_L	τ_{Ti}	ΔT [K]
maximum heating	200	1×10^{-2}	0.9	1333
realistic heating	150	5×10^{-3}	0.7	389

As the expected temperatures inside the shock wave are 8000 K to 10000 K (compare chapter six), the more realistic scenario would add some but not very significant heating. Considering the maximum approximation, however, the temperature increase would not be negligible. It is

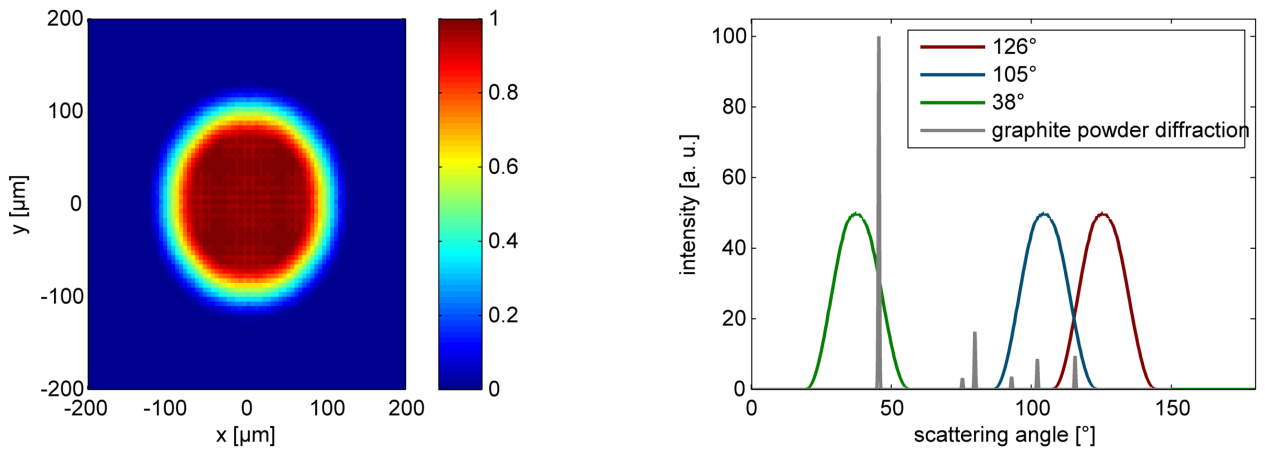


Figure 7.15: Results of the raytracing routine for calculating the angular distribution of the X-rays. On the left: a virtual screen at the position of the graphite sample illustrates the intensity distribution which is generated by the pinhole. On the right: resulting distributions of scattering angles which are recorded by the HOPG spectrometers in comparison the Bragg-reflections from polycrystalline graphite.

relatively unlikely but these assumptions could give an explanation if effects of higher temperature are observed by the scattering experiment. Additionally, it is to mention that here only the first 10 μm have been considered and the heating inside the graphite sample decreases exponentially following the absorption curve. However, these first layers are also the most relevant for the scattering signal (see section. 7.3).

7.2.5 Angular distribution of the X-rays

Another very important quantity for the analysis of the scattering spectra is the distribution of the scattering angles which is seen by the X-rays spectrometers for the applied backlighter target construction. Hereby, the X-ray source with its size and intensity profile as well as the gold pinhole with its diameter and distance to the X-ray source have to be considered. This was realized by implementing a three-dimensional raytracing routine where the source radiation is monitored by a virtual screen at the graphite position behind the gold pinhole. Then the rays reaching the screen are send towards a virtual HOPG crystal and the resulting scattering angles from the screen are collected to form a distribution function.

The results of this raytracing scheme can be seen in figure 7.15. The virtual screen at the graphite position is shown on the left. The angle distributions for the three scattering spectrometers which were mounted in the second campaign together with the powder diffraction spectrum of graphite are shown on the right. The Bragg maxima and their relative intensity were calculated by the commercial powder diffraction application *CrystalDiffra* [CrystalMaker Software, 2012].

The angular distributions emphasize that the chosen scattering angles are a compromise of technical feasibility and an absolutely ideal setup. For example, the 38° spectrometer was aimed to observe the decrease of the Bragg maxima at 45° but the target chamber dimensions did not allow for the setup of the spectrometer exactly at this angle. Furthermore, the 126° spectrometer should ideally not cover a Bragg maximum. Yet, its angle distribution slightly matches a Bragg condition at 115.5°. Therefore, significant elastic scattering can be expected for cold samples. A larger scattering angle was not feasible due to the target design (the spectrometer has to be shielded from the X-ray source) and additionally, the target chamber dimensions were not allowing for the im-

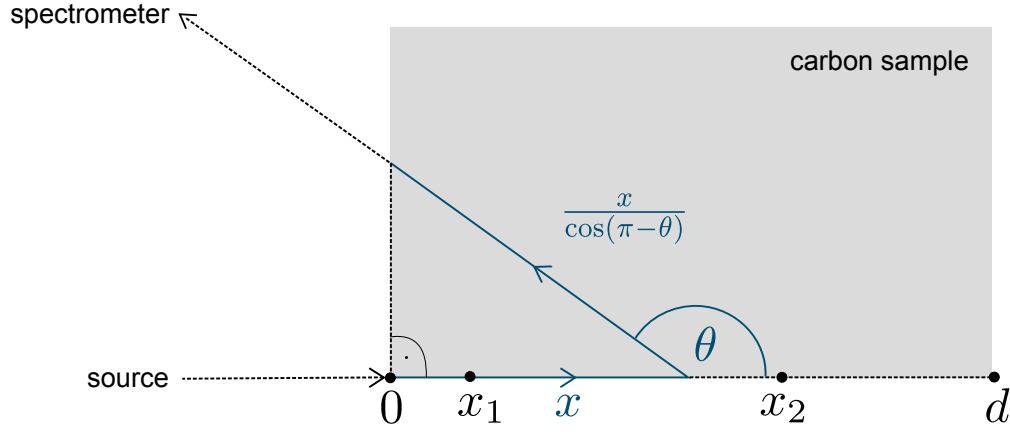


Figure 7.16: Sketch of one exemplary path of a scattered X-ray photon.

plementation of a larger scattering angle for this spectrometer as well. A smaller pinhole was not practicable as a sufficient reduction of its diameter to totally prevent a contribution of the Bragg maximum would have resulted in about a factor of ten less X-rays at the sample. This would drastically reduce the quality of the scattering spectra. However, the experience of previous experiments [Pelka, 2010] gave confidence that slightly covering a small Bragg maximum would not be enough to produce more elastic scattering from cold graphite than signals of shocked liquid graphite would show. This assumption has proven to be true within the experiments presented in this thesis (see section 7.5).

7.3 Absorption characteristics and influence of the shock-driving laser plasma

For the design of experiments and the analysis of obtained scattering spectra, it is important to know the contributions of the different target regions to the scattering signal. Figure 7.16 shows a sketch for the pathway of a backscattered photon. For the contribution of a penetration depth x_2 , it is important to consider the way into the sample as well as the way out of it. The total absorbed intensity of the initial incident radiation with intensity I_0 following this way in and out is given by

$$I_{\text{abs}}(x_1, x_2) = \frac{I_0}{l_0} \left(1 + \frac{1}{\cos(\pi - \theta)} \right) \int_{x_1}^{x_2} e^{-\left(1 + \frac{1}{\cos(\pi - \theta)}\right)x/l_0} dx. \quad (7.14)$$

Here, l_0 is the absorption length and θ the scattering angle. This formula can be used to calculate the contribution of a certain penetration depth interval to the total scattering signal:

$$s(x_1, x_2) = \frac{I_{\text{abs}}(x_1, x_2)}{I_{\text{abs}}(0, d)}, \quad (7.15)$$

where d is the thickness of the graphite sample. This expression is very practical to estimate the contribution of the shock-driving plasma to the scattering. Analyzing the hydro simulations which are presented in chapter six shows that in good approximation the first 10 μm of the cold graphite targets are transferred to the hot corona and transport domain by the drive laser. The remaining matter is either still cold or shocked. During the first campaign, the graphite sample thickness was chosen to be 190 μm for the scattering experiments. During the second campaign, the thickness was varied from 120 μm to 180 μm , with a focus on 150 μm . The resulting contributions of the drive laser plasma are shown in the following table.

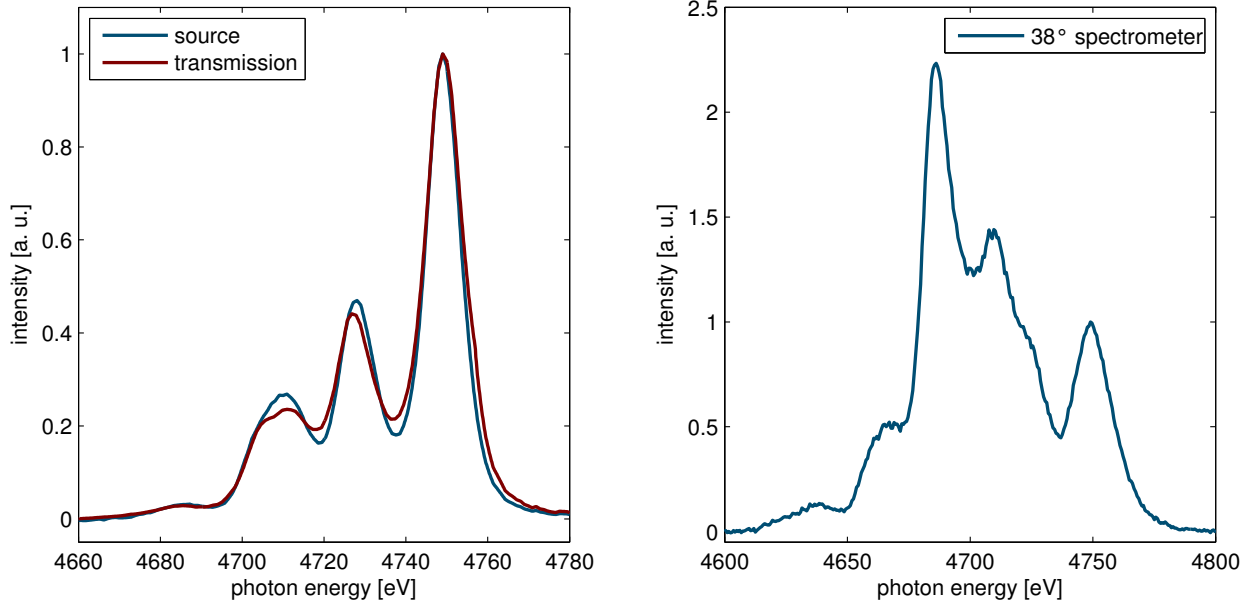


Figure 7.17: On the left: A comparison of the transmission spectrometer and the source spectrometer shows nearly no difference in spectral composition. On the right: recorded spectrum of the 38° spectrometer which was mounted in the second campaign. The strong presence of the satellite lines indicates that colder parts of the X-ray source plasma are visible for this spectrometer.

$d[\mu\text{m}]$	$s(d - 10\mu\text{m}, d)$ for $\theta = 105^\circ$	$s(d - 10\mu\text{m}, d)$ for $\theta = 126^\circ$	Transmission
120	2.23 %	4.23 %	61.2 %
130	1.80 %	3.65 %	58.7 %
140	1.45 %	3.17 %	56.3 %
150	1.18 %	2.76 %	54.1 %
160	0.96 %	2.41 %	51.9 %
170	0.78 %	2.11 %	49.9 %
180	0.63 %	1.86 %	47.9 %
190	0.52 %	1.64 %	45.9 %

These values show that the contribution of the drive laser plasma is rather small for all applied target thicknesses, although around half of the X-ray radiation can transmit through the sample.

7.4 Transmission measurements and 38° spectrometer

The transmission spectrometer was mainly set up to answer the question whether the X-ray spectrum which is transmitted through the titanium foil and the pinhole has the same spectral characteristics as the spectrum which is recorded by directly looking at the laser-plasma interaction. A comparison between the spectra which are recorded by the source and the transmission spectrometers are shown on the left side of figure 7.17. Obviously, there is no notable difference between the two spectra. The small deviations in the intercombination line and the Li-satellite features can be explained by the slightly different line broadening.

The spectrometer looking at 38° scattering angle was originally planned to observe the decrease of the strongest graphite Bragg reflection. Unfortunately, this could not be achieved in the experiment due to a line of sight to outer parts of the plasma corona produced by the backlighter laser.

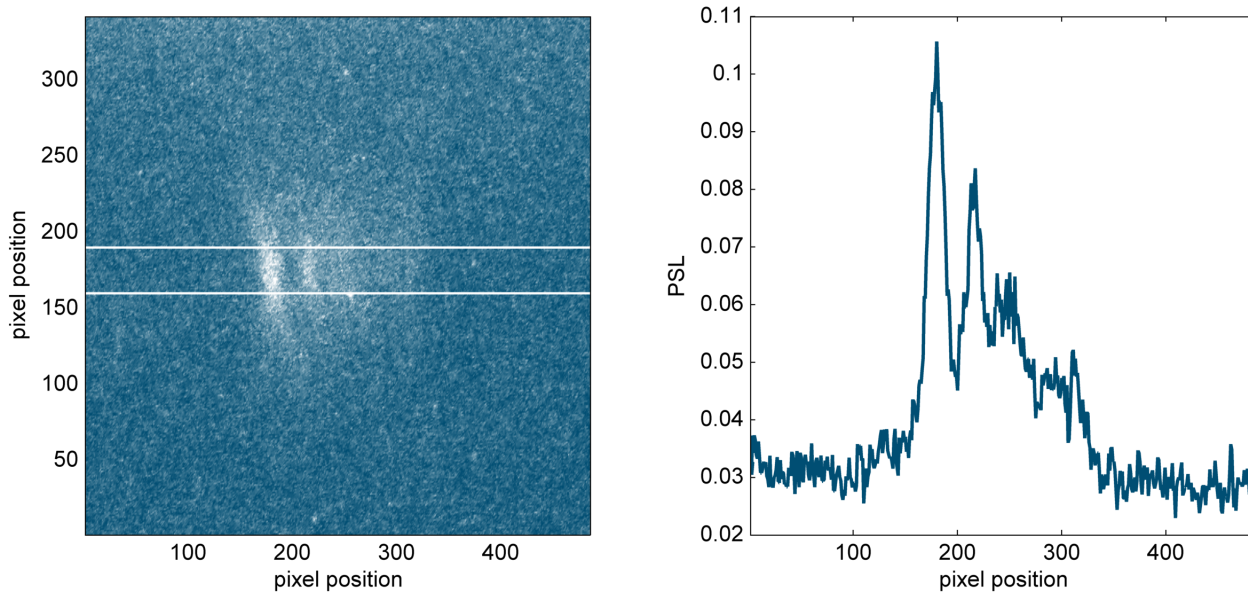


Figure 7.18: On the left: PSL image of the exposed image plates for the 126° scattering spectrometer. The white lines enclose the area which is used for determining the scattering spectra. The corresponding horizontal lineout for this exemplary detector image is shown on the right.

These plasma parts were still hot enough to generate some titanium helium- α radiation. A typical spectrum of the 38° spectrometer is shown on the right side of figure 7.17. Due to the relatively low temperature, the spectrum is significantly different compared to the source radiation from the hot spot. The main transition is dominated by satellite lines of lithium- and beryllium-like titanium ions. The presented exemplary 38° spectrum was monitored with a carbon foil in place. Obviously, it is not possible to decompose the different contributions to the total signal: scattering and the transmitted radiation from the outer plasma corona.

Additionally, there was another effect which could be observed in connection to the transmission and the 38° spectrometer: Both instruments showed relatively large signal fluctuations which are not in direct correlation with the source spectrometer looking from the other side. This is most probably due to small alignment deviations of the backlighter laser. A spatial variation of $50\text{ }\mu\text{m}$ already results in a strong change in the amount of radiation which can be seen by the two spectrometers. As the signals of the backscattering spectrometers scale very well with the source radiation (see following section), it seems unlikely that a pinhole closure due to soft X-ray heating might be responsible for the strong variations. A detailed signal fluctuation analysis of the transmission and the 38° spectrometer can be found in [Roth, 2012].

7.5 Scattering spectra

In this section, the obtained X-ray scattering spectra are presented, analyzed and discussed. For these measurements, the circumstances were again slightly different for the two experimental campaigns. Therefore, the scattering results are discussed in two subsections, one for each campaign.

7.5.1 Experimental campaign March/April 2011

During the first experimental campaign, only the 126° backscattering spectrometer was installed. The relative timing of shock drive and backlighter lasers was varied in the way that scattering data

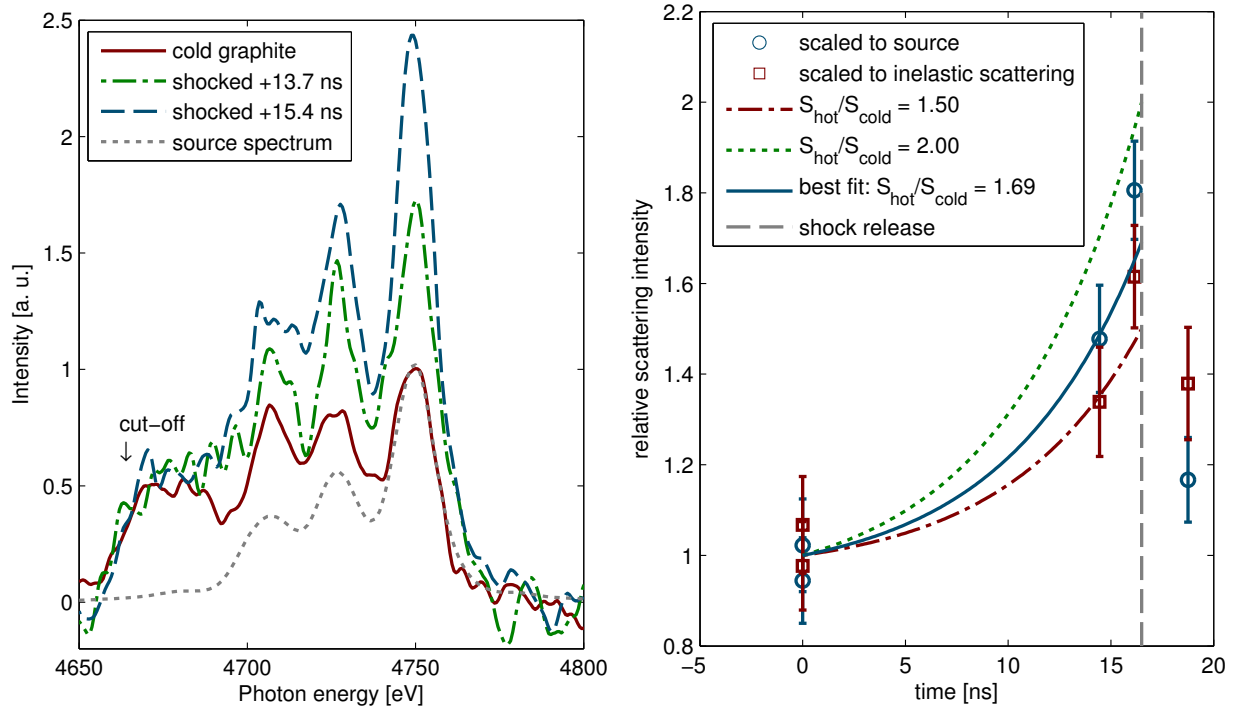


Figure 7.19: On the left: Scattering spectra for cold and shocked graphite samples [Kraus et al., 2012]. All scattering spectra are relatively scaled to the integrated intensity of the recorded source spectrum. A typical source spectrum which is arbitrarily scaled is also shown. On the right: temporal evolution of the integrated scattered intensity scaled to the source radiation and the inelastic scattering.

from a shock wave 2.3 ns before breakout, from a nearly completely shocked sample and from 2.5 ns after the shock release could be collected.

Figure 7.18 exemplarily shows an exposed image plate of the 126° scattering spectrometer. The beryllium filter was working very well: the background level is relatively low and constant. The region within the white lines is used to obtain the final scattering spectrum. On the right side, the averaged lineout of this area is shown. As the background is very flat, a small constant value can be subtracted for background correction. The helium- α , intercombination and satellite peaks can then be used for energy calibration to deduce the final spectrum from this image.

On the left side of figure 7.19, some of the recorded scattering spectra are shown together with a typical source radiation spectrum. The elastic scattering feature which conserves the spectral structure of the source radiation and the energy-reduced inelastic bound-free feature can clearly be identified by comparison with the source spectrum. Elastic scattering can also be seen for cold carbon because a Bragg condition at 115° is marginally covered by the angle distribution implemented in the experiment (see section 7.2.5). Additionally, it is to mention that only about half of the inelastic feature could be collected by the detector. In fact, the cut-off at 4650 eV is due to a piece of shielding in the way of the radiation path. Unfortunately, this had implications on the analysis which will be discussed later. However, what can be seen directly from the spectra of figure 7.19 is that the elastic feature increases strongly for shocked samples. All spectra in this diagram are relatively scaled to the integrated intensity of the corresponding source spectrum. The total shock transit time through the $190\ \mu\text{m}$ thick graphite samples is 16 ns. As the duration of the X-ray pulse is only 1 ns, it is possible to follow the shock motion through the sample by using differ-

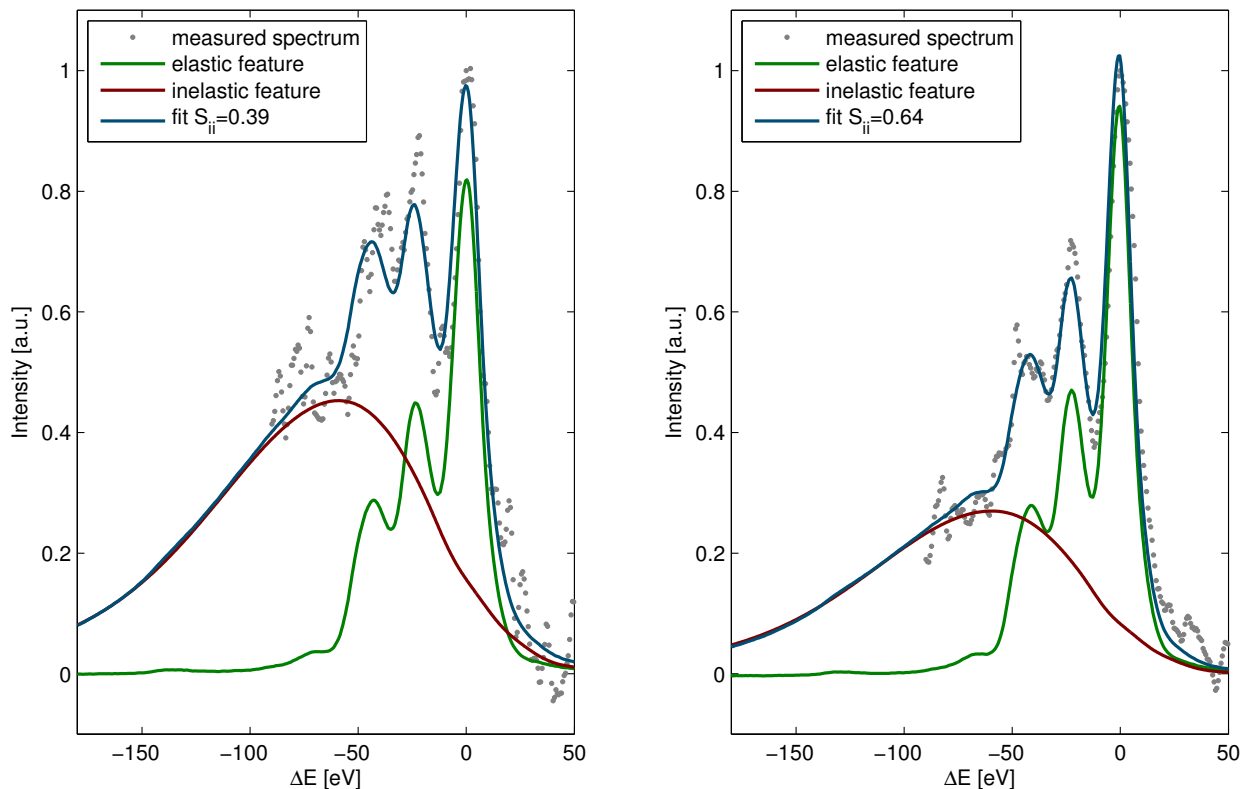


Figure 7.20: 126° scattering spectra from which the structure factor is deduced by determining the ratio of elastic and inelastic scattering. Hereby, only the measured signal which is not influenced by the cut-off is applied. On the left: scattering from cold graphite. On the right: scattering from a completely shocked sample.

ent time delays. Because the photons enter the sample from the opposite side of the shock drive, the signal rises stronger at later times in this backscattering geometry. Due to the exponential attenuation, the probed regions closer to the X-ray source contribute most to the recorded signal. As a consequence, the contribution of the shock-driving plasma to the scattering can be estimated to be only $\sim 2\%$ and, thus, can be neglected (compare section 7.3).

The time diagram of the integrated scattered intensity is shown on the right side of figure 7.19. Hereby, two different scalings have been applied: The data are shown relative to the integrated source radiation as well as scaled to the inelastic feature. Both scalings show a similar temporal behavior within the errorbars. This goes well with the expectation that it is only the elastic feature which increases due to the structure change. Up to the shock release, the data well follow a curve given by the exponential attenuation of the probe radiation according to section 7.3. Hereby, a fixed ratio of integrated scattered intensity between shocked and cold matter was assumed. The best fit is obtained for a ratio of $S_{\text{hot}}/S_{\text{cold}} = 1.69$. After the shock release, the scattered intensity is reduced for both scalings. To illustrate the error margins of the fit, additional curves which correspond to the ratios 1.5 and 2.0 between shock and cold matter, respectively, are drawn into the diagram.

The increase of the elastic scattering fits well to the expected phase transition to the liquid. However, a strong Bragg reflection of cold hexagonal diamond is also present at a scattering angle of $\sim 124^\circ$ for the applied photon energy (see figure 4.6). Obviously, this angle is well covered by the angle distribution of the spectrometer. As already mentioned, hexagonal diamond is a possible

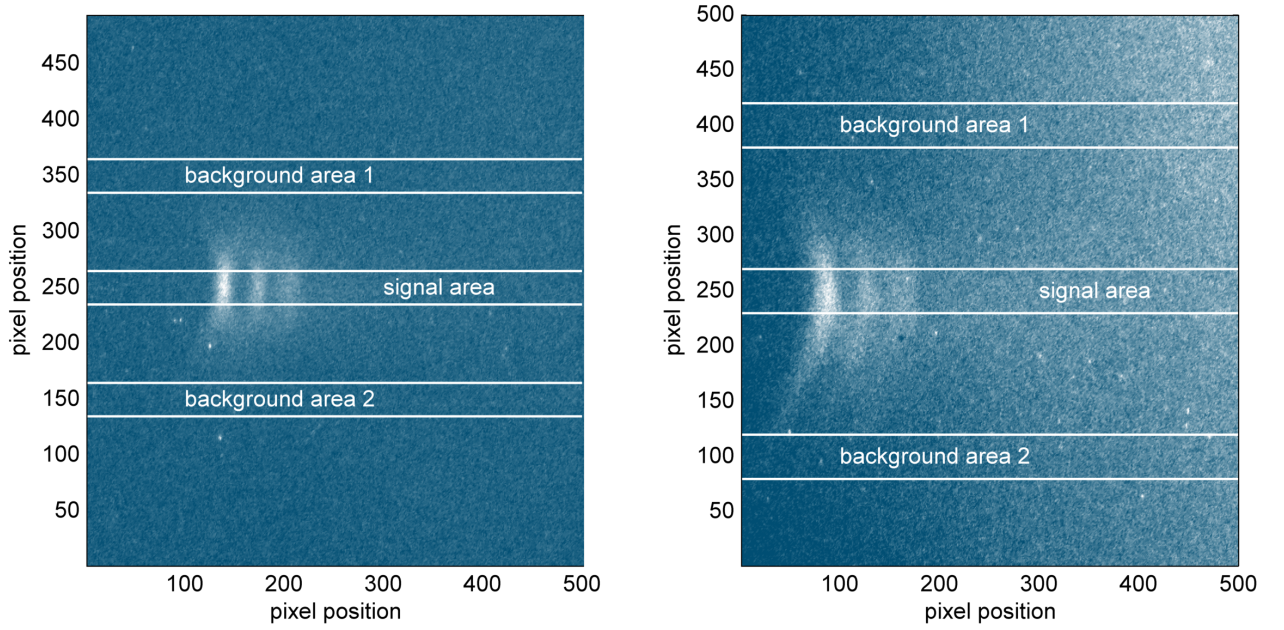


Figure 7.21: PSL images of the exposed image plates for the 105° scattering spectrometer (left) and the 126° scattering spectrometer (right). The areas which are used for the spectrum generation and the background subtraction are marked.

phase which could be formed in the shock wave. Around 105°, there is no strong Bragg reflection of hexagonal diamond which could influence the scattering signal at this angle. This is why such a spectrometer was mounted within the experiments of the second campaign.

Determining an absolute value of $S_{ii}(k)$ in terms of chapter 4.3 is difficult but possible using the scattering data of this campaign. Due to the already mentioned significant cut-off in the low energy part, the inelastic scattering feature is not completely accessible in the measurements. In fact, about half of the total feature is missing because the detector was locally blocked. However, it is still possible to fit the bound-free profiles to the spectra and determine the ratio of elastic scattering to inelastic scattering. Figure 7.20 shows measured spectra for a cold sample and a completely shocked sample together with synthetic compositions of elastic and inelastic scattering which is calculated using the source spectrum and the Compton profiles given by the Coulomb wave assumption (compare section 4.2.3). The resulting structure values are $S_{ii}=0.39\pm0.09$ for the cold case and $S_{ii}=0.64\pm0.11$ for the completely shocked sample. The validity of the synthetic inelastic feature in the region which is not covered by data points is confirmed by the results of the second campaign. These are presented in the following subsection where also the fit method for determining $S_{ii}(k)$ is explained in more detail using more appropriate experimental spectra.

7.5.2 Experimental campaign February/March 2012

In the second campaign, the spectrometer looking at the scattering angle of 105° was mounted in addition to the 126° spectrometer. Figure 7.21 shows exemplarily exposed image plates of both spectrometers. Since plastic foils instead of beryllium filters had to be used for practical purposes in this campaign, the background was not as low and constant as in the previous campaign. This is especially visible in the image obtained by the 126° spectrometer. However, the signal is still well above noise level and the background did not fluctuate arbitrarily but showed the same characteristics in every shot. Therefore, two background regions of the same size as the signal area were defined. These were placed with the same distance above and under the signal area. The average

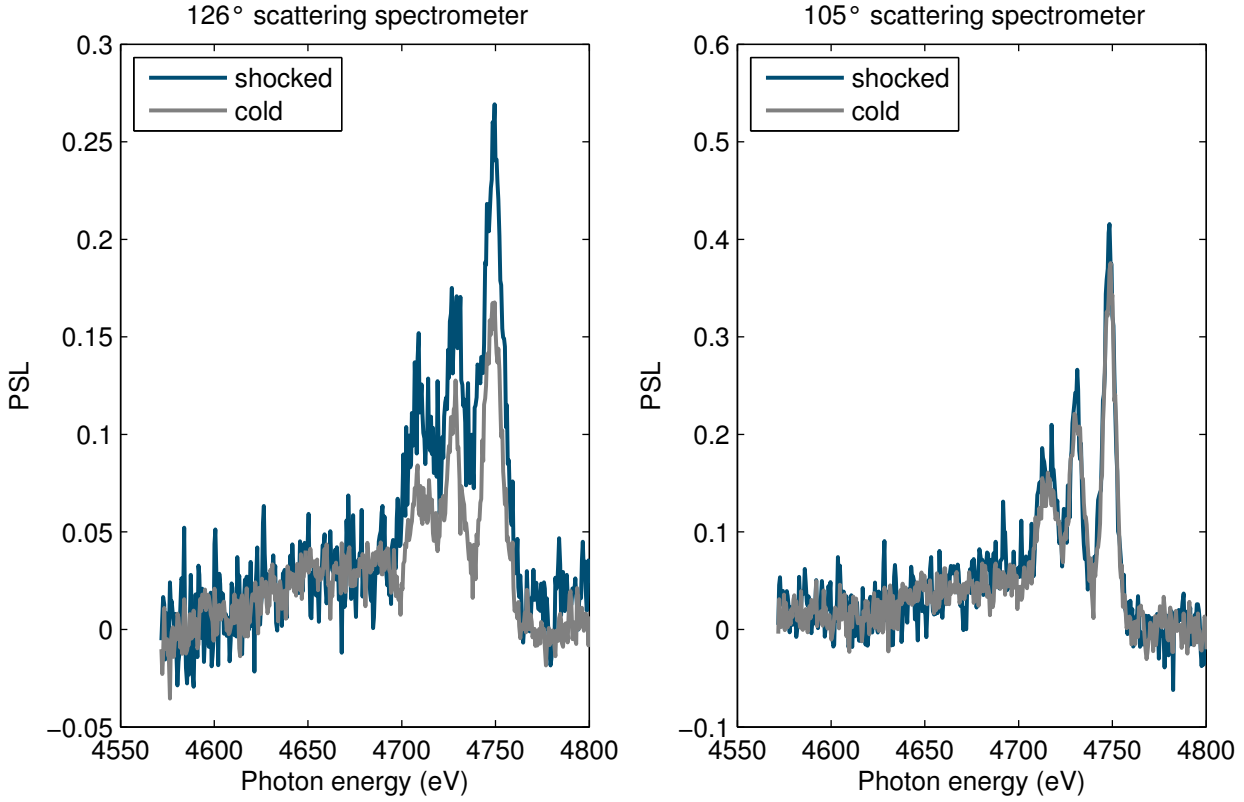


Figure 7.22: Scattering spectra at 126° and 105° for cold and shocked graphite. All spectra are relatively scaled to the integrated intensity of the corresponding source radiation spectrum.

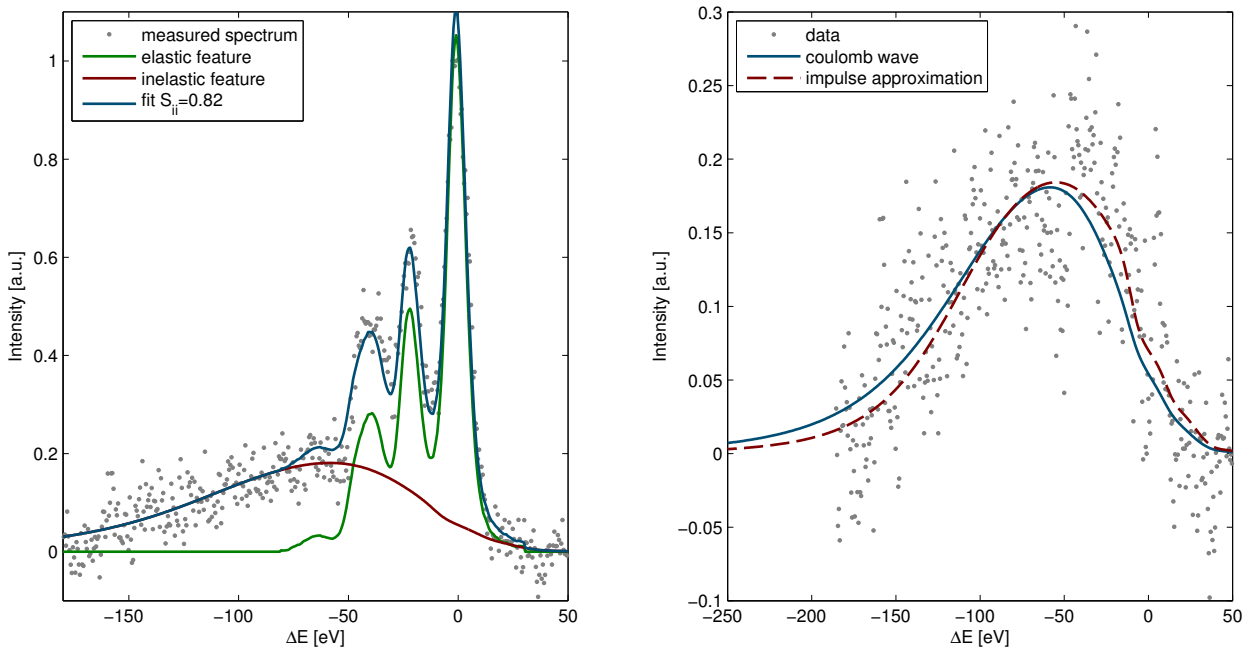


Figure 7.23: On the left: X-ray scattering spectrum (126°) of high quality fitted by the synthetic composition of elastic and inelastic feature. On the right: Comparison of the isolated inelastic feature with the bound-free profiles given by the Coulomb wave assumption and the impulse approximation.

profile of the two background areas can then be subtracted from the scattering signal. This method was very successful in isolating the real signal from the background.

Figure 7.22 shows exemplary scattering spectra of both spectrometers obtained from cold and shocked samples. The background was eliminated in the described way and the spectral features of the titanium helium- α line transition were again applied for the energy calibration. All spectra in these two diagrams are relatively scaled to the integrated intensity of the corresponding source radiation spectrum. It is clearly visible that, again, the elastic feature increases strongly for shocked samples at 126° . The inelastic feature, which is completely visible in this campaign, remains nearly unchanged. The situation at 105° is different. Here, the scattered intensity for both elastic and inelastic feature is nearly identical for cold and shocked samples. This behavior strongly suggests the presence of liquid carbon in the shock wave, as discussed in the previous section. If it was hexagonal diamond instead, the elastic scattering at 105° should be decreased significantly as no Bragg reflection is covered by the spectrometer in this case.

The clear presence of the inelastic feature within the measured spectra can be applied to determine absolute values for the structure factor $S_{ii}(k)$. Using the bound-free profiles from section 4.2.3 in combination with the source spectrum, the scattering data can be compared to synthetic spectra. This is done for a high quality spectrum on the left side of figure 7.23. The data (gray dots) is fitted by a synthetic spectrum (blue) which is composed of the elastic (green) and inelastic feature (red). The inelastic profile is the scaled convolution of the source spectrum and the bound-free profile. The latter is given by the Coulomb wave assumption in this diagram. By integrating the red and green curve separately, the ratio x_{el}/x_{inel} of elastic to inelastic scattering in equation (4.42) can be determined. Since all other quantities on the right side of this equation are known, $S_{ii}(k)$ can be calculated. In this case, the result is $S_{ii}=0.82$. The parameters which are necessary to use equation (4.42) are given in the following table.

Z	Z_{wb}	$k(105^\circ)$	$k(126^\circ)$	$f(105^\circ)$	$f(126^\circ)$
6	4	3.82 \AA^{-1}	4.29 \AA^{-1}	2.47	2.22

The right side of figure 7.23 shows the data where the elastic scattering feature has been subtracted. The remaining inelastic data is fitted by the two bound-free profiles which are presented in section 4.2.3: the Coulomb wave assumption, which includes asymmetric corrections of the bound state, and the impulse approximation, which assumes free electrons with a cut-off at the binding energy. Obviously, the difference of both resulting profiles is relatively small. Thus, considering the existing noise within the measurements, it is not possible to decide which profile fits better to the data. As already mentioned, the spectrum presented in figure 7.23 is already one of the best in terms of signal-to-noise ratio which could be obtained in the experiments. The profile, which is used for the further analysis and the calculation of the structure values, is the Coulomb wave assumption. The physics included in this model should be closer to the real processes of the bound-free scattering.

Figure 7.24 shows the spectrum analysis of scattering data from cold graphite and a nearly completely shocked sample for the 126° spectrometer. The spectrum from the cold sample is plotted on the left side, the data from the shocked target on the right. As the scaling of the total signal is similar in both diagrams, the difference in the ratio of elastic to inelastic scattering between both cases is clearly visible. The resulting structure values are $S_{ii}=0.63\pm0.05$ for the cold case and $S_{ii}=1.10\pm0.08$ for the shocked sample. The examples of figure 7.24 are the two spectra with the most significant difference between cold and shocked targets. The mean structure value for cold graphite at the 125° scattering spectrometer is $S_{ii}=0.75\pm0.04$ and was determined from six individual experiment shots. The error estimation is given by the statistical error of the mean

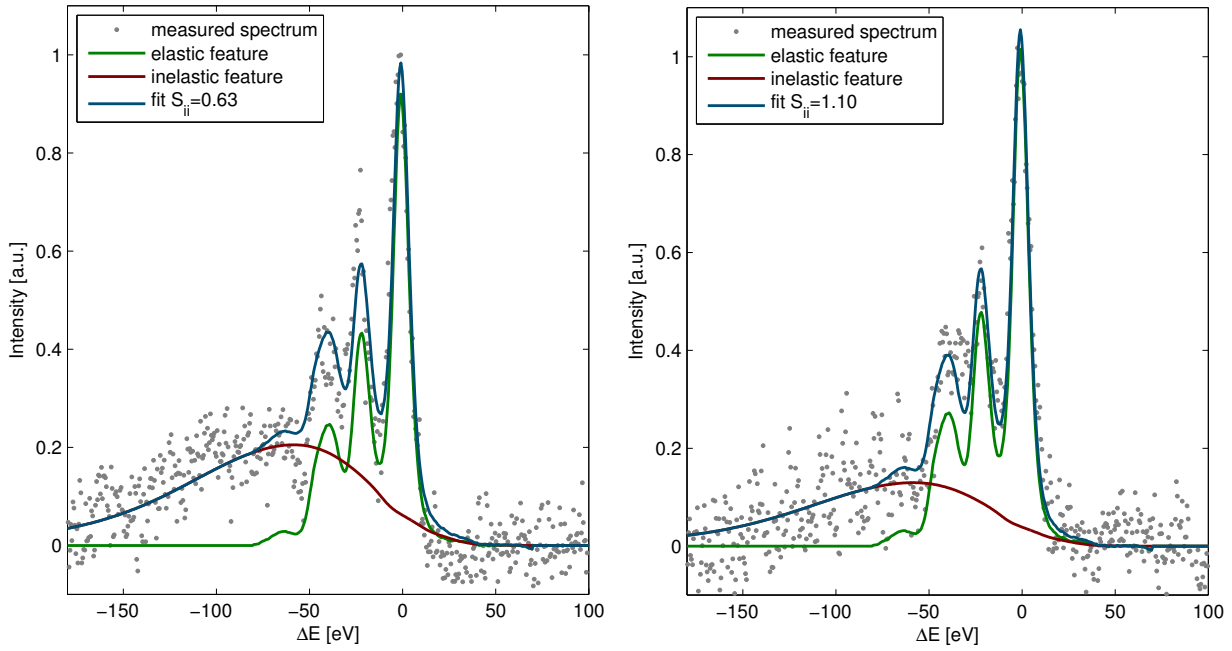


Figure 7.24: 126° scattering spectra from which the structure factor is deduced by determining the ratio of elastic and inelastic scattering. On the left: scattering from cold graphite. On the right: scattering from a completely shocked sample. The ratio of elastic to inelastic feature is strongly increased for the shocked case.

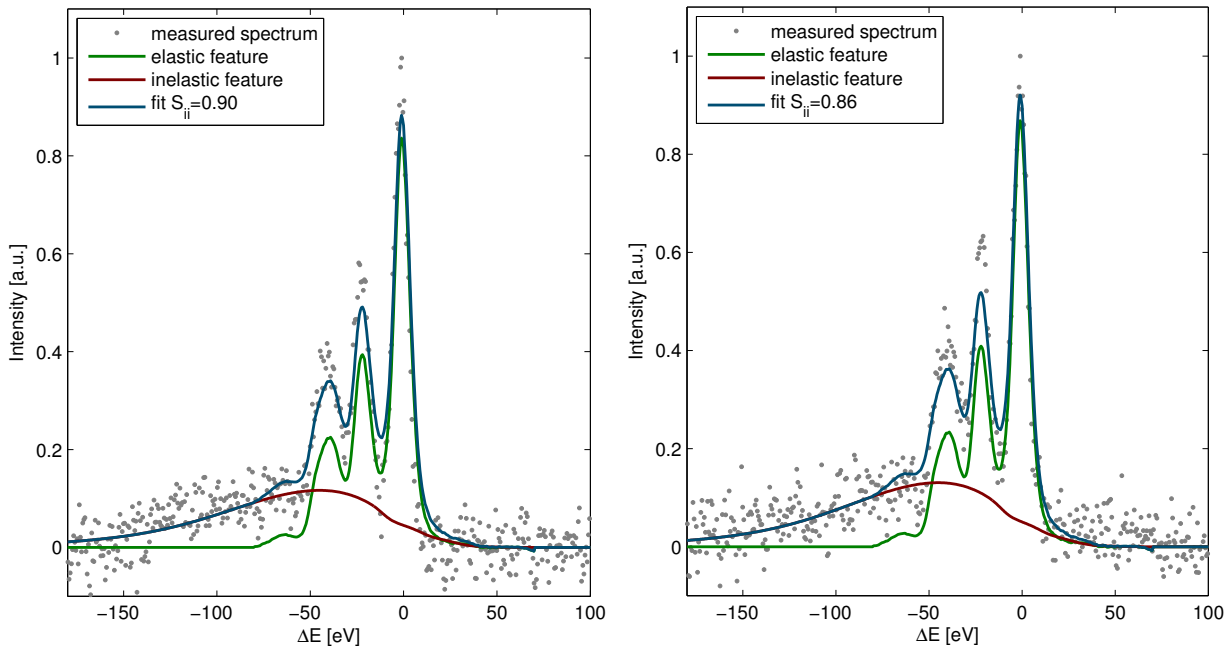


Figure 7.25: 105° scattering spectra from which the structure factor is deduced by determining the ratio of elastic and inelastic scattering. On the left: scattering from cold graphite. On the right: scattering from a completely shocked sample. The resulting structure factors are very similar for both cases.

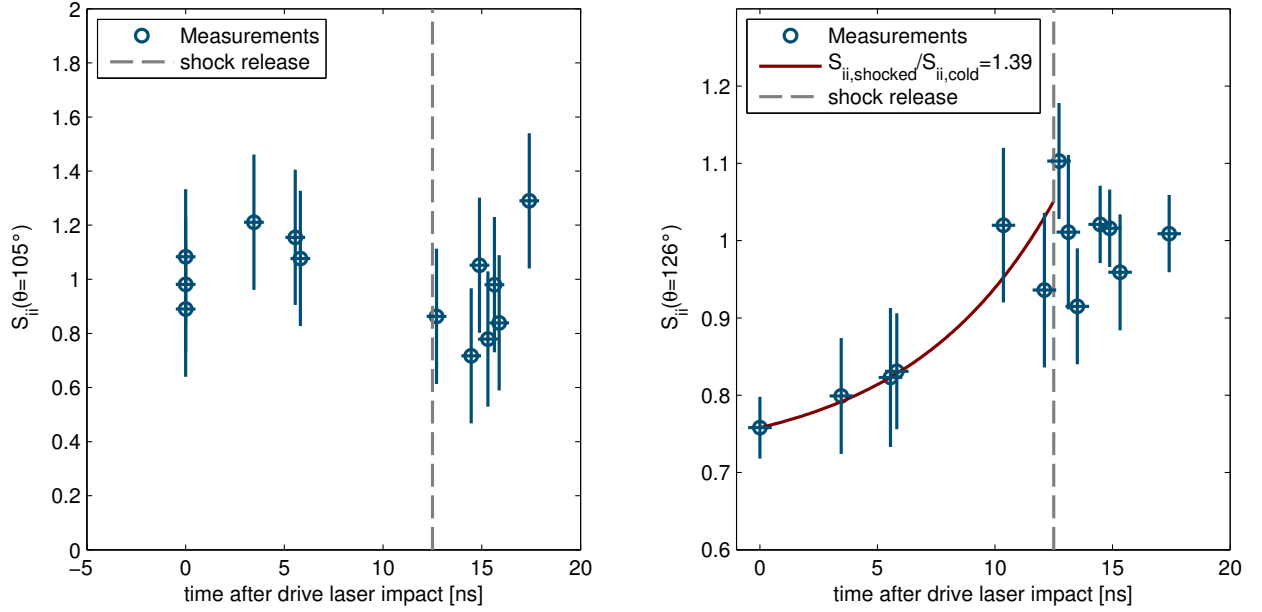


Figure 7.26: Values for the structure factor deduced from the 105° (on the left) and the 126° (on the right) scattering spectrometers.

value which is determined from the six separate scattering spectra. This structure value of cold graphite is significantly larger than in the first experimental campaign. One reason for this effect is that the focal spot of the *PHELIX* laser was larger in the first campaign. Thus, the contribution of the discrete Bragg condition is smaller compared to the remaining angular distribution of the X-rays. Another reason is that different alignment schemes for the backlighter laser were used in the two campaigns. The alignment setup in the first campaign most probably led to slightly larger scattering angles ($\sim +2^\circ$) due to the shifted position of the X-ray source. This also reduces the contribution of the Bragg reflection to the scattering spectra from cold graphite.

The analysis of the 105° scattering spectra does not reach a comparable precision as it is obtained for the 126° spectra. Since the momentum transfer within the scattering process decreases for smaller scattering angles, the energy shift of the inelastic feature is reduced compared to 126° . Thus, it is more difficult to decompose elastic and inelastic feature. Additionally, the elastic feature is significantly increased at 105° compared to the scattering angle of 126° for a similar structure value. This is due to the $|f(k)|^2$ scaling of the elastic scattering (compare section 4.2.1). Therefore, the ratio x_{el}/x_{inel} is much larger at 105° than it is at 126° for the same structure value. Thus, small variations of x_{inel} due to noise already have a large impact on the fit result. However, the analysis is possible and scattering at 105° results in a mean structure value of $S_{ii}=1.01\pm0.18$ for cold graphite. This value is larger than for 126° because three significant Bragg angles are covered by the angle distribution of this spectrometer (compare section 7.2.5). As the structure factor, which is obtained by the 105° scattering spectrometer for cold and shocked samples, is very similar, it is not possible to distinguish between the two cases. This is underlined in figure 7.25 where the 105° scattering spectra which correspond to the 126° data sets of figure 7.24 are shown. For 105° , the resulting structure factors are nearly unchanged comparing cold and nearly completely shocked samples.

Figure 7.26 shows the temporal evolution of $S_{ii}(k)$ for the propagating shock wave to the shock release and beyond. At 105° the resulting structure factor does not change significantly within the errorbars but stays more or less constant. The measured value directly at the shock release is

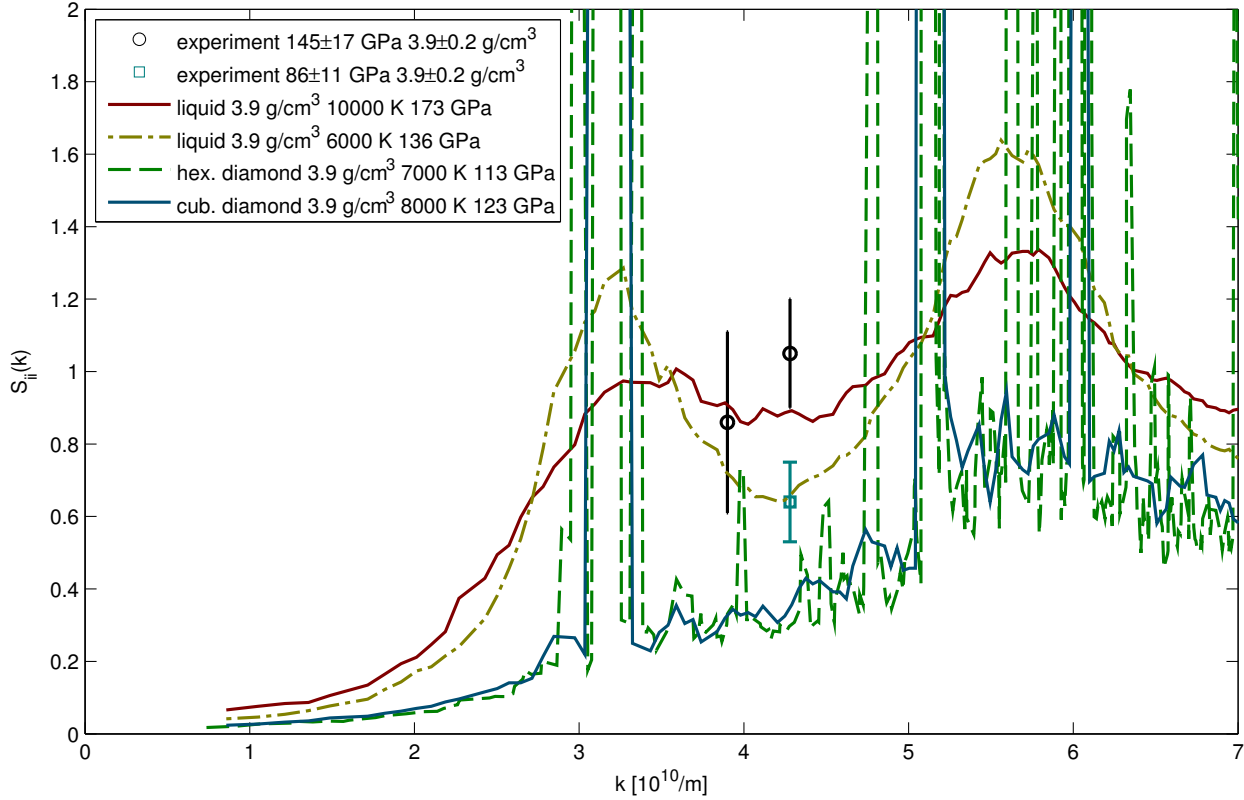


Figure 7.27: Comparison of the obtained structure values with the ab-initio simulations.

$S_{ii}=0.86\pm0.25$ for this angle. The situation for 126° is different. Here, the structure values well follow an exponential increase up to the shock release. This curve is defined by the exponential attenuation of the X-rays inside the carbon samples. Furthermore, a fixed ratio of S_{ii} between shocked and cold matter is assumed. The best fit is calculated for $S_{ii,\text{shocked}}/S_{ii,\text{cold}}=1.39\pm0.2$ which results in $S_{ii}=1.05\pm0.15$ for shocked matter at 126° . After the shock release, the values of S_{ii} scatter around 1.0 for both scattering angles.

7.6 Conclusions

The velocity measurements illustrate that conditions were achieved inside the shock wave where the existence of three different graphite phases is possible according to the DFT-MD simulations. However, the X-ray scattering data clearly prove the presence of liquid carbon inside the laser-driven shock wave, especially in the experiments of the second campaign. Figure 7.27 underlines this result. Here, an extract of the DFT-MD simulations is compared to the structure values which are obtained for completely shocked samples. As stated in section 6.2.2, it is clearly visible that the chosen scattering angles are very well suited to monitor the carbon solid-liquid phase transition in this pressure regime. The resulting k -values of 3.82\AA^{-1} (105°) and 4.29\AA^{-1} (126°) fall into a region where the structure factor of the solid phases is not dominated by strong remaining Bragg maxima. Obviously, the experimental results are in better agreement with the liquid phase than with both diamond phases.

Figure 7.27 also shows that the Bragg peak of hexagonal diamond which was expected to be around $k \approx 4.3\text{\AA}^{-1}$ does not affect the 126° scattering spectrometer. Due to shock compression to a density which is larger than the density of cold hexagonal diamond ($\sim 3.3\text{ g/cm}^3$), the Bragg

maximum is shifted to $k \approx 4.8 \text{ \AA}^{-1}$. Thus, the 126° scattering spectrometer is technically sufficient to distinguish between solid and liquid phases in this pressure regime. As a consequence, it can be stated that liquid carbon was also present in the experiments of the first campaign. Here, the pressures were significantly lower compared to the second campaign. According to the ab-initio simulations, these conditions would favor the diamond phases over the liquid state. This suggests that the relaxation of the shocked material after the transition shock front already starts from a disordered liquid-like state. According to the hysteresis of the phase transition, the liquid phase is then still stable over the diamond phases to relative low temperatures and pressures. This is underlined by the measured structure factor of $S_{ii} = 0.64 \pm 0.11$ for the completely shocked sample in the first experimental campaign. This value fits very well to the DFT-MD calculations for the liquid phase at 3.9 g/cm^3 and 6000 K . Here the liquid is only just stable over the diamond phase (compare section 6.2). Another explanation for the still existing liquid at this pressure and temperature could be the discussed preheating due to the X-rays from the backlighter source. This is however relatively unlikely as described in section 7.2.4.

The behavior of the structure factor after the shock release is also reasonable. The measured value of $S_{ii}(k)$ scatters closely around one which can be explained by the fast density decrease of the released material. The temperature, however, remains nearly unchanged at this time scale (compare the hydro simulations of chapter six). Thus, a liquid (or gas) without significant correlations can be expected to be present in the shock release. Such a state corresponds to a more or less constant value of $S_{ii}(k) = 1$.

Finally, it can be concluded that the presented measurements observed for the first time reliably the formation of liquid carbon under shock compression using graphite as initial state.



8 Outlook

Using laser-driven shocks and X-ray scattering techniques, the experiments presented in this thesis show a successful way to characterize phase transitions in warm dense matter. However this can only be seen as a start since warm dense matter studies are in general still in a very initial state. This chapter gives a brief outlook on further improvements of the presented experiments on the melting of graphite under shock compression. Additionally, different future instruments with high potential for the investigation of phase transitions in warm dense matter will be discussed. These are 4th generation light sources, like the LCLS in Stanford or the future European XFEL in Hamburg, and intense particle beams which can be generated by laser-based acceleration schemes and future high intensity conventional accelerators like the FAIR facility in Darmstadt.

8.1 Further improvements of the presented experiments

The experiments in the framework of this thesis show the presence of a liquid state in a region of the carbon phase diagram where the state of matter was not probed experimentally before. However the real transition from diamond to the liquid state has still not been measured as liquid carbon seems to be present for all driving intensities of the presented experiments. Thus, the aim of future experiments should be to find the drive-laser intensity where the diamond-liquid transition happens on the graphite Hugoniot curve. The high pressure diamond state is also very interesting as it is not yet clear whether a cubic or hexagonal structure is dominating the crystal lattice in this case.

A very powerful instrument is definitely the application of graphite types with different porosity. In this way, the initial density can be varied which also results in a larger variety of possible final states. This would ideally give the possibility to draw an experimentally obtained melting line into the carbon phase diagram in the regime of 100 GPa for the first time. Additionally, the lattice structure of the diamond state shortly before melting could be different for varying initial graphite states. For example, compressing highly oriented pyrolytic graphite (HOPG) parallel to the c-axis should have a higher probability of forming hexagonal diamond than compressing randomly oriented pressed graphite [Kanel et al., 2010]. The Hugoniot of these materials in the region above 100 GPa could be determined with more accuracy using a VISAR (velocity interferometer system for any reflector). Having such a device, especially the particle velocity could be determined with much more precision compared to the multi-frame shadowgraphy method. A VISAR for the characterization of laser-driven shocks was constructed very recently at GSI [Ionita et al., 2012] and can be applied in future experiments.

Another obvious improvement would be a more planar shock drive into the graphite samples. This requires a larger focal spot and thus a significantly larger drive laser energy to keep the intensity similar. Unfortunately, the *nhelix* laser system is not capable to deliver these energies. But as a matter of fact, an experiment at a more powerful laser facility is already around the corner. Following the success of the experimental campaigns at GSI, a proposal for a more advanced experiment at the VULCAN laser facility of the Rutherford Appleton Laboratory has been approved and is already scheduled for January/February 2013. Figure 8.1 shows the planned experimental setup at the target area west of VULCAN. The combination of four strong long pulse beams allows for a focal spot size of 1 mm in diameter. Random phase

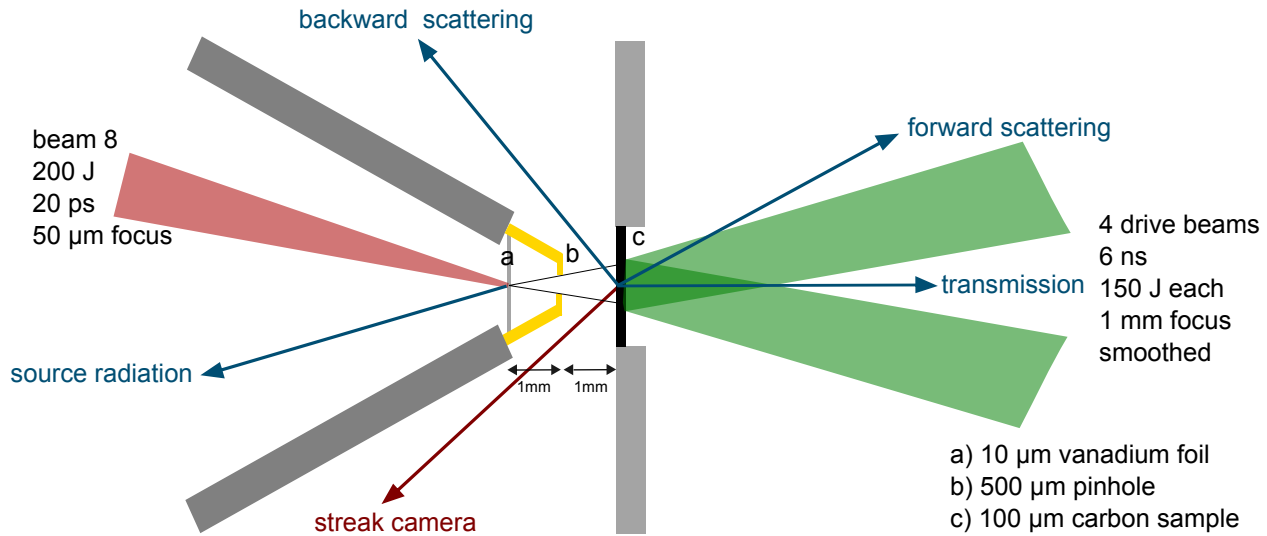


Figure 8.1: Sketch of the planned experimental setup at target area west of the VULCAN laser at the Rutherford Appleton Laboratory, UK.

plates will be applied to smooth the intensity profile of this large spot. Another modification is that a high energy short pulse will be used to produce the X-rays for backlighting. A laser intensity of $\sim 10^{17}$ W/cm² can produce K- α radiation very efficiently [Kritcher et al., 2009; Neumayer et al., 2010]. A K- α backlighter has numerous benefits compared to thermal helium- α sources: The duration of the produced X-ray flash is in the order of the laser pulse length (20 ps in this case). Therefore, the time resolution will be strongly improved using a short pulse laser. Additionally, the line width of a K- α transition is much smaller than the corresponding helium- α transition because the satellite lines are not as distinct and only exist on the high energy side of the main transition. Thus, it will be easier to distinguish elastic and inelastic features in the obtained scattering spectra. Furthermore, K- α radiation is mainly produced in the cold material where the backlighter laser hits the target foil and not in the plasma corona. This will give a much better chance to observe forward scattering which is not overlaid by source radiation from the corona as it was in the campaigns presented in this thesis. The reduced line width would then also allow for the observation of possible plasmon features [Glenzer et al., 2007; Neumayer et al., 2010]. Finally, the chosen line transition is optimal for this kind of experiment as it is easily possible to implement forward and backward scattering angles where no strong graphite Bragg condition is fulfilled (see figure 8.2). Thus, this experiment will allow for the measurement of the carbon melting line around 100 GPa using different types of graphite as initial state.

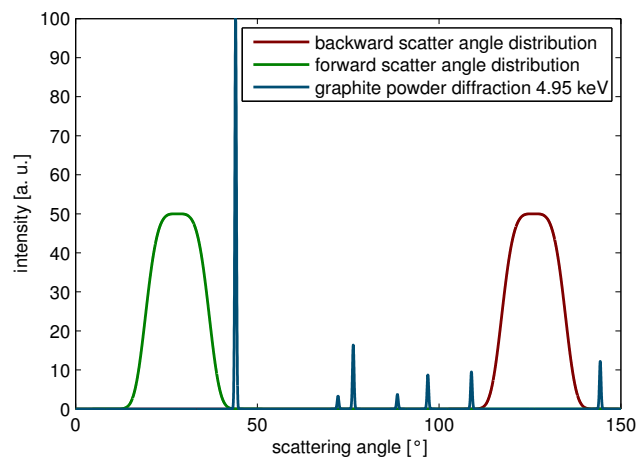


Figure 8.2: Angle distributions for the planned experiment at VULCAN.

8.2 Isochoric heating with intense laser-generated particle beams

An alternative way to produce well-defined warm dense matter states is the isochoric heating with intense particle beams. The still young technique of laser-accelerated proton beams proved to be able to heat solid-density samples up to temperatures of ~ 20 eV before expansion occurs [Dyer et al., 2008]. By focusing the generated proton beams using special target geometries, even higher temperatures may be possible [Patel et al., 2003; Bartal et al., 2011]. With this method, different states of matter can be accessed compared to the shock-compression technique. Additionally, there is some overlap of the two methods. For example, isochoric heating of diamond, which has a density of 3.52 g/cm^3 would lead to similar states around the melting region as those which can be accessed by shock-compression of porous graphite.

The combination of laser-accelerated proton beams and X-ray scattering in the same experiment provides some difficulties. Since efficient laser-driven particle acceleration requires relativistic intensities of at least 10^{18} W/cm^2 , the parallel production of high energy X-rays and even gamma-rays cannot be avoided. This results in very high background and noise levels on the X-ray detectors, often totally covering the relatively faint scattering signals [Pelka, 2010]. Fortunately, significant progress concerning shielding techniques could be achieved in the past years which allows for an improved analysis of scattering spectra from samples which were heated by laser-accelerated protons.

8.3 4th generation light sources

Looking further into the future, the most promising tools to study ultra-fast atomic dynamics are X-ray free electron lasers, often called 4th generation light sources. At the moment, there is only one facility of this kind existing worldwide: the Linac Coherent Light Source (LCLS) in Stanford. However, there are many more to come in the future, for example the European XFEL in Hamburg, the SACLA(XFEL) facility in Japan or the MARIE facility in Los Alamos. These machines will definitely be a big pillar to study microscopic states of warm dense matter in the future. LCLS, for example, currently offers 10^{11} - 10^{12} directed and coherent photons with a pulse duration of 70-300 fs. The photon energy can be varied from 4 keV to 25 keV and is highly monochromatic ($\Delta E/E \approx 0.2\%$) compared to laser-driven line transitions. Thus, XFELs are the perfect backlighter for X-ray scattering experiments on warm dense matter. However, these machines still require instruments to produce WDM states. At LCLS, there is the Matter at Extreme Conditions (MEC) facility which offers a long pulse and a short pulse laser in addition to the X-ray beam. The long pulse option (50 J in 2-200 ns) is comparable to the *nhelix* system at GSI and is aimed to drive shock waves into samples to produce WDM states. Therefore, the experiments presented in this thesis could be repeated with much higher accuracy at the MEC facility which started the commissioning phase in 2012. For the far future, it is even planned to set up monochromators at LCLS which would allow for a band width which is small enough to even resolve the collective atom/ion dynamics in warm dense matter. Such a measurement is urgently needed to test existing warm dense matter models.

8.4 Perspectives for WDM experiments at FAIR

Another upcoming facility which will give the possibility for a unique investigation of WDM is the Facility for Antiproton and Ion Research (FAIR) which is under construction next to GSI in Darmstadt. High intensity ion beams will allow for specific energy depositions of several hundred thousand Joules per gram which leads to pressures up to several 100 GPa. With a focal spot size

of ~ 1 mm this technique can produce relatively large and long-living WDM in the laboratory. In contrast to XFEL facilities, which are more aimed to study fast non-equilibrium dynamics, ion-beam-generated WDM can be used for the investigation of homogeneous samples in equilibrium.

A high energy laser is planned to be built at the plasma physics experimental cave at FAIR. This machine is mainly aimed to produce backlighter X-ray radiation for scattering and radiography purposes. In fact, X-ray scattering will be a central diagnostics for all three upcoming plasma physics experiments at FAIR. As the experiments presented in this thesis were the first X-ray scattering experiments ever performed at GSI, this work should be continued facing the upcoming FAIR facility. The available *PHELIX* laser system offers capabilities to further develop and test backlighter principles which can be applied for FAIR. Furthermore, the recently implemented two-beam option allows for pump-probe experiments directly at *PHELIX* without using the *nhelix* laser system. Here, the further investigation of carbon in warm dense matter states is imaginable following the previous experiments. Finally, cryogenic targets, which are currently developed at TU Darmstadt [Menzel, 2010; Bedacht et al., 2012], would open the possibility to investigate warm dense hydrogen which would directly address fundamental astrophysical problems.

Bibliography

- B. J. Alder and R. H. Christian. Behavior of strongly shocked carbon. *Physical Review Letters*, 7: 367–369, 1961.
- J. Arthur et al. Linac Coherent Light Source (LCLS) - conceptual design report. *Technical report, SLAC, Stanford*, 2002.
- S. Atzeni and J. Meyer-ter-Vehn. *The Physics of Inertial Fusion*. Clarendon Press, Oxford, 2004.
- V. Bagnoud, B. Aurand, A. Blazevic, S. Borneis, C. Bruske, B. Ecker, U. Eisenbarth, J. Fils, A. Frank, E. Gaul, S. Goette, C. Haefner, T. Hahn, K. Harres, H.-M. Heuck, D. Hochhaus, D. Hoffmann, D. Javorková, H.-J. Kluge, T. Kuehl, S. Kunzer, M. Kreutz, T. Merz-Mantwill, P. Neumayer, E. Onkels, D. Reemts, O. Rosmej, M. Roth, T. Stoehlker, A. Tauschwitz, B. Zielbauer, D. Zimmer, and K. Witte. Commissioning and early experiments of the PHELIX facility. *Applied Physics B: Lasers and Optics*, 100:137–150, 2010.
- T. Bartal, M. E. Foord, C. Bellei, M. H. Key, K. A. Flippo, S. A. Gaillard, D. T. Offermann, P. K. Patel, L. C. Jarrott, D. P. Higginson, M. Roth, A. Otten, D. Kraus, R. B. Stephens, H. S. McLean, E. M. Giraldez, M. S. Wei, D. C. Gautier, and F. N. Beg. Focusing of short-pulse high-intensity laser-accelerated proton beams. *Nature Physics*, 7(12):1–4, 2011.
- D. Batani, H. Stabile, A. Ravasio, G. Lucchini, F. Strati, T. Desai, J. Ullschmied, E. Krousky, J. Skala, L. Juha, B. Kralikova, M. Pfeifer, C. Kadlec, T. Mocek, A. Präg, H. Nishimura, and Y. Ochi. Ablation pressure scaling at short laser wavelength. *Physical Review E*, 68:067403, 2003.
- D. Batani, F. Strati, H. Stabile, M. Tomasini, G. Lucchini, A. Ravasio, M. Koenig, A. Benuzzi-Mounaix, H. Nishimura, Y. Ochi, J. Ullschmied, J. Skala, B. Kralikova, M. Pfeifer, C. Kadlec, T. Mocek, A. Präg, T. Hall, P. Milani, E. Barborini, and P. Piseri. Hugoniot data for carbon at megabar pressures. *Physical Review Letters*, 92(6):65503, 2004.
- S. Bedacht, G. Schaumann, A. Blazevic, M. Roth, and D. H. H. Hoffmann. Cryogenic Targets for Laser and Particle Beams. *GSI Scientific Report 2011*, pages PNI–PP–25, 2012.
- A. Ben-Kish, A. Fisher, E. Cheifetz, and J. L. Schwob. Extreme ultraviolet-vacuum ultraviolet spectrum detection using image plates. *Review of Scientific Instruments*, 71(7):2651–2654, 2000.
- A. Benuzzi-Mounaix, M. Koenig, G. Huser, B. Faral, D. Batani, E. Henry, M. Tomasini, B. Marchet, T. A. Hall, M. Boustie, T. De Resseguier, M. Hallouin, F. Guyot, D. Andrault, and T. Charpin. Absolute equation of state measurements of iron using laser driven shocks. *Physics of Plasmas*, 9(6):2466, 2002.
- B. J. Bloch and L. B. Mendelsohn. Comparison of methods for calculating atomic shielding factors. *Physical Review A*, 12(4):1197, 1975.
- M. Börner. Aufbau eines Nomarski-Multiframe-Interferometers zur Bestimmung der freien Elektrodendichte in lasererzeugten Plasmen. *Master Thesis, TU Darmstadt*, 2010.
- M. Börner, J. Fils, A. Frank, A. Blažević, T. Hessling, A. Pelka, G. Schaumann, A. Schökel, D. Schumacher, M. M. Basko, J. Maruhn, An. Tauschwitz, and M. Roth. Development of a nomarski-type multi-frame interferometer as a time and space resolving diagnostics for the free electron density of laser-generated plasma. *Review of Scientific Instruments*, 83(4):043501, 2012.

- D. K. Bradley, J. H. Eggert, D. G. Hicks, P. M. Celliers, S. J. Moon, R. C. Cauble, and G. W. Collins. Shock Compressing Diamond to a Conducting Fluid. *Physical Review Letters*, 93(19):1–4, 2004.
- F. P. Bundy. Pressure-temperature phase diagram of elemental carbon. *Physica A: Statistical Mechanics and its Applications*, 156(1):169–178, 1989.
- F. P. Bundy and J. S. Kasper. Hexagonal Diamond - A new form of carbon. *The Journal of Chemical Physics*, 46(00):3437, 1967.
- J. Chihara. Difference in X-ray scattering between metallic and non-metallic liquids due to conduction electrons. *Journal of Physics F: Metal Physics*, 17:295, 1987.
- J. Chihara. Interaction of photons with plasmas and liquid metals-photoabsorption and scattering. *Journal of Physics: Condensed Matter*, 12:231, 2000.
- H.-K. Chung, M. H. Chen, W. L. Morgan, Y. Ralchenko, and R. W. Lee. Flychk: Generalized population kinetics and spectral model for rapid spectroscopic analysis for all elements. *High Energy Density Physics*, 1(1):3 – 12, 2005.
- A. A. Correa, S. A. Bonev, and G. Galli. Carbon under extreme conditions: Phase boundaries and electronic properties from first-principles theory. *Proceedings of the National Academy of Sciences of the United States of America*, 103(5):1204, 2006.
- A. A. Correa, L. X. Benedict, D. Young, E. Schwegler, and S. A. Bonev. First-principles multiphase equation of state of carbon under extreme conditions. *Physical Review B*, 78(2):24101, 2008.
- CrystalMaker Software. CrystalDiffract. Webpage: <http://www.crystallmaker.com/crystaldiffract>, 2012.
- J. Daligault and S. Gupta. Electron-ion scattering in dense multi-component plasmas: application to the outer crust of an accreting neutron star. *Astrophysical Journal*, 703:994–1011, 2009.
- M. S. del Rio, M. Gambaccini, G. Pareschi, A. Taibi, A. Tuffanelli, and A. K. Freund. Focusing properties of mosaic crystals. *Crystal and Multilayer Optics*, 3448(1):246–255, 1998.
- DESY XFEL Project Group. The european X-ray free-electron laser - technical design report. *Technical report, DESY, Hamburg*, 2006.
- R. P. Drake. High energy density physics. *Springer, Berlin*, 2006.
- P. Dufour, J. Liebert, G. Fontaine, and N. Behara. White dwarf stars with carbon atmospheres. *Nature*, 450(7169):522–4, 2007.
- G. M. Dyer, A. C. Bernstein, B. I. Cho, J. Osterholz, W. Grigsby, A. Dalton, R. Shepherd, Y. Ping, H. Chen, K. Widmann, and T. Ditmire. Equation-of-state measurement of dense plasmas heated with fast protons. *Physical Review Letters*, 101(1):15002, 2008.
- J. H. Eggert, D. G. Hicks, P. M. Celliers, D. K. Bradley, R. S. McWilliams, R. Jeanloz, J. E. Miller, T. R. Boehly, and G. W. Collins. Melting temperature of diamond at ultrahigh pressure. *Nature Physics*, 6(1):40–43, 2009.
- P. Eisenberger and P. M. Platzman. Compton scattering of x rays from bound electrons. *Physical Review A*, 2(2):415–423, 1970.
- S. Eliezer. The interaction of high-power lasers with plasmas. *Institute of Physics Publishing, Bristol and Philadelphia*, 2002.

- S. Eliezer and K. Mima. Applications of laser-plasma interactions. *CRC Press, New York*, 2009.
- D. J. Erskine and W. J. Nellis. Shock-induced martensitic phase transformation of oriented graphite to diamond. *Nature*, 349(6307):317–319, 1991.
- V. Fortov, G. Kanel, A. Utkin, O. Vorobiev, G. Kessler, H. Karow, K. Baumung, B. Goel, and V. Light. Intense shock waves in hot dense matter generated by high-power light ion beams. *AIP Conference Proceedings*, 369(1):1060–1065, 1996.
- A. Frank. Energieverlust und Umladung von schweren Ionen in lasererzeugten Plasmen. *PhD Thesis, TU Darmstadt*, 2012.
- E. Garcia Saiz, G. Gregori, D. O. Gericke, J. Vorberger, B. Barbreil, R. J. Clarke, R. R. Freeman, S. H. Glenzer, F. Y. Khattak, M. Koenig, O. L. Landen, D. Neely, P. Neumayer, M. M. Notley, A. Pelka, D. Price, M. Roth, M. Schollmeier, C. Spindloe, R. L. Weber, L. van Woerkom, K. Wünsch, and D. Riley. Probing warm dense lithium by inelastic X-ray scattering. *Nature Physics*, 4(12):940–944, 2008.
- D. O. Gericke. *Personal communication*, 2012.
- D. O. Gericke, J. Vorberger, K. Wünsch, and G. Gregori. Screening of ionic cores in partially ionized plasmas within linear response. *Physical Review E*, 81:065401, 2010.
- S. H. Glenzer and R. Redmer. X-ray Thomson scattering in high energy density plasmas. *Reviews of Modern Physics*, 81(December):1625–1663, 2009.
- S. H. Glenzer, G. Gregori, R. W. Lee, F. J. Rogers, S. W. Pollaine, and O. L. Landen. Demonstration of spectrally resolved X-ray scattering in dense plasmas. *Physical Review Letters*, 90(17):175002, 2003.
- S. H. Glenzer, O. L. Landen, P. Neumayer, R. W. Lee, K. Widmann, S. W. Pollaine, R. J. Wallace, G. Gregori, A. Höll, T. Bornath, R. Thiele, V. Schwarz, W.-D. Kraeft, and R. Redmer. Observations of plasmons in warm dense matter. *Physical Review Letters*, 98(6):65002, 2007.
- S. H. Glenzer, B. J. MacGowan, P. Michel, N. B. Meezan, L. J. Suter, S. N. Dixit, J. L. Kline, G. A. Kyrala, D. K. Bradley, D. A. Callahan, E. L. Dewald, L. Divol, E. Dzenitis, M. J. Edwards, A. V. Hamza, C. A. Haynam, D. E. Hinkel, D. H. Kalantar, J. D. Kilkenny, O. L. Landen, J. D. Lindl, S. LePape, J. D. Moody, A. Nikroo, T. Parham, M. B. Schneider, R. P. J. Town, P. Wegner, K. Widmann, P. Whitman, B. K. F. Young, B. Van Wonterghem, L. J. Atherton, and E. I. Moses. Symmetric inertial confinement fusion implosions at ultra-high laser energies. *Science*, 327(5970):1228–1231, 2010.
- G. Gregori, S. H. Glenzer, W. Rozmus, R. W. Lee, and O. L. Landen. Theoretical model of x-ray scattering as a dense matter probe. *Physical Review E*, 67(2):26412, 2003.
- G. Gregori, S. H. Glenzer, F. J. Rogers, S. M. Pollaine, O. L. Landen, C. Blancard, G. Faussurier, P. Renaudin, S. Kuhlbrodt, and R. Redmer. Electronic structure measurements of dense plasmas. *Physics of Plasmas*, 11(5):2754, 2004.
- G. Gregori, A. Ravasio, A. Höll, S. H. Glenzer, and S. J. Rose. Derivation of the static structure factor in strongly coupled non-equilibrium plasmas for X-ray scattering studies. *High Energy Density Physics*, 3(1-2):99–108, 2007.
- R. Grover. Does diamond melt? *The Journal of Chemical Physics*, 71(9):3824–3829, 1979.

-
- M. P. Grumbach and R. M. Martin. Phase diagram of carbon at high pressure: Analogy to silicon. *Solid State Communications*, 100(2):61 – 65, 1996.
- W. H. Gust. Phase transition and shock-compression parameters to 120 GPa for three types of graphite and for amorphous carbon. *Physical Review B*, 22(10):4744, 1980.
- H. H. Gutbrod et al. FAIR Baseline Technical Report. *FAIR collaboration*, 2006.
- Hamamatsu Photonics K.K. C2830 temporal disperser. *Instruction Manual*, 1990.
- Hamamatsu Photonics K.K. Femtosecond Streak Camera C6138 (FESCA-200). *Data sheet*, 2010.
- B. L. Henke, E. M. Gullikson, and J. C. Davis. X-ray interactions: photoabsorption, scattering, transmission, and reflection at $E = 50\text{--}30,000$ eV, $Z = 1\text{--}92$. *Atomic data and nuclear data tables*, 54(2):181–342, 1993.
- P. Hohenberg and W. Kohn. Inhomogeneous Electron Gas. 136:B864, 1964.
- P. Holm and R. Ribberfors. First correction to the nonrelativistic Compton cross section in the impulse approximation. *Physical Review A*, 40(11):6251–6259, 1989.
- W. B. Hubbard, W. J. Nellis, a. C. Mitchell, N. C. Holmes, S. S. Limaye, and P. C. McCandless. Interior structure of neptune: comparison with uranus. *Science*, 253(5020):648–51, 1991.
- J. H. Hubbell, H. A. Gimm, and I. Øverbø. Pair, Triplet, and Total Atomic Cross Sections (and Mass Attenuation Coefficients) for 1 MeV–100 GeV Photons in Elements $Z = 1$ to 100. *Journal of Physical and Chemical Reference Data*, 9:1023, 1980.
- I. Hutchinson. Principles of plasma diagnostics. *Cambridge University Press*, 2005.
- B. F. Ionita, D. H. H. Hoffmann, D. Kraus, A. Ortner, S. Udrea, F. Wagner, V. Bagnoud, A. Blazevic, A. Frank, D. Varentsov, K. Weyrich, N. Amadou, E. Brambrink, and D. Nikolaev. Isentropic Compression Experiments with PHELIX. *2011 Annual Report on High Energy Density Physics with Intense Ion and Laser Beams*, 2012.
- J. Jackson. Classical electrodynamics. *John Wiley & Sons, Inc., New York*, 1999.
- R. W. James. The optical principles of the diffraction of x-rays. *Ox Bow, Woodbridge, CT*, 1962.
- G. I. Kanel, G. S. Bezruchko, A. S. Savinykh, S. V. Razorenov, V. V. Milyavskii, and K. V. Khishchenko. Submicrosecond Polymorphic Transformations Accompanying Shock Compression of Graphite. *High Temperature*, 48:806 – 814, 2010.
- M. D. Knudson, M. P. Desjarlais, and D. H. Dolan. Shock-wave exploration of the high-pressure phases of carbon. *Science*, 322(5909):1822–5, 2008.
- M. Koenig, A. Benuzzi-Mounaix, E. Brambrink, A. Nourou, A. Ravasio, H. Wei, T. Vinci, S. Mazevet, F. Occelli, G. Morard, F. Guyot, T. D. Resseguier, and E. Lescoute. Simulating earth core using high energy lasers. *High Energy Density Physics*, 6(2):210 – 214, 2010.
- W. Kohn. Electronic structure of matter - Wave functions and density functionals. *Nobel Prize lecture*, 1999.
- W. Kohn and L. J. Sham. Self-Consistent Equations Including Exchange and Correlation Effects. 140:A1133, 1965.
- D. Kraus. Spektrale Untersuchung lasererzeugter Hohlraumstrahlung. *Master Thesis, TU Darmstadt*, 2009.

- D. Kraus, A. Otten, A. Frank, V. Bagnoud, A. Blažević, D. O. Gericke, G. Gregori, A. Ortner, G. Schau-
mann, D. Schumacher, J. Vorberger, F. Wagner, K. Wünsch, and M. Roth. X-ray Thomson scatter-
ing on shocked graphite. *High Energy Density Physics*, 8(1):46–49, 2012.
- D. Kremp, M. Schlanges, and W.-D. Kraeft. *Quantum Statistics of Nonideal Plasmas*. Springer,
Berlin, Heidelberg, New York, 2005.
- G. Kresse and J. Furthmüller. Efficient iterative schemes for *ab initio* total-energy calculations using
a plane-wave basis set. *Physical Review B*, 54:11169–11186, 1996.
- G. Kresse and J. Hafner. *Ab initio* molecular dynamics for liquid metals. *Physical Review B*, 47:
558–561, 1993.
- G. Kresse and J. Hafner. *Ab initio* molecular-dynamics simulation of the liquid-metal-amorphous
semiconductor transition in germanium. *Physical Review B*, 49:14251–14269, 1994.
- A. L. Kritcher, P. Neumayer, M. K. Urry, H. Robey, C. Niemann, O. L. Landen, E. Morse, and S. H.
Glenzer. K-alpha conversion efficiency measurements for X-ray scattering in inertial confinement
fusion plasmas. *High Energy Density Physics*, 3(1-2):156–162, May 2007.
- A. L. Kritcher, P. Neumayer, J. Castor, T. Doppner, R. W. Falcone, O. L. Landen, H. J. Lee, R. W. Lee,
E. C. Morse, A. Ng, S. Pollaine, D. Price, and S. H. Glenzer. Ultrafast X-ray Thomson scattering
of shock-compressed matter. *Science*, 322(5898):69, 2008.
- A. L. Kritcher, P. Neumayer, C. R. D. Brown, P. Davis, T. Döppner, R. W. Falcone, D. O. Gericke,
G. Gregori, B. Holst, O. L. Landen, H. J. Lee, E. C. Morse, A. Pelka, R. Redmer, M. Roth, J. Vor-
berger, K. Wünsch, and S. H. Glenzer. Measurements of Ionic Structure in Shock Compressed
Lithium Hydride from Ultrafast X-Ray Thomson Scattering. *Physical Review Letters*, 103(24):
245004, 2009.
- A. L. Kritcher, T. Döppner, C. Fortmann, T. Ma, O. L. Landen, R. Wallace, and S. H. Glenzer. In-flight
measurements of capsule shell adiabats in laser-driven implosions. *Physical Review Letters*, 107:
015002, 2011.
- W. L. Kruer. *The physics of laser plasma interactions*. Westview Press Inc., 2003.
- R. Kubo. The fluctuation-dissipation theorem. *Journal of the Physical Society of Japan*, 12:570,
1957.
- N. L. Kugland, G. Gregori, S. Bandyopadhyay, C. M. Brenner, C. R. D. Brown, C. Constantin,
S. H. Glenzer, F. Y. Khattak, A. L. Kritcher, C. Niemann, A. Otten, J. Pasley, A. Pelka, M. Roth,
C. Spindloe, and D. Riley. Evolution of Elastic X-ray Scattering in Laser-Shocked Warm Dense Li.
Physical Review E, 80:1–8, 2009.
- M. J. Kuncher and S. Seager. Extrasolar Carbon Planets. *arXiv:astro-ph/0504214v2*, 2005.
- H.-J. Kunze. Density dependence of the intensity ratio of resonance and intercombination transi-
tions in C V. *Physical Review A*, 24:1096–1098, 1981.
- A. V. Kurdyumov, V. F. Britun, V. V. Yarosh, A. I. Danilenko, and V. B. Zelyavskii. The Influence of the
Shock Compression Conditions on the Graphite Transformations into Lonsdaleit and Diamond.
Journal of Superhard Materials, 34(1):19–27, 2012.
- R. W. Lee, H. A. Baldis, R. C. Cauble, O. L. Landen, J. S. Wark, A. Ng, S. J. Rose, C. Lewis, D. Riley,
J.-C. Gauthier, and P. Audebert. Plasma-based studies with intense x-ray and particle beam
sources. *Laser and Particle Beams*, 20(03):527–536, 2002.

- R. W. Lee, S. J. Moon, H.-K. Chung, W. Rozmus, H. A. Baldis, G. Gregori, R. C. Cauble, O. L. Landen, J. S. Wark, A. Ng, S. J. Rose, C. L. Lewis, D. Riley, J.-C. Gauthier, and P. Audebert. Finite temperature dense matter studies on next-generation light sources. *J. Opt. Soc. Am. B*, 20(4): 770–778, 2003.
- J. D. Lindl, P. Amendt, R. L. Berger, S. G. Glendinning, S. H. Glenzer, S. W. Haan, R. L. Kauffman, O. L. Landen, and L. J. Suter. The physics basis for ignition using indirect-drive targets on the National Ignition Facility. *Physics of Plasmas*, 11(2):339, 2004.
- D. Löb. Auswertung von Experimenten zur Laser-Plasma-Wechselwirkung mittels Strahlungshydrodynamiksimulationen. *Master Thesis, TU Darmstadt*, 2008.
- S. P. Lyon and J. D. Johnson. SESAME: The Los Alamos National Laboratory Equation of State Database. *LANL Report No. LA-UR-92-3407*, 1992.
- J. J. MacFarlane, I. E. Golovkin, P. R. Woodruff, D. R. Welch, B. V. Oliver, T. A. Mehlhorn, and R. B. Campbell. Simulation of the ionization dynamics of aluminum irradiated by intense short-pulse lasers. *Inertial Fusion Sciences and Application*, page 457, 2003.
- J. J. MacFarlane, I. E. Golovkin, and P. R. Woodruff. HELIOS-CR - A 1-D radiation-magnetohydrodynamics code with inline atomic kinetics modeling. *Journal of Quantitative Spectroscopy and Radiative Transfer*, 99:381–397, 2006.
- S. P. Marsh. LASL Shock Hugoniot Data. *University of California Press, Berkeley*, 1980.
- A. L. Meadowcroft, C. D. Bentley, and E. N. Stott. Evaluation of the sensitivity and fading characteristics of an image plate system for x-ray diagnostics. *Review of Scientific Instruments*, 79: 113102, 2008.
- J. Menzel. Aufbau und Inbetriebnahme einer Kryoanlage zur Targeterzeugung für Experimente mit Hochenergielasern und Schwerionenstrahlen. *PhD thesis, TU Darmstadt*, 2010.
- B. Militzer, W. B. Hubbard, J. Vorberger, I. Tamblyn, and S. A. Bonev. A Massive Core in Jupiter Predicted From First-Principles Simulations. *Astrophysical Journal Letters*, 688:L45, 2008.
- D. Müssig. Plasmadiagnostik mittels Laser-Thomsonstreuung. *Diploma thesis. TU Darmstadt*, 2008.
- C. J. Mundy, A. Curioni, N. Goldman, I. F. W. Kuo, E. J. Reed, L. E. Fried, and M. Ianuzzi. Ultrafast transformation of graphite to diamond: An ab initio study of graphite under shock compression. *The Journal of chemical physics*, 128:184701, 2008.
- M. Murakami, J. Meyer-Ter-Vehn, and R. Ramis. Thermal X-ray emission from Ion-Beam-heated matter. *Journal of X-ray Science and Technology*, 2:127–148, 1990.
- W. J. Nellis, A. C. Mitchell, and A. K. McMahan. Carbon at pressures in the range 0.1-1 TPa (10 Mbar). *Journal of Applied Physics*, 90(2):696, 2001.
- N. Nettelmann, B. Holst, A. Kietzmann, M. French, R. Redmer, and D. Blaschke. Ab initio equation of state data for hydrogen, helium, and water and the internal structure of Jupiter. *The Astrophysical Journal*, 683(2):1217, 2008.
- P. Neumayer, C. Fortmann, T. Döppner, P. Davis, R. W. Falcone, A. L. Kritcher, O. L. Landen, H. J. Lee, R. W. Lee, C. Niemann, S. Le Pape, and S. H. Glenzer. Plasmons in Strongly Coupled Shock-Compressed Matter. *Physical Review Letters*, 105(7):075003, 2010.
- A. Otten. Modellierung des Ausleseprozesses von CR-Bildplatten. *Diploma Thesis, TU Darmstadt*, 2007.

- A. Pak, G. Gregori, J. Knight, K. Campbell, D. Price, B. Hammel, O. L. Landen, and S. H. Glenzer. X-ray line measurements with high efficiency Bragg crystals. *Review of Scientific Instruments*, 75(10):3747, 2004.
- P. K. Patel, A. J. Mackinnon, M. H. Key, T. E. Cowan, M. E. Foord, M. Allen, D. F. Price, H. Ruhl, P. T. Springer, and R. Stephens. Isochoric heating of solid-density matter with an ultrafast proton beam. *Physical Review Letters*, 91(12):125004, 2003.
- I. J. Paterson, R. J. Clarke, N. C. Woolsey, and G. Gregori. Image plate response for conditions relevant to laser-plasma interaction experiments. *Measurement Science and Technology*, 19:095301, 2008.
- L. Pauling and J. Sherman. Screening Constants for Many-electron Atoms. The Calculation and Interpretation of X-ray Term Values, and the Calculation of Atomic Scattering Factors. *Zeitschrift für Kristallographie, Kristallgeometrie, Kristallphysik, Kristallchemie*, 81:1, 1931.
- M. N. Pavlovskii and V. P. Drakin. Concerning the Metallic Phase of Carbon. *JETP Letters*, 4:116, 1966.
- V. K. Pecharsky and P. Y. Zavalij. Fundamentals of powder diffraction and structural characterization of materials. *Springer, New York*, 2003.
- A. Pelka. Röntgenthompsonstreuung als Diagnostik dichter Plasmen. *PhD Thesis, TU Darmstadt*, 2010.
- A. Pelka, G. Gregori, D. O. Gericke, J. Vorberger, S. H. Glenzer, M. M. Günther, K. Harres, R. Heathcote, A. L. Kritcher, N. L. Kugland, B. Li, M. Makita, J. Mithen, D. Neely, C. Niemann, A. Otten, D. Riley, G. Schaumann, M. Schollmeier, A. Tauschwitz, and M. Roth. Ultrafast Melting of Carbon Induced by Intense Proton Beams. *Physical Review Letters*, 105(26):2–5, 2010.
- K. Philipp. Auslesebedingungen von Bildplatten. *Bachelor Thesis, TU Darmstadt*, 2011.
- R. Ramis. r94 system 2009. *Reference Manual*, 2010.
- R. Ramis, R. Schmalz, and J. Meyer-Ter-Vehn. Multi - a computer code for one-dimensional multi-group radiation hydrodynamics. *Computer Physics Communications*, 49(3):475 – 505, 1988.
- R. Ramis, J. Meyer-ter-Vehn, and J. Ramirez. Multi2d - a computer code for two-dimensional radiation hydrodynamics. *Computer Physics Communications*, 180(6):977 – 994, 2009.
- R. Renninger. Absolut-Vergleich der stärksten Röntgenreflexe verschiedener Kristalle. *Acta crystallographica*, 7:677, 1954.
- D. Riley, N. C. Woolsey, D. McSherry, I. Weaver, A. Djaoui, and E. Nardi. X-ray diffraction from a dense plasma. *Physical Review Letters*, 84(8):1704–1707, 2000.
- D. Riley, N. C. Woolsey, D. McSherry, F. Y. Khattak, and I. Weaver. He-like x-ray line emission from laser irradiated sources. *Plasma Sources Science and Technology*, 11:484, 2002.
- F. Roth. Röntgenthompsonstreuung an geschocktem Graphit. *Master Thesis, TU Darmstadt*, 2012.
- M. Roth, I. Alber, V. Bagnoud, C. R. D. Brown, R. Clarke, H. Daido, J. Fernandez, K. Flippo, S. Gaillard, D. C. Gauthier, M. Geissel, S. H. Glenzer, G. Gregori, M. Günther, K. Harres, R. Heathcote, A. L. Kritcher, N. Kugland, S. LePape, B. Li, M. Makita, J. Mithen, C. Niemann, F. Nürnberg, D. Offermann, A. Otten, A. Pelka, D. Riley, G. Schaumann, M. Schollmeier, J. Schütrumpf, M. Tampo, A. Tauschwitz, and An. Tauschwitz. Proton acceleration experiments and warm dense matter research using high power lasers. *Plasma Physics and Controlled Fusion*, 51:124039, 2009.

- J. A. Rowlands. The physics of computed radiography. *Physics in medicine and biology*, page R123, 2002.
- G. Schaumann, M. S. Schollmeier, G. Rodriguez-Prieto, A. Blazevic, E. Brambrink, M. Geissel, S. Korostiy, P. Pirzadeh, M. Roth, F. B. Rosmej, A. Y. Faenov, T. A. Pikuz, K. Tsigutkin, Y. Maron, N. A. Tahir, and D. H. H. Hoffmann. High energy heavy ion jets emerging from laser plasma generated by long pulse laser beams from the NHELIX laser system at GSI. *Laser and Particle Beams*, 23:503–512, 2005.
- M. Schollmeier. Untersuchung schmalbandiger Linienstrahlung lasererzeugter dichter Plasmen für Röntgenstaudiagnostik an Materie. *Diploma Thesis, TU Darmstadt*, 2004.
- D. Schumacher. Charakterisierung laserinduzierter Hohlraumstrahlung. *Diploma Thesis. TU Darmstadt*, 2007.
- D. Schumacher. Untersuchung laserinduzierter Hohlraumstrahlung und Energieverlust von Schwerionen in indirekt geheizten Plasmen. *PhD thesis, TU Darmstadt*, 2012.
- M. Schumacher, F. Smend, and I. Borchert. Incoherent scattering of gamma rays by inner-shell electrons. *Journal of Physics B: Atomic and Molecular Physics*, 8(9):1428, 1975.
- J. F. Seely, G. E. Holland, L. T. Hudson, and A. Henins. X-ray modulation transfer functions of photostimulable phosphor image plates and scanners. *Applied optics*, 47(31):5753–61, 2008.
- SGL Carbon. Special Graphite Grade R 6650. *Datenblatt R 6650/01.01/D/E*, 2012.
- J. Sheffield. Plasma scattering of electromagnetic radiation. *Academic Press, New York*, 1975.
- S. Stanley and J. Bloxham. Convective-region geometry as the cause of Uranus’ and Neptune’s unusual magnetic fields. *Nature*, 428(6979):151–3, 2004.
- N. Tahir, A. Shutov, I. Lomonosov, A. Piriz, R. Redmer, T. Stöhlker, H. Geissel, C. Deutsch, and V. Fortov. High Energy Density Physics Studies at the Facility for Antiprotons and Ion Research: the HEDgeHOB Collaboration. *Contributions to Plasma Physics*, 51(4):309–321, 2011.
- M. K. Urry, G. Gregori, O. L. Landen, A. Pak, and S. H. Glenzer. X-ray probe development for collective scattering measurements in dense plasmas. *Journal of Quantitative Spectroscopy and Radiative Transfer*, 99(1-3):636–648, 2006.
- US National Research Council. Frontiers in high energy density physics: The X-games of contemporary science. *National Academic Press*, 2003.
- L. v. Hámos. Röntgenspektroskopie und Abbildung mittels gekrümmter Kristallreflektoren. I. Geometrisch-optische Betrachtungen. *Annalen der Physik*, 409(6):716–724, 1933.
- M. van Thiel. Compendium of shock wave data. *Lawrence Livermore Laboratory Report UCRL-50108*, 1977.
- S. M. Vinko, O. Ciricosta, B. I. Cho, K. Engelhorn, H. K. Chung, C. R. D. Brown, T. Burian, J. Chalupsky, R. W. Falcone, C. Graves, V. Hajkova, A. Hingginbotham, L. Juha, J. Krzywinski, H. J. Lee, M. Messerschmidt, C. D. Murphy, Y. Ping, A. Scherz, W. Schlotter, S. Toleikis, J. J. Turner, L. Vysin, T. Wang, B. Wu, U. Zastrau, D. Zhu, R. W. Lee, P. A. Heimann, B. Nagler, and J. S. Wark. Creation and diagnosis of a solid-density plasma with an X-ray free-electron laser. *Nature*, pages 0–4, 2012.
- D. Waasmaier and A. Kirfel. New analytical scattering-factor functions for free atoms and ions. *Acta Crystallographica Section A: Foundations of Crystallography*, 51(3):416–431, 1995.

-
- X. Wang, S. Scandolo, and R. Car. Carbon phase diagram from *Ab Initio* molecular dynamics. *Physical Review Letters*, 95:185701, 2005.
- K. Wünsch. Theory of X-ray Thomson Scattering in Warm Dense Matter. *PhD thesis. University of Warwick*, 2011.
- K. Wünsch, J. Vorberger, and D. O. Gericke. Ion structure in warm dense matter: Benchmarking solutions of hypernetted-chain equations by first-principle simulations. *Physical Review E*, 79: 010201, 2009.
- J. Zazula. On graphite transformations at high temperature and pressure induced by absorption of the LHC beam. *LHC Project Note*, 78, 1997.
- Y. B. Zeldovic and Y. P. Raizer. Physics of shock waves and high-temperature hydrodynamic phenomena. *Academic Press, New York and London*, 1966.



Publications

In preparation

D. Kraus, J. Vorberger, V. Bagnoud, A. Blazevic, A. Frank, D. O. Gericke, G. Gregori, A. Ortner, A. Otten, F. Roth, G. Schaumann, K. Siegenthaler, F. Wagner, K. Wünsch and M. Roth

Liquid carbon at one million times atmospheric pressure

G. Hoffmeister, C. Bellei, K. Harres, D. Ivanov, D. Kraus, A. Pelka, B. Rethfeld, G. Schaumann and M. Roth

Influence of fs-laser desorption on TNSA accelerated ions

Submitted

A. Frank, A. Blazevic, V. Bagnoud, M. M. Basko, M. Börner, W. Cayzac, P. L. Grande, D. Kraus, T. Heßling, D. H. H. Hoffmann, A. Ortner, A. Otten, A. Pelka, D. Pepler, D. Schumacher, An. Tauschwitz and M. Roth

Energy loss and charge-transfer of argon in laser-generated carbon plasma

submitted to Physical Review Letters

Publications in refereed journals

D. Kraus, A. Otten, A. Frank, V. Bagnoud, A. Blazevic, D. O. Gericke, G. Gregori, A. Ortner, G. Schaumann, D. Schumacher, J. Vorberger, F. Wagner, K. Wünsch and M. Roth

X-ray Thomson scattering on shocked graphite

High Energy Density Physics **8**, 46-49 (2012)

G. Hoffmeister, M. Roth, C. Bellei, K. Harres, D. Kraus, A. Pelka, B. Rethfeld and G. Schaumann

Effects of fs-laser desorption on the target normal sheath acceleration (TNSA)

AIP Conference Proceedings **1464**, 418 (2012)

T. Bartal, M. E. Foord, C. Bellei, M. H. Key, K. A. Flippo, S. A. Gaillard, D. T. Offermann, P. K. Patel, L. C. Jarrott, D. P. Higginson, M. Roth, A. Otten, D. Kraus, R. B. Stephens, H. S. McLean, E. M. Giraldez, M. S. Wei, D. C. Gautier and F. N. Beg

Focusing of short-pulse high-intensity laser-accelerated proton beams

Nature Physics **7**(12), 1-4 (2011)

T. Heßling, A. Blazevic, A. Frank, D. Kraus, M. Roth, G. Schaumann, D. Schumacher, T. Stöhlker and D. H. H. Hoffmann

Time- and spectrally resolved measurements of laser-driven hohlraum radiation

Physical Review E **84**, 016412 (2011)



Danksagung

Als Erstes danke ich Prof. Dr. Markus Roth dafür, dass er mit die Möglichkeit zur Durchführung dieser Arbeit in diesem sehr interessanten und spannenden Themenfeld eröffnet hat; für sein Interesse, sein Vertrauen in mich und seine Unterstützung.

Prof. Dr. Thomas Stöhlker danke ich für die Aufnahme in der Plasmaphysikgruppe der GSI und die damit verbundene Möglichkeit, die Experiment dort durchführen zu können.

Prof. Dr. Dr. h.c./RUS Dieter H. H. Hoffmann danke ich sehr für die Übernahme des zweiten Gutachtens für diese Arbeit.

Dipl.-Phys. Anke Otten und Dr. Alexander Pelka danke ich vielmals für die Einarbeitung in das Thema in Theorie und Experiment. Besonders die damit verbundenen Auslandserfahrungen haben sich tief bei mir "eingebrannt".

Dr. Dirk Gericke danke ich für die vielen Diskussionen über die Interpretation der gewonnenen Daten. Außerdem motivierte er Teile seines Teams, Rechnungen zur Struktur von Kohlenstoff durchzuführen. Dies sind Dr. Jan Vorberger, dem ich die DFT-MD-Simulationen verdanke, und Dr. Kathrin Wünsch, die die HNC-Rechnungen durchgeführt hat.

Many thanks to Dr. Gianluca Gregori for developing much of the theoretical concepts which made this work possible and for providing the source code of his X-ray scattering program.

"Meiner" Master-Studentin B.Sc. Franziska Roth danke ich für die Unterstützung bei Experiment und Auswertung und das damit verbundene Hinterfragen der angewendeten Methoden. B.Sc. Karen Siegenthaler vervollständigt das Team der "Thomson-Streuer", ich danke ihr für die Mithilfe beim Experiment und für viele schwierige Fragen.

Die Experimente an Z6 hätten niemals funktioniert ohne ein grandioses Team. Neben einigen bereits genannten sind das Dr. Abel Blazevic, der alles am Laufen hält, Dr. Alexander Frank, der für traumhafte Parameter am nhelix-Laser sorgt, außerdem waren dabei Dipl.-Phys. Alex Ortner, M.Sc. Florian Wagner, Dr. Dennis Schumacher, M.Sc. Witold Cayzac und B.Sc. Armin Weckmann. Danke für die Motivation, das Engagement und den Spaß dabei.

Ausschlaggebend für den Erfolg der Experimente war nicht zuletzt ein hervorragend laufender PHELIX-Laser, der von einem hoch motivierten Team betrieben wird. Danke an Dr. Vincent Bagnoud, Dipl.-Ing. Dirk Reemts, Dr. Udo Eisenbarth, Dr. Stefan Götte, Dipl.-Ing. Sabine Kunzer, Dr. Bernhard Zielbauer, Dr. Jerome Fils und Lilianna Tymura.

M.Sc. Daniel Löb danke ich für die Einarbeitung in den Hydrodynamikcode MULTI2D, der wichtige Erkenntnisse über den Charakter der Schockwelle geliefert hat.

M.Sc. Michael Börner danke ich für den Aufbau des optischen Rings des Multi-Frame-Interferometers, der die Verwendung dieser für die Experimente sehr wichtigen Diagnostik ermöglicht hat.

Für das Design und den Bau der "Backlighter-Targets" danke ich vielmals Dr. Gabriel Schumann und Alexander Waltinger vom Targetlabor des Instituts für Kernphysik der TU Darmstadt. Dr. Bettina Lommel und besonders Annett Hübner danke ich sehr für die Herstellung der Kohlenstoffproben und das sehr aufwendige Polieren der Oberflächen. Dr. Kay-Obbe Voss danke ich sehr für die Vermessung der Oberflächenstruktur der Kohlenstofftargets mit dem Rasterkraftmikroskop.

Allen jetzigen und ehemaligen Mitgliedern der AG Laser- und Plasmaphysik der TU Darmstadt danke ich für ein tolles Arbeitsklima.

"Last but not least" danke ich meinen Freunden, meiner Familie und Anna für den Rahmen, der die Durchführung dieser Arbeit erst möglich gemacht hat.

Lebenslauf

Persönliche Daten

Name	Dominik Kraus
Geburtstag	27.11.1984 in Darmstadt
Staatsangehörigkeit	deutsch

Schulbildung

1991 - 1995	Grundschule
1995 - 2001	Goetheschule Dieburg
2001 - 2004	Gymnasiale Oberstufe, Alfred-Delp-Schule Dieburg
Juni 2004	Abitur (Note 1,0)

Studium

2004-2009	Physikstudium an der TU Darmstadt
November 2009	Abschluss Master of Science (Note 1,0) Titel der Abschlussarbeit: <i>Spektrale Untersuchung lasererzeugter Hohlraumstrahlung</i>
seit Dezember 2009	Promotion an der TU Darmstadt Thema: <i>Charakterisierung von Phasenübergängen in warmer dichter Materie mit Röntgenstreuung</i>

Berufserfahrung

seit Dezember 2009	Wissenschaftlicher Mitarbeiter an der TU Darmstadt
seit 2007	Gästeführer für Besuchergruppen im European Space Operations Center der ESA

Auszeichnungen

Juni 2004	Buchpreis der Deutschen Physikalischen Gesellschaft für hervorragende Leistungen im Fach Physik
-----------	--

Auslandsaufenthalte

2010-2012 (insgesamt 23 Wochen)	Los Alamos National Laboratory, USA Lawrence Livermore National Laboratory, USA Rutherford Appleton Laboratory, Vereinigtes Königreich
------------------------------------	--



Erklärung zur Dissertation

Hiermit versichere ich, die vorliegende Dissertation ohne Hilfe Dritter nur mit den angegebenen Quellen und Hilfsmitteln angefertigt zu haben. Alle Stellen, die aus Quellen entnommen wurden, sind als solche kenntlich gemacht. Diese Arbeit hat in gleicher oder ähnlicher Form noch keiner Prüfungsbehörde vorgelegen.

Darmstadt, den 10. Dezember 2012

(Dominik Kraus)